ABSTRACT

Title of Dissertation: COMPACT LASER DRIVEN ELECTRON AND PROTON ACCELERATION WITH LOW ENERGY LASERS

George Albert Hine,
Doctor of Philosophy 2017

Dissertation directed by: Professor Howard Milchberg,
Department of Physics

Laser-driven particle accelerators offer many advantages over conventional particle accelerators. The most significant of these is the magnitude of the accelerating gradient and, consequently, the compactness of the accelerating structure. In this dissertation, experimental and computational advances in laser-based particle acceleration in three intensity regimes are presented. All mechanisms investigated herein are accessible by “tabletop” ultrashort terawatt-class laser systems found in many university labs, with the intention of making them available to more compact and high repetition rate laser systems. The first mechanism considered is the acceleration of electrons in a preformed plasma “slow-wave” guiding structure. Experimental advances in the generation of these plasma guiding structures are presented. The second mechanism is the laser-wakefield acceleration of electrons in the self-modulated regime. A high-density gas target is implemented experimentally leading to electron acceleration at low laser pulse energy. Consequences of operating

in this regime are investigated numerically. The third mechanism is the acceleration of protons by a laser-generated magnetic structure. A numerical investigation is performed identifying operating regimes for experimental realizations of this mechanism. The key advances presented in this dissertation are:

- The development and demonstration of modulated plasma waveguide generation using both mechanical obstruction and an interferometric laser patterning method
- The acceleration of electrons to MeV energy scales in a high-density hydrogen target with sub-terawatt laser pulses and the generation of bright, ultra-broadband optical pules from the interaction region
- 3D particle-in-cell (PIC) simulations of self-modulated laser wakefield acceleration in a plasma, showing the generation of broadband radiation, and the role of "direct laser acceleration" in this regime
- 3D PIC simulations of laser wakefield acceleration in the resonant regime, identifying spatio-temporal optical vortices in a laser-plasma system
- 3D PIC simulations of proton acceleration by magnetic vortex acceleration using TW-class laser pulses

COMPACT LASER DRIVEN ELECTRON AND PROTON ACCELERATION WITH LOW ENERGY LASERS

by

George Albert Hine

Dissertation submitted to the Faculty of the Graduate School of the
University of Maryland, College Park, in partial fulfillment
of the requirements for the degree of
Doctorate of Philosophy
2017

Advisory Committee:
Doctor Howard Milchberg Chair
Doctor Tim Koeth
Doctor Phil Sprangle
Doctor Ki-Yong Kim
Doctor Gretchen Campbell

© Copyright by
George Albert Hine
2017

Dedication

For Kiersten

Acknowledgements

I would like to thank Professor Howard Milchberg for generously giving me the opportunity to work in his lab, when others would not. Men like Howard, who have such a profound dedication to their art, are rare. Howard's delight in research is clearly reflected in his team and their many accomplishments over the years.

I would also like to thank Professor Timothy Koeth for first introducing me to Professor Milchberg.

I must thank Drs. Brian Layer, Sun-Jun Yoon, and Jennifer Elle for showing me the ropes when I started in the group. Their efforts, advice, and experience was invaluable. I had the honor of cultivating a friendship with Dr. Andrew Goers, built on a foundation of hard work, long nights, and common goals. It has been a pleasure to work with Linus Feder, Bo Miao, Fatholah Salehi, Daniel Woodbury, and Robert Schwartz, and to see them each step up to new challenges. They have already accomplished so much and I am excited for their future work.

Along with Dr. Jared Wahlstrand, Sina Zahedpour, Nihal Jhajj, Eric Rosenthal, and Ilia Larkin, the group members have been like a family to me and I'm very thankful for the opportunity to work, and regularly decompress, with them.

Working in IREAP has been a wonderful experience, thanks in no small part to its staff. I have Edd Cole, Nolan Ballew, Jay Pyle, Don Martin, Bill Schuster, and Stephen Henderson to thank for teaching me everything I know about machining and Doctor Ed Condon and Bryan Quinn for working tirelessly for this institute.

I'm thankful to have shared this experience with such fantastic students, especially Dr. Kevin Pedro, Dr. Nat Steinsultz, Dr. Jeff Demers, Joe Garret, Neil

Anderson, Alireza Seif, and Rachel Ruisard. They, along with Virginia Garrett and Meredith Lukow, have been a wellspring of support and comradery. I am indebted to Sam Allen, Emily Leak, and Taylor Baker, who taught me so much about the art and science of wellbeing.

My fiancé, Kiersten Ruisard, has been singularly supportive, every step of the way, and nothing I write or say could ever thank her enough for it.

Finally, I could not have completed this work without the endless love and support I’ve received from my parents, my sisters and their wonderful families, and the Lord God.

Table of Contents

List of Tables

List of Figures

Chapter 1: Introduction

1.1 Motivation

1.1.1 Conventional Particle Accelerators

Particle accelerators are ubiquitous tools in industrial, medical, and scientific fields. In industry, they are used to characterize and process materials and goods, as well as in several forms of lithography [1]. In medicine, particles and secondary radiation are used to directly treat cancers, with fast ions also used to produce radiotracers for tomography and imaging [2]. In the fundamental sciences, particle accelerators are used to produce extreme conditions to study the nature of the universe [3].

Modern conventional accelerators operate using radio-frequency (RF) oscillating electric fields in either a cyclic or linear geometry. The RF fields are either produced or guided by metallic structures, limiting the maximum field strength to below the breakdown of the structure, ~100 MV/m and even lower at higher frequencies [4]. This means that for a linear accelerator to reach ~ 10 GeV energies(as is desirable for many scientific applications) [3], the necessary acceleration length is on the order of kilometers. Cyclic accelerators overcome this limitation by winding the acceleration length into either a spiral (as in a cyclotron) or a closed loop (a synchrotron) using magnetic fields. Radiative losses, however, limit the radius of curvature for high energy particles, which ultimately limits cyclic accelerators to TeV proton energy scales and impractically low energies for electrons.

With conventional accelerators reaching their practical energy limitations, efforts are being made to use plasma as a medium for acceleration. It allows for field gradients as high as TV/m, reducing the necessary acceleration length by several orders of magnitude. [5,6]

1.1.2 Laser-Driven Particle Accelerators

Modern laser technology can produce can produce PW (petawatt, 10^{15} W) peak powers, and even ~10 – 100 TW (terawatt, 10^{12} W) at the level of a university lab. Using interactions of these lasers with plasma, the high field gradients previously mentioned are accessible. At present, electrons have been accelerated to over 4 GeV in 9 cm using a 300 TW laser in a discharge capillary [7], and it has been shown that electrons can even be accelerated to the MeV scale with sub-terawatt laser pulses [8].

Because the interaction region is on the sub-mm to several-cm scale, it is the laser systems that dictate facility size and cost. These systems can range from large user facilities to tabletop size. There have been many efforts to develop progressively more powerful lasers for particle acceleration; however, this is often at the expense of the often-boasted-of compactness. In contrast, fiber lasers [9] and disk lasers [10] offer a compact, high repetition rate option and the use of such systems for particle acceleration would be a true realization of a portable high-energy particle accelerator.

While conventional particle accelerators have been developing since the late 1920's, laser-based particle acceleration is still a young field. Although accelerating gradients in plasma are inherently much larger than in conventional accelerating structures, factors like beam quality and average current are still being addressed.

1.2 Laser Propagation in Plasma

1.2.1 Electromagnetic Waves in Plasma

In contrast to polarizable media in which bound electrons create polarization fields, the propagation of light in a plasma is dictated by the quivering of free electrons. The resulting dispersion relation,

$$\begin{aligned} \omega &= \sqrt{k^2c^2+\omega_p^2} \\ \omega_p^2 &= \frac{4\pi e^2 n_e}{m_e} \end{aligned} \tag{1.1}$$

with n_e the electron number density, e the electron charge, and m_e the electron mass, leads to a density- and frequency-dependent refractive index η,

$$\begin{aligned} \eta &= \sqrt{1-\frac{n_e}{n_{crit}}} \\ n_{crit} &= \frac{\omega^2 m_e}{4\pi e^2} \end{aligned} \tag{1.2}$$

where n_{crit} is the critical density above which light of frequency ω becomes evanescent. The plasma dispersion curve is shown in figure 1.1. It can be seen that as the density approaches critical density, the phase and group velocity approach infinity and zero respectively:

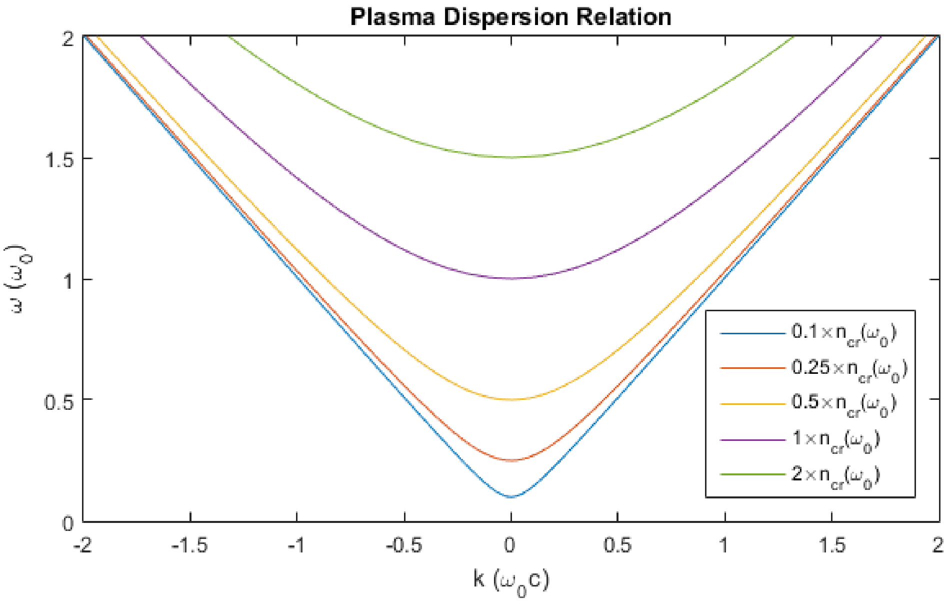

Figure 1.1 The dispersion relation for electromagnetic waves in a plasma. Permissible frequencies are those above the plasma frequency. It can be seen that, for a given frequency, the phase velocity increases with increasing plasma density.

$$v_{ph} = \left. \frac{c}{\sqrt{1 - \frac{n_e}{n_{crit}}}} \right|_{n_e \to n_{crit}} \to \inf$$

$$v_g = c \left. \sqrt{1 - \frac{n_e}{n_{crit}}} \right|_{n_e \to n_{crit}} \to 0 \qquad (1.3)$$

1.2.2 Linear Guiding in a Plasma Fiber

From expression 1.2, it can be seen that a local plasma density minimum corresponds to a refractive index maximum, and thus, an electromagnetic guiding structure. Figure 1.2 shows the refractive index profile of a step-index fiber optic. The difference between the wall and the on-axis refractive index causes rays of an angle greater than the critical angle, $\sin\theta_{cr} = n_2 / n_1$ to undergo total internal reflection, and

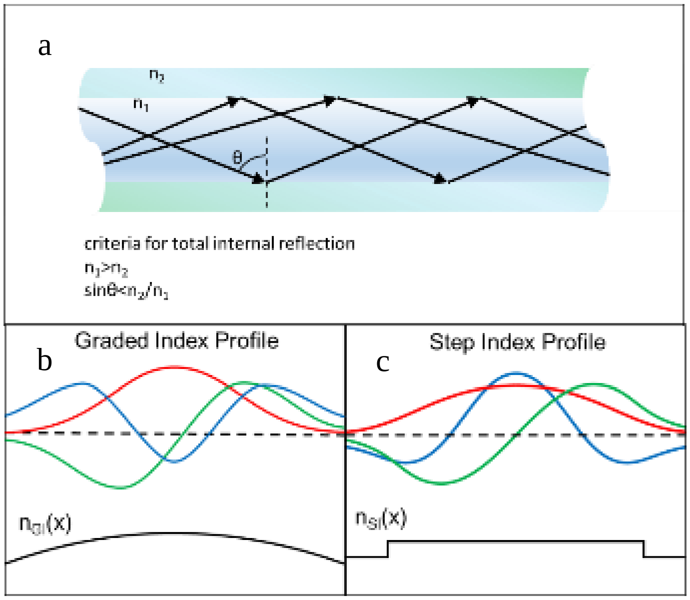

Figure 1.2 (a) A step-index dielectric fiber. Rays with oblique incidence experience total internal reflection and are guided down the length of the fiber. (b,c) When the index profile is comparable to the wavelength, the light propagates as a discrete number of finite "guided modes." The first few guided modes of a graded index fiber and a step index fiber are provided.

be guided. In plasma, this requires a high electron density at the walls and low density on-axis.

This concept can be extended to small guide radii, where the assumptions of ray optics start to break down, and the guided light is described instead by a discrete number of guided modes. The index profile of the guide then dictates the shape and number of the guided modes. The guides described in this dissertation are nearly parabolic, leading to a series of guided modes described by Laguerre-Gauss functions. This is ultimately advantageous because the laser profile at the focus (where coupling takes place) is nearly Gaussian, which reduces losses when coupling into the guide. Generation and guiding in a plasma waveguide was first demonstrated by Durfee *et al.* [11] who used a pulsed Bessel beam to generate a plasma column which transiently formed a waveguide as it expanded. [12] The mode properties of plasma waveguides are discussed fully by Clark *et al*. [13]

1.2.3 Nonlinear Guiding in a Uniform Plasma

In contrast to guiding in a preformed channel, self-guiding can occur as one of several nonlinear processes in a uniform plasma. This nonlinearity arises from the relativistic motion of electrons in the laser field, which is often associated with an effective "mass-shift." The effective mass-shift can be introduced into the refractive index by

$$\begin{aligned} n_{cr}(\gamma) &= \frac{(\gamma m_{e0})\omega}{4\pi e^2} = \gamma\left(\frac{m_{e0}\omega}{4\pi e^2}\right) = \gamma n_{cr0} \\ \eta &= \sqrt{1-\frac{n_e}{\gamma n_{cr0}}} \end{aligned} \tag{1.4}$$

where it follows from conservation of canonical momentum (shown in the appendix) that

$$\gamma = \sqrt{1+\tfrac{1}{2}a_0^2} \tag{1.5}$$

where

$$a_0 = \frac{e|\mathbf{A}|}{m_e c^2} \approx 0.855\times10^{-9} I^{1/2}[W/cm^2]\lambda_0[\mu m] \tag{1.6}$$

is the normalized vector potential. This can be expanded in the field strength, a_0, for small values of a_0 to reveal a Kerr-like nonlinearity,

$$\eta \approx \sqrt{1-{}^{n_e}\!/\!_{n_{cr}}} + \frac{1}{4}\frac{{}^{n_e}\!/\!_{n_{cr}}}{\sqrt{1-{}^{n_e}\!/\!_{n_{cr}}}}a_0^2 \tag{1.7}$$

With this nonlinearity come third-order nonlinear processes, including self-focusing, and self-phase modulation. It should also be noted that the nonlinearity has a strong dependence on plasma density near the critical density, n_{crit}.

Equation 1.6 is useful for describing the weakly relativistic dynamics of propagation before pulse collapse [14], or while guided in a plasma channel [8,15,16], but TW-scale systems can reach intensities well above $a_0=1$, invalidating the perturbative expansion (1.6) for the refractive index. Furthermore, when self-focusing leads to pulse collapse, the would-be collapse to singularity is mitigated by additional effects, which include higher order nonlinearities and ponderomotive force-induced charge expulsion [17]. The dynamics that ensue are highly nonlinear and thus, numerical simulation is often used to capture the system's complex behavior.

1.2.4 Power, Intensity, and Plasma Density

The laser systems and gas targets that will be described in Chapter 2 can access a wide range of nonlinearity. At low densities, or low powers, the propagation can be nearly linear or only weakly nonlinear. In this regime, plasma waves may be driven, but only at perturbative amplitudes, where the electron density response is sinusoidal. Without a guiding structure, diffraction entirely controls beam evolution, with the high-intensity interaction limited to a Rayleigh range, $z_R = \frac{\pi w_0^2}{\lambda}$, with w_0 the focal spot size (size at beam waist) and λ the laser wavelength. Relativistic nonlinear focusing overcomes diffraction if the laser power P is above the critical power for self-focusing, [17]

$$P_{cr} = \frac{2ce^2}{r_e^2}\frac{\omega_p^2}{\omega^2} \approx 17\frac{n_{cr}}{n_e}GW \tag{1.8}$$

where $r_e = \frac{e^2}{m_e c^2}$ is the classical electron radius. For a very long plasma, when

$P/P_{cr}>1$, the pulse focuses until the laser ponderomotive force drives electron cavitation, which terminates the self-focusing, with the laser spot about the size of a plasma period. For the shorter, finite length plasmas typical of gas jet targets, self-focusing collapse and cavitation can occur for P/P_{cr} significantly larger than unity, depending on plasma length. After collapse, the pulse and plasma wave induced by the ponderomotive force travel as a “filament” until the laser is depleted enough that self-focusing can no longer beat out diffraction [17,18]. If the density and power are sufficiently high, another regime can be reached in which the plasma wake is not only electrostatic, but also produces a magnetic field. The persistence of this field makes the ion motion non-negligible. In Chapter 5, this effect will be discussed in the context of proton acceleration.

1.3 Laser Acceleration of Electrons in Plasma

1.3.1 Laser Wakefield Acceleration

Much of the complexity of relativistic nonlinear optics stems from the density response of the plasma. The origin of this response is a time-averaged outward force which the laser pulse exerts on the plasma. The magnitude of this force can be estimated by considering the quiver energy of an electron in a laser field. The electron quiver energy is given by (derived in appendix A.2.1),

$$T = \gamma - 1 = \sqrt{1 + \mathbf{a} \cdot \mathbf{a}} - 1 \qquad (1.9)$$

Since the electron’s time-averaged kinetic energy (derived in Appendix A.2.2) has spatial dependence,

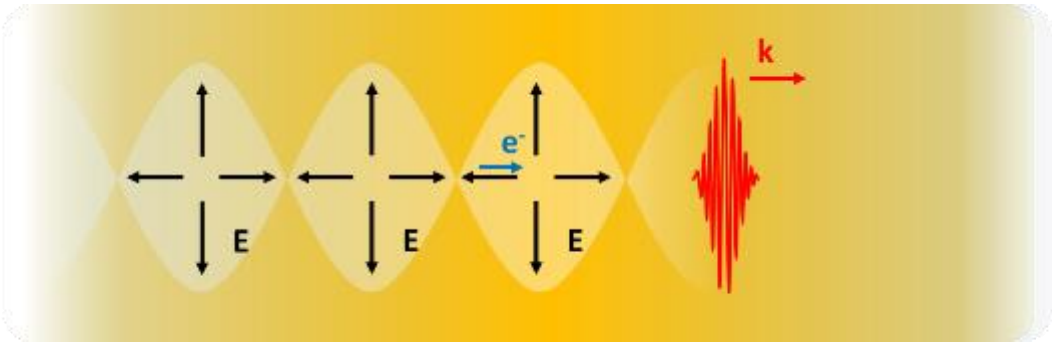

Figure 1.3 A schematic of laser wakefield acceleration. An intense laser pulse (red) drives a plasma wave as it travels through a plasma (orange). The resulting charge displacement creates an electrostatic field (black) which can accelerate electrons (blue).

$$< \frac{T}{mc^2} > = < \gamma - 1 > = < \sqrt{1 + \mathbf{a} \cdot \mathbf{a}} - 1 > \approx \frac{a_0^2(\mathbf{r},t)}{2} \tag{1.10}$$

a body force called the ponderomotive force can be identified.

$$\frac{f}{mc^2} = -\nabla < \frac{T}{mc^2} > \approx -\nabla \frac{a_0^2}{2} \tag{1.11}$$

The effect of this force is the expulsion of electrons, with the laser driving a wake which trails it. It was proposed that electrons co-propagating with the laser could be accelerated by the plasma wake's electrostatic field, [19] as shown in figure 1.3. Moreover, it was found that a wake driven to sufficiently high amplitudes traps electrons from the background plasma in the accelerating phase of the wave [20,21]. The combination of these effects has led to laser wakefield acceleration becoming widely studied. High quality, high energy electron beams have been demonstrated using this mechanism [22–24].

The coupling efficiency between the laser pulse and the plasma wave is dependent on the pulse length of the laser. When the laser pulse length τ_0 is approximately half of the plasma period $\tau_p = 2\pi / \omega_p$ the laser pulse couples

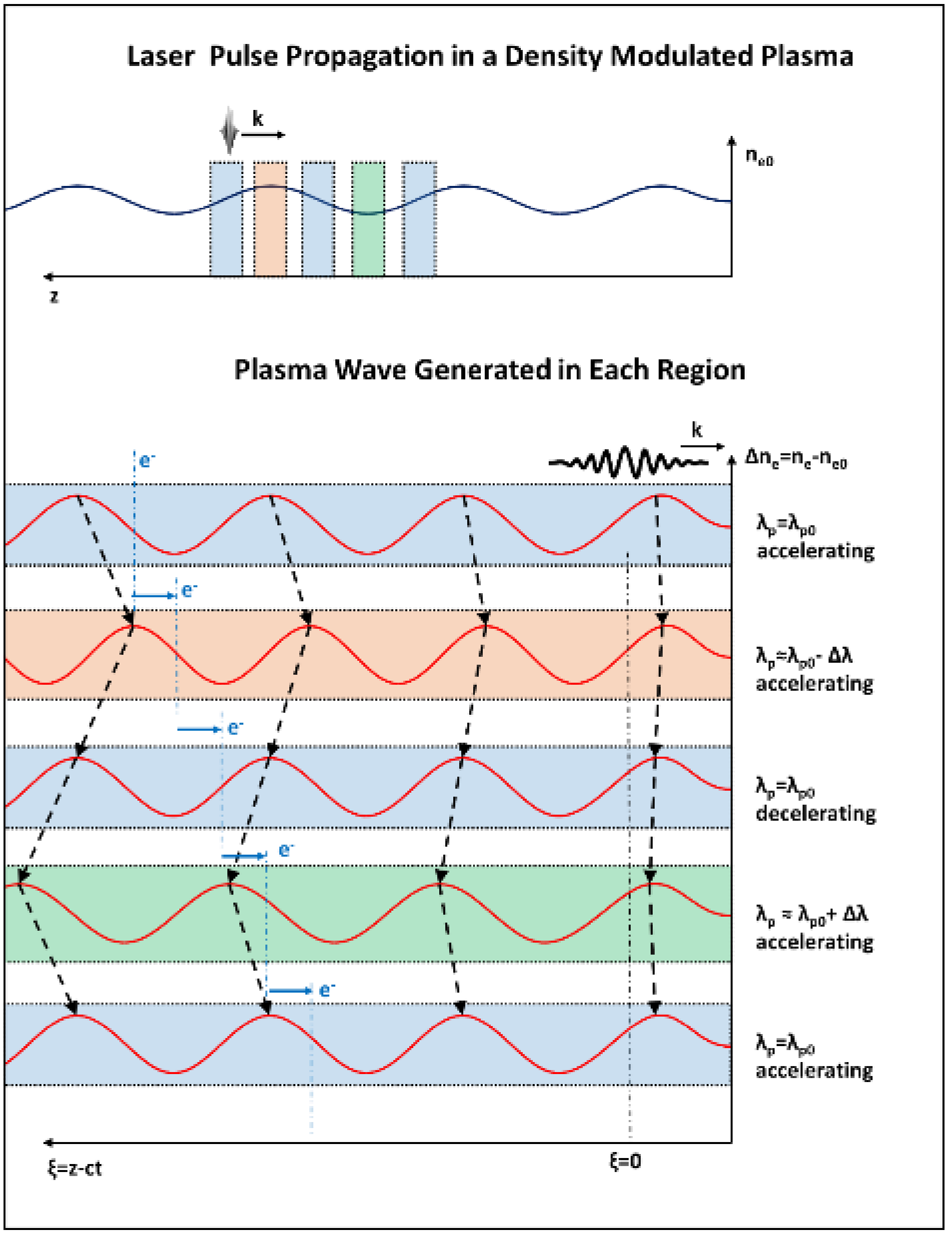

Figure 1.4 Quasi-phase matching of laser wakefield acceleration. An intense laser pulse propagates in a density modulated plasma. In each region, indicated by the colored boxes in the top chart, the local plasma density n_e dictates a plasma wavelength $\lambda_p(n_e)=c\left(4\pi e^2 n_e / m_e\right)^{-1/2}$. The laser drives a plasma wave (red) which expands and contracts as it travels between regions. A properly phased electron with the appropriate velocity will experience the accelerating phase of the plasma wave over a greater length than the decelerating phase, resulting in a net energy gain. [25]

efficiently to the plasma wave and is said to be in the “resonant regime.” If the pulse length is longer than a plasma period, it is modulated into a train of pulselets which are separated by the plasma period, and the system is said to be in the “self-modulated regime.”

As these electrons approach the speed of light, they will exceed the laser group velocity, and thus the phase velocity of the plasma wake. This causes them to slip from the accelerating phase of the wake into the decelerating phase, imposing a limit on the maximum electron energy.

S.-J. Yoon *et al.* showed this dephasing can be mitigated by a periodically modulated plasma density [25]. In their model, as an electron bunch dephases from its plasma wave potential bucket, the plasma wave expands due to the local change in plasma density, causing the electrons to enter the accelerating phase of the next bucket. As the electrons continue to outrun the wave, compression of the buckets keeps them in the accelerating phase until the process repeats. Figure 1.4 illustrates this concept.

1.3.2 Quasi Phase-Matched Direct Laser Acceleration

The process of using a periodically indexed medium to combat dephasing is more generally referred to as “Quasi-Phase Matching” (QPM). A wave traveling along a periodic structure can be broken into a series of longitudinal modes, each with a different phase velocity which depends on the modulation period and amplitude. This is shown in figure 1.5. By tuning the modulation, one of the longitudinal modes

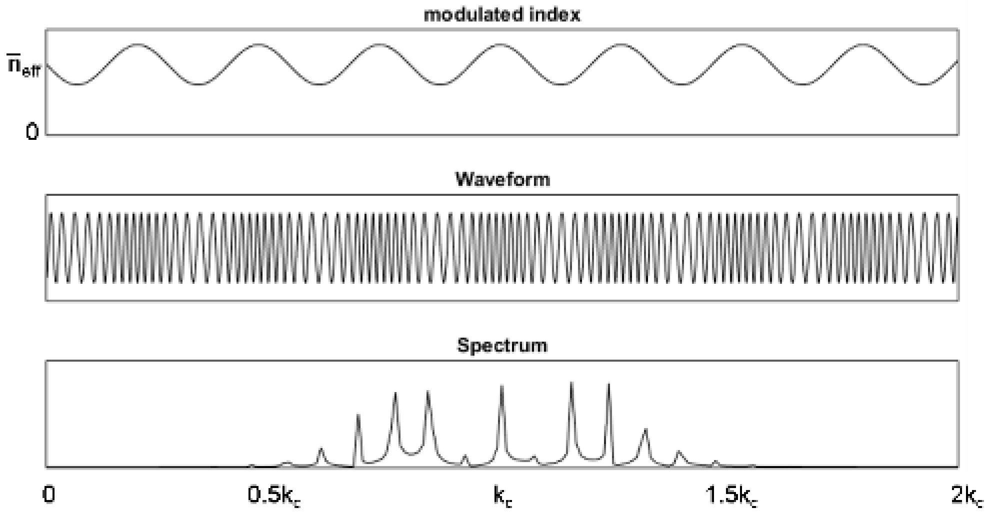

Figure 1.5 Longitudinal decomposition of a wave in a periodically modulated refractive medium. The modulation gives rise to a spectrum of longitudinal modes, around a central wavenumber k_c, with phase velocity k/ω. Since this spectrum is dependent on the modulation period and amplitude, the phase velocity of a mode can be tuned to quasi-phase match to relativistic electrons.

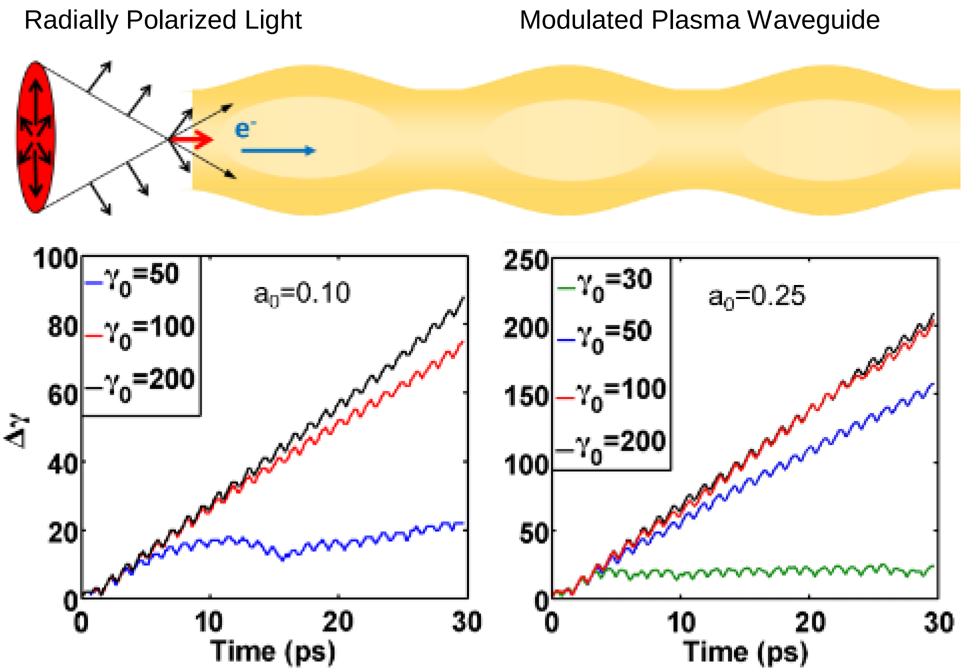

Figure 1.6 Using quasi-phase matching, the longitudinal field of radially polarized light can be phase matched to an electron bunch in a plasma waveguide. The result is energy gain with oscillatory and linear growth terms. Pic simulations show for a fixed laser energy and modulation period, there is a minimum initial electron energy for effective acceleration. [28]

can be matched to a desired velocity. In the case of quasi-phase matched laser wakefield acceleration, the plasma wave, which has a phase velocity equal to the laser group velocity $v_g<c$, is quasi-phase matched to a relativistic electron beam with velocity nearly c. Another acceleration scheme which utilizes QPM is an alternative to laser wakefield acceleration proposed by Layer *et al.* [26] and York *et al.* [27]. In this scheme, electrons are accelerated directly with the axial component field of a guided radially polarized laser pulse. Quasi-phase matching is then necessary because the phase velocity of light in a uniform plasma or unmodulated plasma waveguide is superluminal, and thus inaccessible to accelerated particles. Axial modulations of a plasma waveguide induce significant axial harmonics of the guided pulse which are subluminal and can phase match to the accelerated electrons moving at nearly *c*.

The realization of this mechanism involved guiding of a radially polarized laser pulse in a plasma channel. The radially polarized pulse has an on-axis longitudinal component which oscillates at the laser frequency, which can be quasi-phase matched to a co-propagating electron bunch. Yoon *et al.* demonstrated this acceleration mechanism using PIC simulations, shown in figure 1.6. [28] Also, it has been seen that a half-pellicle can be used to generate a TM01 profile, which is a good approximation to a completely radially polarized beam. [29]

1.4 Laser Acceleration of Ions in Plasma

1.4.1 Methods of Laser-Based Ion Acceleration

A wide variety of laser based ion acceleration mechanisms have been proposed [6,30]. Currently, the most prevalent mechanism for laser-ion acceleration is target normal sheath acceleration, wherein protons in adsorbents (usually water) are accelerated from the rear surface of metal foils upon irradiation of the front surface with an intense laser [31]. Other techniques which implement a laser interacting with an overdense plasma have been proposed, including collisionless shock acceleration [32], radiation pressure acceleration [33], and the break out afterburner mechanism [34]. These ion acceleration techniques require a carefully placed, delicate few-micron to few-nanometer thick foil which, following each shot, must be realigned off the resulting perforation. These targets are extremely sensitive to laser pulse contrast. Furthermore, the laser-induced blowoff from solid targets poses a damage and contamination hazard to nearby optics.

1.4.2 Magnetic Vortex Acceleration

The laser acceleration of ions in underdense plasma has also been investigated. These mechanisms enable the use of replenishable gas targets which produce no blowoff that can damage or coat optics, and do not need to be realigned after each shot. Recently, high density gas jets have been used for efficient, high repetition rate electron acceleration [35], operating with lower laser energy (and peak laser power). It is a natural question whether these targets can be used to produce energetic ions with a more powerful laser pulse.

Due to their relatively high mass, protons can be considered immobile on the time scales of the <100 fs pulses described in this dissertation and require a mechanism to mediate the transfer of laser energy to them so that they can accelerate. This is central to all laser-driven ion acceleration schemes. As for methods described

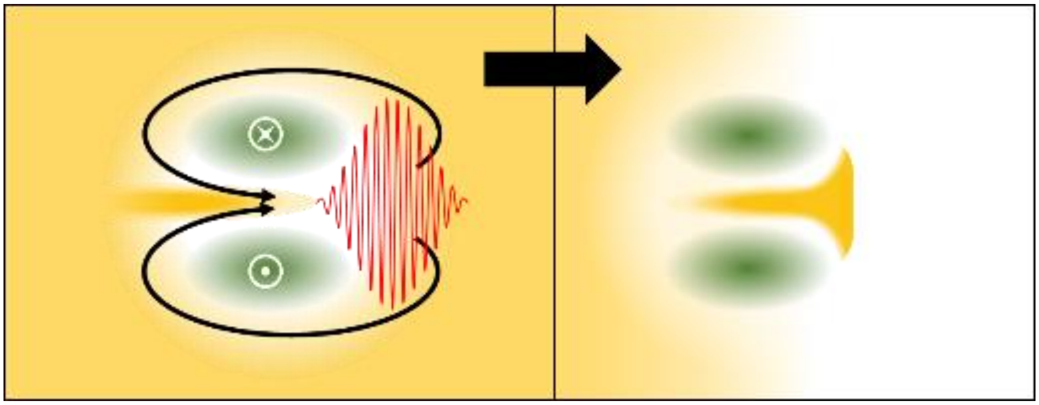

Figure 1.7Magnetic vortex acceleration. (Left) An intense laser pulse (red) propagates in a plasma (light orange). The strong ponderomotive force from the laser cavitates the electrons, and the return currents (dark orange) generate a toroidal magnetic field (green) which co-propagates with the laser. (Right) upon exiting the plasma, the magnetic torus is trapped on the downramp, pushing electrons forward and creating a polarization field which accelerates background ions.

in 1.4.1, this can be achieved through the transfer of energy to a hot electron population (as in TNSA), or an electrostatic shock (CSA). Other mechanisms using underdense plasma have been proposed using the beating of plasma waves [36], or the generation of strong magnetic fields through a processes called magnetic vortex acceleration [37]. In the case of acceleration via magnetic vortex, the time-averaged force that the laser exerts on the plasma expels electrons from the plasma wake which then create return currents in the form of a beam, generating a toroidal magnetic field that co-propagates with the laser. When the laser exits the plasma, the rapidly changing magnetic fields generate electric fields which acts on plasma electrons which then accelerate the ions.

1.5 Dissertation Outline

This dissertation summarizes several efforts to make laser-based particle accelerators more compact while still exploiting the high field gradients supported by plasma. In this chapter, the fundamentals of laser-based acceleration have been introduced, and the propagation of a laser in plasma described, specifically with respect to linear and nonlinear guiding of light. This nonlinear propagation can be broken into three regimes. In the weakly nonlinear regime, the laser drives a perturbatively small plasma wake, and diffracts in the absence of a preformed plasma channel. At higher densities or laser powers, the nonlinearity overcomes diffraction and the laser self-guides, driving a nonlinear plasma wake. At even higher intensities, the return currents in the plasma wake produce a strong magnetic field that causes non-negligible ion motion.

Chapter 2 is a description of the experimental tools used in subsequent chapters. A mode-locked Nd:YAG laser system and a synchronous Ti:Sapphire laser system are described, along with a variety of high-pressure cryogenic gas targets. The design, fabrication and characterization of a permanent magnet spectrometer is presented, along with an optical setup employing a spatial light modulator. The fundamentals of simulations used are also introduced.

Chapter 3 covers the formation of preformed plasma guiding structures in a clustered gas target. Two techniques are then presented for the development of density modulated plasma guiding structures. The first technique offers deep modulations while the second uses a spatial light modulator to achieve period tuning *in situ*. These structures can extend weakly relativistic interactions over many Rayleigh lengths and overcome dephasing.

Chapter 4 describes the propagation of an intense laser in a dense gas target in which the propagation is sufficiently nonlinear to self-guide. The spatio-temporal optical vortex, a new feature in nonlinear optics, is identified as an integral part of the relativistic self-guiding system. A dense hydrogen target is implemented to reduce the self-guiding threshold of the laser to sub-terawatt powers, and the resulting effects are discussed including electron injection, self-modulated laser wakefield acceleration, and the generation of broadband wavebreaking radiation.

Finally, Chapter 5 proposes a proton acceleration technique for the production of medical radio isotopes. The technique employs a very thin, near-critical gas target and relativistic filamentation, which results in a quasistatic magnetic field from plasma return currents. The results are presented in the context of cutting edge disk laser technology, which could enable the creation of a compact, high-repetition rate laser-proton source. A discrepancy in the previous literature is identified and addressed, and simulations show the efficacy of a high-repetition rate MeV-scale proton source. This is followed by Chapter 6, which summarizes the dissertation and describes the implications for future work.

Chapter 2: Experimental Apparatus and Simulation Tools

2.1 Laser Systems

2.1.1 High Power 140 ps Nd:YAG Laser

Two laser systems are used in the work of this dissertation. The first is a joule-class 140 ps Nd:YAG laser with a 1064 nm wavelength. It features a *Time Bandwidth GE-100* mode-locked Nd:Vanadate oscillator which outputs a 38 MHz pulse train of 18 nJ, 140 ps pulses. A Semiconductor Saturable Absorber Mirror (SESAM) provides the pulse steepening necessary to achieve mode-locking in the oscillator.

The 38 MHz pulse train is reduced to 10 Hz by a KD*P pulse slicer before entering a regenerative amplifier. The regenerative amplifier has a self-filtering unstable resonator (described in Appendix A.3.1) design which produces a high quality beam profile. [38] This cavity design uses a circular aperture and pair of curved end mirrors producing an Airy pattern whose central lobe passes through the aperture on each pass. This is described in detail in the appendix. The seeded output of the regenerative amplifier is kept at 12 mJ to avoid nonlinear self-focusing in the amplifier rod.

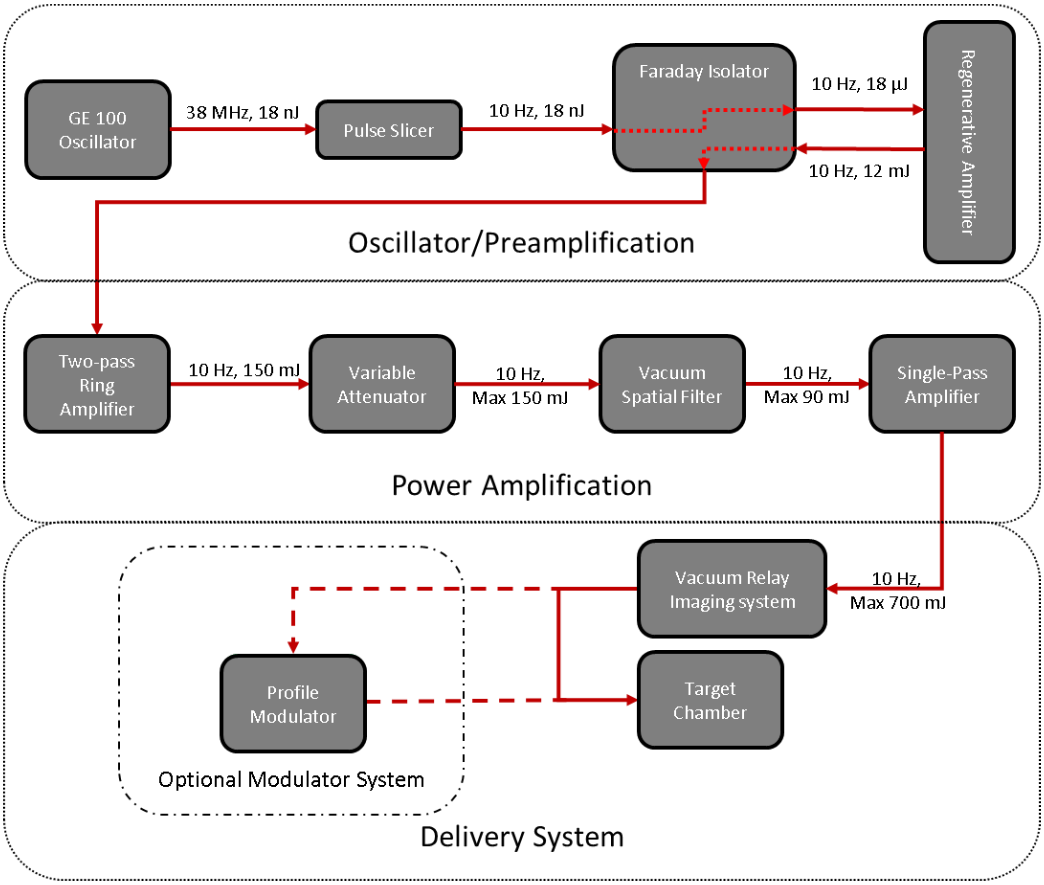

Figure 2.1 Schematic of 1J 140 ps Nd:YAG laser system. The oscillator is a Time-bandwidth GE100 mode-locked Nd:Vanadate system. The 18 nJ 38 MHz output is reduced to 10 Hz and amplified to 12 mJ. This is fed into the power amplification stage through a faraday isolator to protect the regenerative amplifier and oscillator from back-reflections. The power amplification stage consists of two amplifiers, separated by a vacuum spatial filter and a variable attenuator. The first amplifier brings the energy up to 150 mJ and is spatially filtered. The filtered beam is then amplified to a maximum energy of 700 mJ in a single-pass amplifier. Finally, the exit face of the final amplifier is imaged through a vacuum relay imaging system to the target. It is also possible to image to a profile modulator, which subsequently images to the target.

The output of the regenerative amplifier enters a two-pass ring amplifier, which amplifies it to 150 mJ. The energy is then reduced by a variable attenuator which ultimately determines the final pulse energy. The profile after the ring amplifier is poor quality so the profile is filtered in a vacuum spatial filter (VSF), where there is significant energy loss, bringing the energy down to 90 mJ. This then seeds the final amplifier which brings the energy up to 700 mJ.

The final amplifier exit face is vacuum relay imaged to the final focusing optic to deliver a flat-top beam profile. If the transverse profile is to be modulated (as described in Chapter 3), the face is first imaged to an interferometric profile modulator, before again relay imaging to the final focusing optic. A schematic of this laser is provided in figure 2.1, with details on certain components.

2.1.2 Ultrashort 25 TW Ti:Sapphire Laser

The second laser used is a Joule-class Ti:Sapphire chirped pulse amplification system. The output of an ultrashort mode-locked oscillator is stretched and amplified to joule-level energies, before being recompressed in vacuum and focused on target.

The oscillator is a Kerr-lens mode-locked *Coherent Micra* Ti:Sapphire system which outputs a 5 nJ pulse train at 76 MHz with a center wavelength of 810 nm and a bandwidth limit of 20fs. The pulses are stretched to 250 ps with a single grating stretcher and the repetition rate reduced to 1 kHz by a commercial acousto-optic programmable dispersive filter (AOPDF) [39]. This AOPDF also pre-compensates

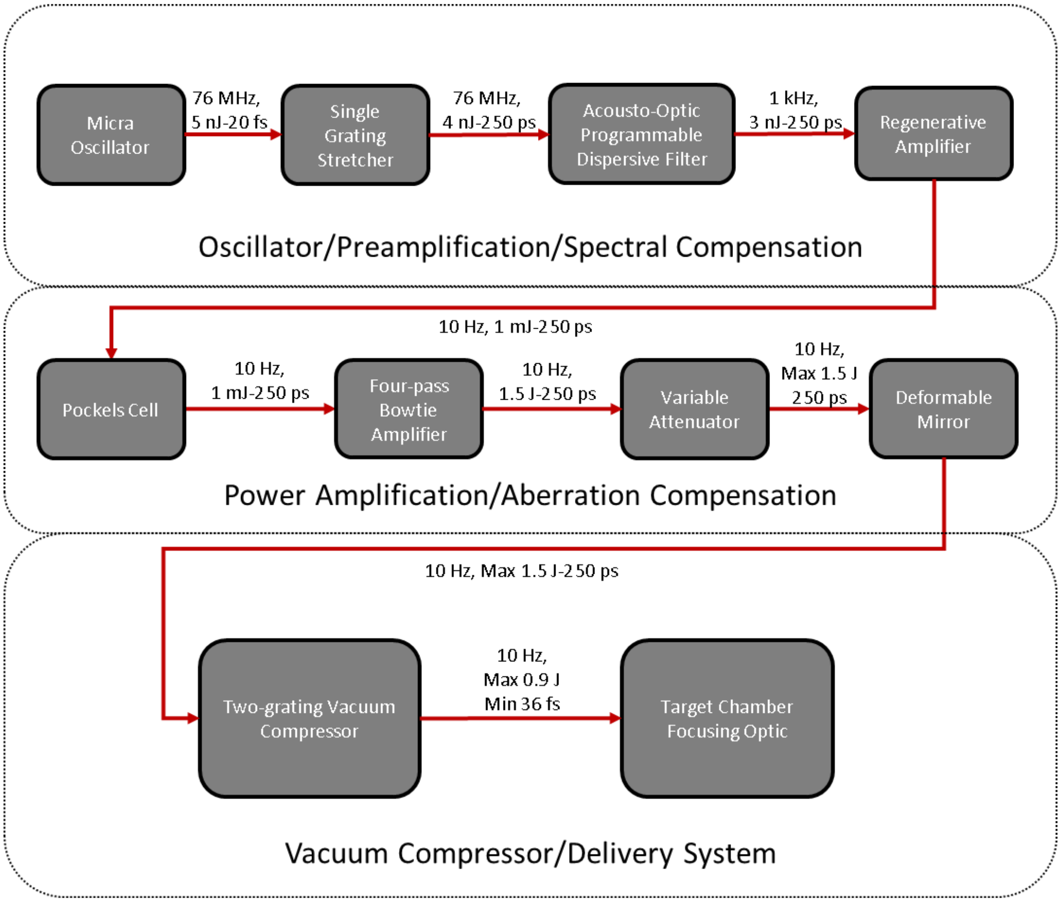

Figure 2.2 Schematic of Ti:Sapphire 25 TW laser system. A Coherent Micra oscillator outputs a 5 nJ 20 fs pulse train at 76 MHz This pulse is stretched to 250 ps and amplified to 1 mJ after being spectrally pre-compensated by an Acousto-Optic Programmable Dispersive Filter which reduces the repetition rate to 1 kHz. This pulse train is reduced to 10 Hz by a Pockels cell before entering a four-pass bowtie amplifier which amplifies the pulse to 1.5 J. The energy of the pulse is reduced by a variable attenuator and aberration pre-compensation by a deformable mirror before entering the vacuum portion of the system. The pulse is compressed in vacuum by a two-grating compressor to a minimum pulse length of 36 fs and focused by an off-axis parabola.

the spectral phase and amplitude of the seed pulses in order to mitigate gain narrowing and higher order dispersion within the laser, enabling compression of the amplified pulse to near-bandwidth limits.

The stretched and spectral amplitude/phase compensated kHz pulse train is amplified in a regenerative amplifier to 1 mJ. Due to gain narrowing, the bandwidth of the pulse reduces by a factor of two, increasing the bandwidth-limited compressed pulse to about 40 fs.

The output of the regenerative amplifier is reduced to a 10 Hz repetition rate by a Pockels cell and enters a four-pass bowtie amplifier. The pulse is amplified to 1.5 J and the final pulse energy is adjusted using a variable attenuator. A deformable mirror pre-compensates for focusing aberrations, and the pulse is compressed in vacuum by a pair of gratings before being sent to one of two target chambers, where it is focused on target by an off-axis paraboloid. Figure 2.2 outlines this laser system.

2.1.3 Laser System Synchronization

The *Micra* oscillator for the Ti:Sapphire system uses a piezoelectric actuator within the cavity for a tunable pulse repetition rate. By actively adjusting the repetition rate, the oscillator pulse train can be synchronized to an external 76 MHz (or 38 MHz) RF signal. Using a photodiode signal from the Nd:YAG system's mode-locked Nd:Vanadate oscillator as the master oscillator, the two mode-locked systems can be synchronized to each other.

When the laser systems are synchronized, the Nd:YAG system's mode-locked Nd:Vanadate oscillator is used as the master clock for both laser systems, triggering all timing boxes, Pockels cells, cameras, and the solenoid valve of the target. The Ti:Sapphire system can also be run without the synchronization system, in which case the *Micra* acts as the master clock for the experiment.

2.2 High Pressure Cryogenic Gas Target

2.2.1 Elongated Nitrogen Cluster Jet

Two targets were used in the following work. The first is an elongated N_2 cluster jet, used to preform plasma waveguides. The target is formed using a Parker-Hannifin series-99 solenoid valve. This valve is cooled to liquid nitrogen temperatures through its copper mounting block. This mounting block was cooled with a 22 psi flow of liquid nitrogen, and its temperature controlled by an electrical heating element. A thermocouple mounted on the copper block was used in a feedback loop with the heating element to allow temperature control of the target.

The solenoid valve was pressurized with nitrogen in the range of 200-1000 PSI, adjusted with a high pressure regulator. The low temperatures and high pressures of the solenoid valve allow for cluster formation after throttling into vacuum. Van-Der-Waals forces cause clusters to form as the gas adiabatically expands and cools. [40]

The flow of these clusters is nearly ballistic [41] and is confined by a pair of variably sized side walls or “jaws” separated by the orifice size (0.5 – 1 mm). The confined flow exits the jaws as a fan, at which point it is irradiated by an intense laser pulse. In earlier work [12], these jaws were stainless steel. In the experiments of this dissertation, new jaws were manufactured out of PTFE (Teflon) for its better resistance to damage by high power laser radiation and laser-heated plasma. An added benefit is reduced coating of nearby optics with material ablated from the jaws.

End-coupling of injected focused pulses into a plasma waveguide is best if the entrance is sharp compared to the Rayleigh range of the focused pulse, so it is desirable that the edges of the expanding cluster fan have a high-contrast dropoff to vacuum. This was achieved using 100 μm thick sapphire skimmers on top of the jaws. The skimmers were affixed using Teflon tape and were robust to irradiation by channel forming pulses and by ambient laser-heated plasma. The cluster fan was characterized by the plasma produced when irradiated with a channel-forming pulse. Phase shift images were extracted from interferograms, showing a sharp entrance density gradient scale length of ~250 μm.

2.2.2 Thin, Dense, Cryogenically Cooled Gas Jet

Another jet was subsequently developed, using the same Parker-Hannifin series-99 solenoid valve, outfitted with an 800 μm diameter orifice head. Two generations of nozzles were developed with ~100 μm diameter orifices. These were coupled to the orifice head to produce a thin and dense gas flow target.

Like the elongated cluster target, the valve was mounted in a copper cooling block. To achieve more effective cooling of the hydrogen gas, the block was designed with a heat exchanger to pre-cool the target gas, and more effectively cool the mounting block.

The first generation of nozzles were constructed from thin steel tube. Under operating conditions, the high intensity interaction slowly erodes the nozzle tip,

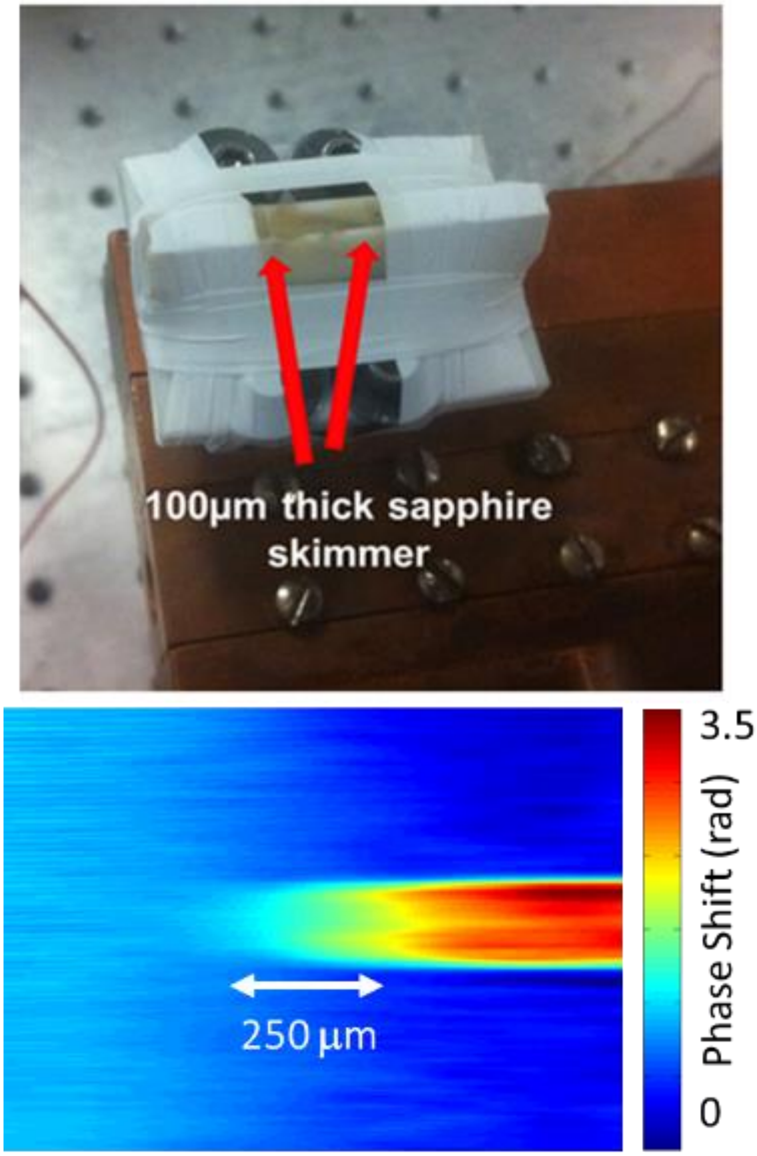

Figure 2.3 An elongated nitrogen cluster jet. A Parker-Hannifin series-99 solenoid valve is mounted in a copper cooling block. A pair of Teflon guiding walls (off-white) confine the expanding gas flow to a fan as clusters precipitate. A pair of 100 μm sapphire skimmers (indicated by red arrows) are affixed to the top of the jaws to produce high contrast edges to the cluster fan using Teflon tape (bright white).

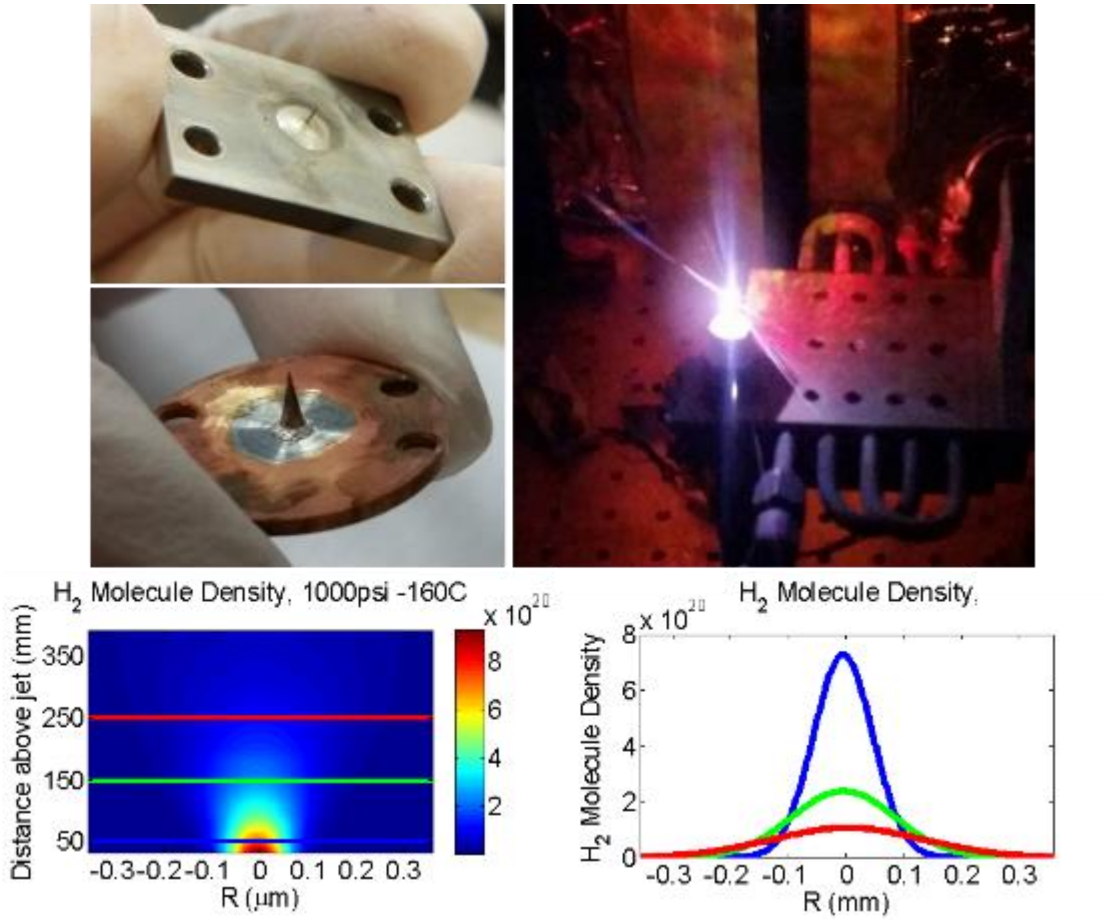

Figure 2.4 Thin-dense hydrogen gas targets. A Parker-Hannifin series-99 solenoid valve is mounted in a copper cooling block. This cooling block (right) acts as a heat exchanger between a flow of liquid nitrogen and the high pressure hydrogen reservoir. The first generation of nozzles (top left) consisted of a thin needle. Modern versions (bottom left) use a hollow, conical tip.

mainly from plasma-induced erosion, but also from laser interaction. The nozzle was regularly refreshed using low power Ti:Sapphire pulses in atmosphere to square off the tip.

The second generation of these nozzles replaced the tube with a hollow conical shape. This allows for a gradual reduction of flow from the orifice to the nozzle tip.

These targets also use a temperature control system. To adjust target density, the reservoir backing pressure was vary between 200 and 1100 PSI. Target neutral gas densities were measured using transverse interferometry. Phase shifts were extracted from interferograms and density was extracted by Abel inversion about the jet axis. Traces of the neutral gas imply near-critical plasma densities for Ti:Sapphire.

2.3 Experimental Diagnostics and Devices

2.3.1 Transverse Spectroscopy and Interferometry

Figure 2.5 shows the target chamber with the various diagnostics for the interaction region. The interaction region is probed for ultrafast transverse interferometry with a frequency doubled portion of the main Ti:Sapphire pulse. The probe beam is imaged from the interaction region into a folded wavefront interferometer. Shadowgrams (phase contrast images) are obtained by blocking one of the arms of the interferometer. With the probe blocked, a flip mirror can redirect light from the interaction region to a fiber spectrometer.

The folded wavefront interferometer splits the probe pulse after passage through the target. The probe is split so that the portion of the beam that is phase shifted by the target is recombined and interfered with an unshifted portion, which acts as a reference. In the interferometric probing plasma waveguides generated in clustered gases, the reference region was a region of uniform clustered gas above the plasma. In probing of thin gas jet targets, the portion of the beam passing through vacuum regions horizontally displaced from the interaction region were used as reference.

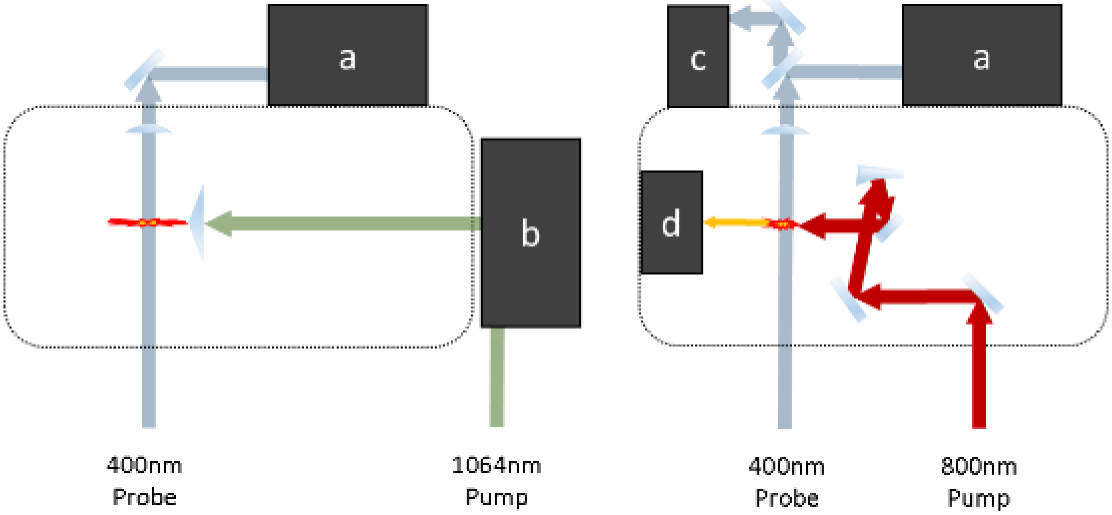

Figure 2.5 Target chamber diagnostics, (a-d). In the left configuration, a 1064 nm pump pulse generates a waveguide which is probed with a synchronous 400 nm ultrashort pulse. In the right configuration an 800 nm pump pulse generates a plasma in a thin, dense gas target which is probed by a synchronous 400 nm pulse. a) The probe enters a folded wavefront interferometer imaging the interaction region. b) A beam profile modulation system which can be bypassed. c) With the 400 nm probe blocked, a flip mirror directs the light from the interaction region into a fiber spectrometer. d) a charged particle spectrometer with a permanent magnet dispersive element.

2.3.2 Liquid Crystal on Silicon Spatial Light Modulator

Liquid crystal is a state of matter which exhibits some properties of a liquid, while maintaining some form of long-range order. The spatial light modulator (SLM) used in of the experiments of this dissertation is a nematic liquid crystal on a silicon substrate. Nematic liquid crystals are composed of uniaxial molecules with a high aspect ratio having long-range rotational (alignment) order, but with no long-rage translational order. In the SLM used, alignment layers orient the liquid crystal along the SLM face, creating a slow axis for light polarized parallel with the liquid crystal orientation and a fast axis for light polarized perpendicular to it.

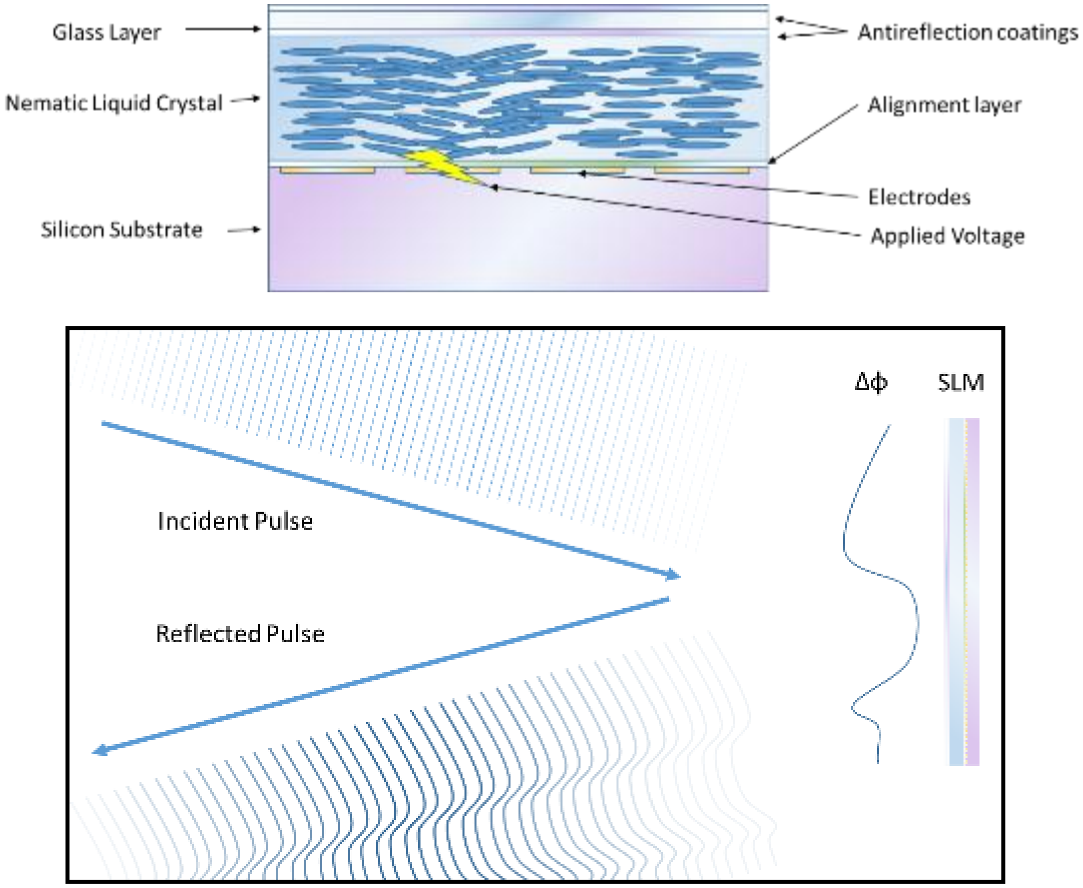

Figure 2.6 Liquid Crystal-on-Silicon Spatial Light Modulator. (Top) Nematic liquid crystal is oriented by an alignment layer to produce an extraordinary axis in the liquid crystal layer. A voltage applied to an electrode locally disturbs the liquid crystal orientation. This produces a perturbation on the local refractive index. (Bottom) Using an array of these electrodes, an incident laser can be patterned with a phase-shift profile Δφ.

The silicon substrate is written with 475200 electrodes in a 600x792 array. When an electrode is active, the nearby molecules re-orient, altering the local refractive index. When the polarization of incident light is aligned with the extraordinary axis, a phase shift profile is imprinted on the reflected light. If the polarization has components along the ordinary and extraordinary axes, a polarization profile is imprinted on the reflected light, as determined by the local relative speeds of fast and slow axes. When used with crossed polarizing optics, polarization rotation can be used as a means of amplitude modulation.

There are limitations on the use of SLMs, often due to their low damage threshold. Damage can arise either from high intensities or high average powers. If the SLM is subject to damage from high intensities, the liquid crystal molecules, alignment layers, printed electrodes or optical coatings can be permanently damaged. When subject to high average power, the SLM can heat up. Before permanent damage, the first effect is for the liquid crystal to “melt,” losing its rotational order. Though the latter process is reversible, it renders the SLM ineffective for several hours until the liquid crystal recrystallizes. Identifying the lack of phase shift from an applied voltage can be a means of measuring damage thresholds on SLMs. Table 2.1 shows results from Hamamatsu for the SLM used in the following work.

To avoid damage an apparatus was designed to minimize laser fluence on the SLM. The SLM was used to phase-modulate a low energy beam for interferometric recombining with a high energy beam.

Light Source						Irradiation intensity		Peak Power		Result	
Type	Wavelength (nm)	Pulse Width	Repetition frequency (kHz)	Beam size (mm) [at $1/e^2$]	Irradiation time (hours)	Average output power (W)	Output power per area (W/cm^2)	Peak output power	Output power per area	Damage	Characteristic change
YAG laser (cw)	1064	-	-	Φ 2.5	1	2.0	41.0	-	-	Not Seen	Not Seen
YAG laser (cw)	1064	-	-	Φ 2.5	Several minutes	3.5	71.0	-	-	Not Seen	Seen
YAG laser (pulse)	1064	200 ns	80	Φ 2.5	1	2.0	41.0	0.2kW	1.4 kW/cm^2	Not Seen	Not Seen
YAG laser (pulse)	1064	200 ns	80	Φ 2.5	Several minutes	3.5	71.0	0.2kW	1.4 kW/cm^2	Not Seen	Seen
Pulse laser	1030	670 fs	1	Φ 24.5	10	0.6	3.6	0.86 GW	5.4 GW/cm^2	Not Seen	Not Seen
Pulse laser	1030	1.37 ps	30	Φ 8.11	8	5.2	10.0	0.12GW	0.24 GW/cm^2	Not Seen	Not Seen
Pulse laser	1030	11.4 ns	10	Φ13	8	17.4	13.1	0.15 kW	0.11 kW/cm^2	Not Seen	Not Seen

Table 2.1 Damage threshold measurements of Hamamatsu LCOS-SLM. Though a 140 ps system was not used in these tests, it is prudent to stay below the peak power described in the blue row and the average power described in the red row.

2.3.3 Electron Spectrometer

To characterize electron beams produced by laser-driven plasma accelerators, a permanent magnet electron spectrometer was developed. The goal was to create a spectrometer that could characterize a wide variety of electron energies without heat load from magnet coils. The spectrometer would be in vacuum, so heat would not dissipate quickly. To avoid the heat load, permanent magnets were used.

A yoke was machined out of iron, with a pair of aluminum mounting brackets to hold neodymium (N42) magnets along with iron spacers. The brackets were designed to allow a series of magnets with thickness ranging from ½ inch to 1/32 inch to be affixed to the magnet yoke. A pair of spacers was designed for each pair of permanent magnets to keep the geometry the same between different field strength configurations. Figure 2.7 shows the dispersive element and its parts.

The field in the magnet gap was characterized by gauss probe measurement of the field at the magnet faces. For this measurement, the 1/8th inch thick magnets were used. The field within the gap was then calculated with Laplace's equation for the magnetic scalar potential using the method of relaxation [42], with measured fields as the boundary conditions at the pole faces and zero potential at all other boundaries. A measurement made of the mid-plane magnetic field was compared to the computed mid-plane field, confirming an accurate solution. These results are shown in figure 2.8. This process is described in greater detail in Appendix A.1.2.

The 3D field map was then imported into *Cyber-Ray* ray-tracing software [43]. Our charged particle spectrometer was simulated using the imported B-

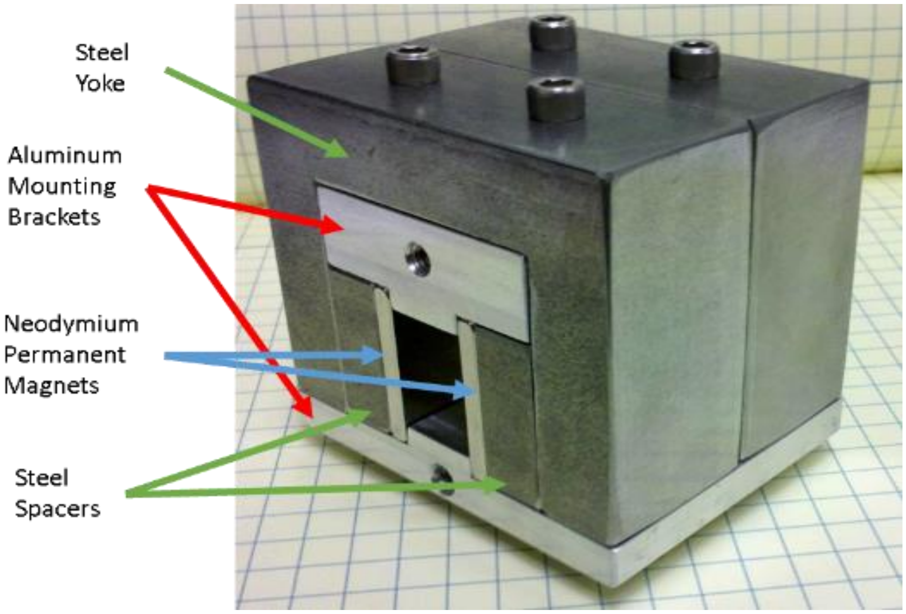

Figure 2.7 Permanent magnet dispersive element. Neodymium magnets (blue) provide a source of magnetic field with no heat load. The steel yoke and spacers (green) confine the magnetic field to magnet gap, simplifying dispersion modeling. Aluminum mounting brackets provide support and a means to mount the element.

field and a diagnostic surface at the scintillator location which recorded particle position and momentum. Simulating a broadband particle source an energy vs. screen position curve was calculated. To estimate energy curves for other magnets, the field strength was scaled with a constant multiplicative factor and the new curve calculated in *CyberRay*. Energy curves for both electrons and protons for various magnet configuration are shown in Appendix A.3.2.

The full spectrometer was then assembled in the target chamber according to the final design from ray-tracing. Lanex scintillator film [44,45], on which the electron beams were dispersed by the magnet, was placed 10 inches from the magnet. The resulting Lanex fluorescence pattern, constituting the electron beam spectrum, was imaged to an *Andor* Electron Multiplying CCD (EMCCD). The Lanex film was protected from laser light by 25μm Al foil, through which the relativistic e-beam readily passed.

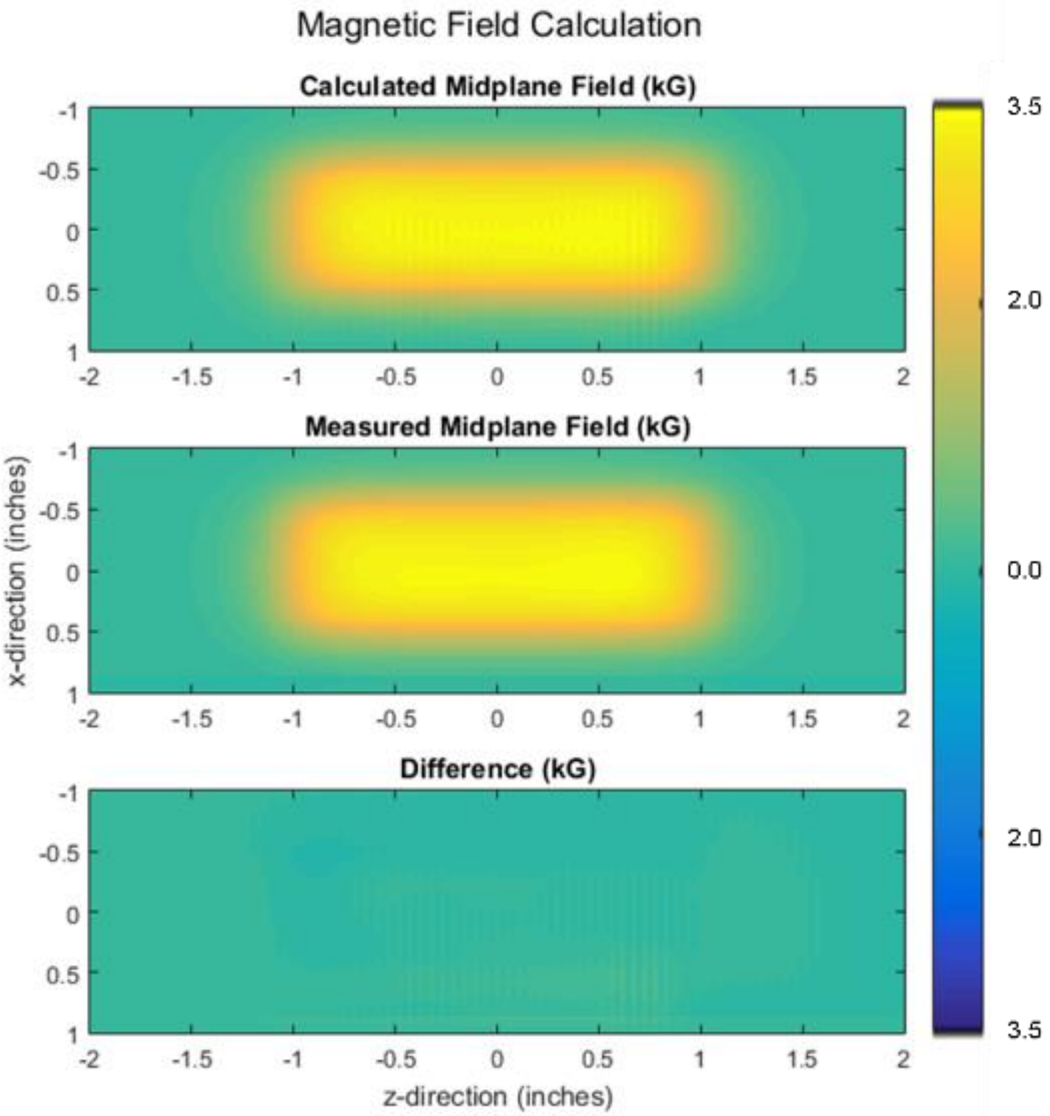

Figure 2.8 Accuracy of calculated magnetic field. The top magnetic field is the mid-plane out-of-plane magnetic field calculated using measurements of the in-plane magnetic field as boundary conditions for a solver of Laplace's equation. The middle magnetic field is a measurement of the mid-plane out-of-plane field, which is qualitatively similar. The difference between fields, shown at the bottom, confers good agreement on the order of 1%, mostly attributable to artifacts from the field solver.

2.4 Particle-in-cell Simulations

2.4.1 The Particle-in-Cell Method

In order to model the nonlinear dynamics of an intense laser-plasma interaction, simulations were implemented using the TurboWAVE particle-in-cell (PIC) code [46]. In these simulations, field quantities like electric field, charge density, and current density, are defined on a discrete grid. Within this grid, a number of “macroparticles” are defined which have positions as well as momenta in a continuous phase space. Upon advance of the time step, the motion of these macroparticles is updated based on an interpolation of the local field quantities and likewise, the field quantities are updated based on an interpolation of the particle positions and velocities. This is illustrated in figure 2.9This method is much faster than calculating a full 6D phase space, but still captures the kinetic dynamics which follow from having multi-valued velocities within a grid cell.

In the years since its initial development, the PIC model itself has been a field of study [47], with advances in computational optimization [48], geometric approximation [49,50], particle collision and generation [51], and hardware utilization [52]. As a result, many published codes have become effective tools to support theory as well as experiment. The code used within this dissertation is TurboWAVE [53], and has been under continuous development at the Naval

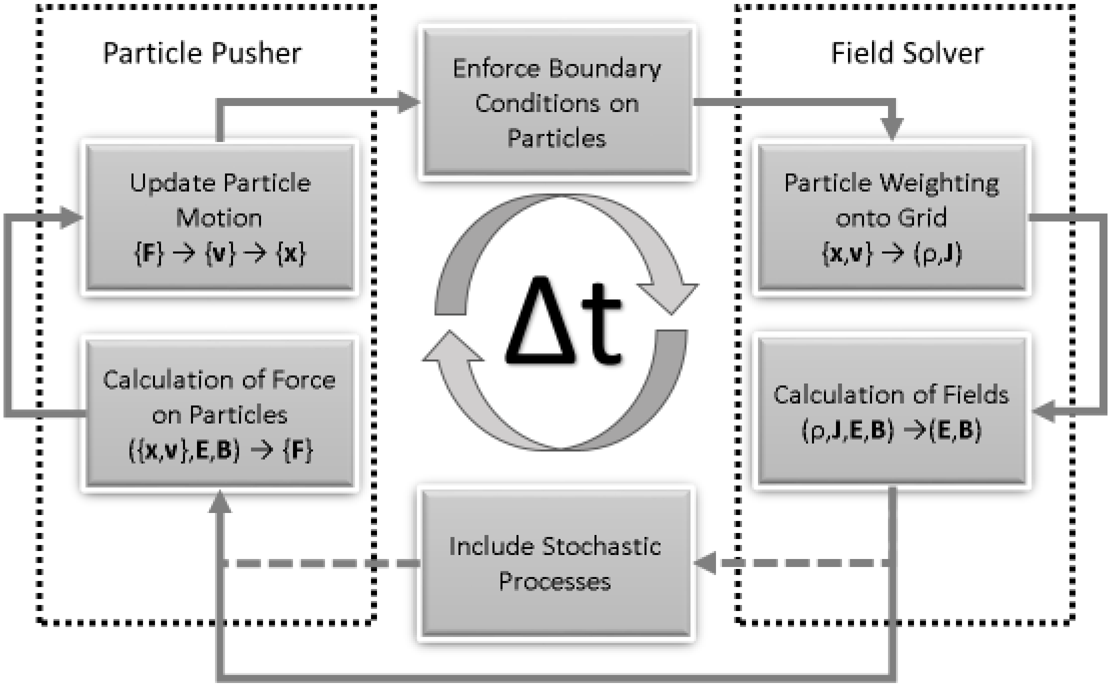

Figure 2.9 Flow chart for computations using the Particle-in-Cell method. On each time step, charge and current densities are calculated by weighting particles on to the grid. Electric and magnetic fields are calculated from the corresponding grid values. If stochastic processes are being simulated, like collisions, ionization, radiation reaction, or particle generation, they can be implemented here, though this feature is not implemented in this work. An impulse on each of the particles is calculated and the particle phase space is updated. Using the updated particle positions, the boundary conditions on particles is enforced, and the process repeats in the next time step.

Research Lab. The details of this code are beyond the scope of this work, but some fundamental information will be provided here.

2.4.2 Particle Pushing

In a PIC code, the 6D particle phase space is represented by a collection of “macroparticles,” which have positions and momenta defined in 6D phase space, collectively emulating the phase space of a much larger number of particles. On each time step, each macroparticle’s position and momentum are updated. The change in the particle’s momentum is calculated by interpolating the E and B fields at the particles position. The particle’s velocity is then calculated from its momentum which is then used to update the particle's position. The particles' position and velocity are then used to calculate the charge and current density on the grid.

2.4.3 Field Solvers

The current and charge densities (**J** and ρ) are calculated from the particle position and velocity by distributing their charge and current onto their surrounding grid points. Electric and magnetic fields, **E** and **B** are then calculated using **J** and ρ along with **E** and **B** from the previous time step. The leapfrog technique reduces error by defining charge density and magnetic field on half time steps, error is reduced. The fields are defined on a grid, using the standard Yee mesh [54], wherein different quantities are defined at different points within a grid cell which also reduces error.

On a grid cell with corner at point (i,j,k), the charge density is defined on the corners. The current density and electric field components are defined on the edges of the cell, offset by half a cell width in the component direction. Finally, the magnetic field components are defined on the cell face, offset by half a cell width in the two directions that are not the component direction. This method reduces error when solving Maxwell's equations directly. Figure 2.10 provides a diagram of the Yee mesh.

The Yee mesh is designed such that values are calculated from differences which are centered on the calculated values. Maxwell's equations can be discretized in space and time before being solved as follows.

$$\Delta_x E_x[i,j,k] + \Delta_y E_y[i,j,k] + \Delta_z E_z[i,j,k] = 4\pi\rho[i,j,k] \tag{2.1a}$$

$$\Delta_x B_x[i+\tfrac{1}{2}, j+\tfrac{1}{2}, k+\tfrac{1}{2}] + \Delta_y B_y[i+\tfrac{1}{2}, j+\tfrac{1}{2}, k+\tfrac{1}{2}] + \Delta_z B_z[i+\tfrac{1}{2}, j+\tfrac{1}{2}, k+\tfrac{1}{2}] = 0 \tag{2.1b}$$

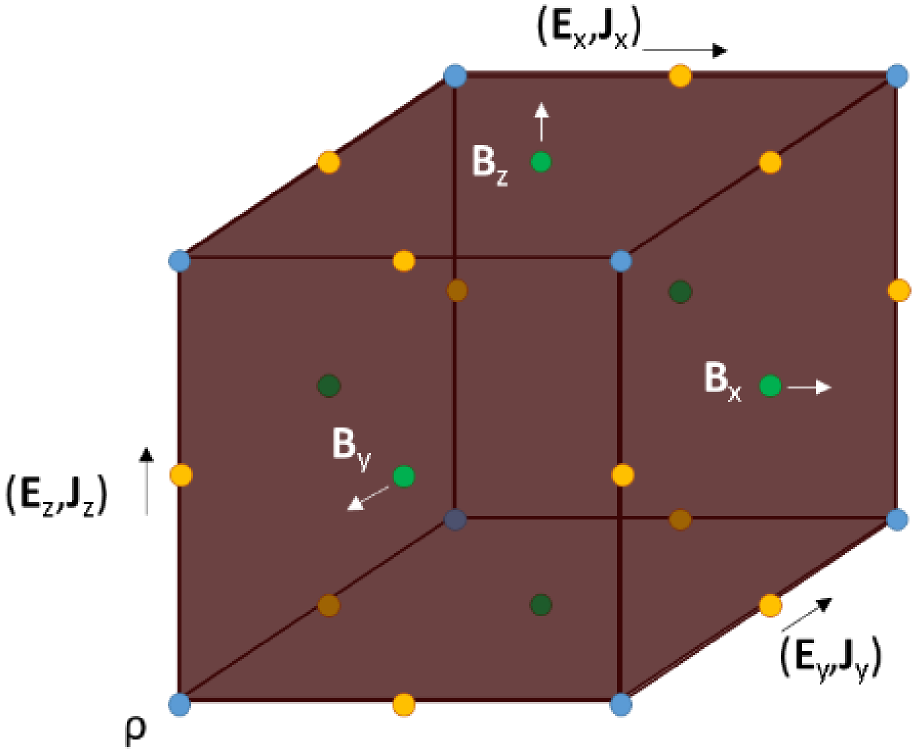

Figure 2.10 The Yee Mesh. A single cell is depicted, with colored dots representing different values. Charge density (blue) is defined on the corners of the cell, current density and electric (yellow) field are defined on the edges of the cell, each component offset in its own direction. Magnetic field (green) is defined on cell faces, the normal of each face parallel to the component direction. With this configuration, each field is calculated from center-differences of values only one half-step in the necessary direction.

$$\begin{aligned}
&\Delta_y E_z[i, j+\tfrac{1}{2}, k+\tfrac{1}{2}] - \Delta_z E_y[i, j+\tfrac{1}{2}, k+\tfrac{1}{2}] = -\tfrac{1}{c}\,\Delta_t B_x[i, j+\tfrac{1}{2}, k+\tfrac{1}{2}] \\
&\Delta_z E_x[i+\tfrac{1}{2}, j, k+\tfrac{1}{2}] - \Delta_x E_z[i+\tfrac{1}{2}, j, k+\tfrac{1}{2}] = -\tfrac{1}{c}\,\Delta_t B_y[i+\tfrac{1}{2}, j, k+\tfrac{1}{2}] \qquad (2.1c) \\
&\Delta_x E_y[i+\tfrac{1}{2}, j+\tfrac{1}{2}, k] - \Delta_y E_x[i+\tfrac{1}{2}, j+\tfrac{1}{2}, k] = -\tfrac{1}{c}\,\Delta_t B_z[i+\tfrac{1}{2}, j+\tfrac{1}{2}, k]
\end{aligned}$$

$$\begin{aligned}
&\Delta_y B_z[i+\tfrac{1}{2}, j, k] - \Delta_z B_y[i+\tfrac{1}{2}, j, k] = \tfrac{1}{c}\left(4\pi J_x[i+\tfrac{1}{2}, j, k] + \Delta_t E_x[i+\tfrac{1}{2}, j, k]\right) \\
&\Delta_z B_x[i, j+\tfrac{1}{2}, k] - \Delta_x B_z[i, j+\tfrac{1}{2}, k] = \tfrac{1}{c}\left(4\pi J_y[i, j+\tfrac{1}{2}, k] + \Delta_t E_y[i, j+\tfrac{1}{2}, k]\right) \qquad (2.1d) \\
&\Delta_x B_y[i, j, k+\tfrac{1}{2}] - \Delta_y B_x[i, j, k+\tfrac{1}{2}] = \tfrac{1}{c}\left(4\pi J_z[i, j, k+\tfrac{1}{2}] + \Delta_t E_z[i, j, k+\tfrac{1}{2}]\right)
\end{aligned}$$

With center-differencing,

$$\begin{aligned}
\Delta_t G[i,j,k]\big|_{t=n} &\equiv \frac{1}{\Delta t}\left(G[i,j,k]\big|_{t=n+1/2} - G[i,j,k]\big|_{t=n-1/2}\right) \\
\Delta_x G[i,j,k] &\equiv \frac{1}{\Delta x}\left(G[i+\tfrac{1}{2},j,k] - G[i-\tfrac{1}{2},j,k]\right) \\
\Delta_y G[i,j,k] &\equiv \frac{1}{\Delta y}\left(G[i,j+\tfrac{1}{2},k] - G[i,j-\tfrac{1}{2},k]\right) \\
\Delta_z G[i,j,k] &\equiv \frac{1}{\Delta z}\left(G[i,j,k+\tfrac{1}{2}] - G[i,j,k-\tfrac{1}{2}]\right)
\end{aligned} \tag{2.2}$$

A consequence of this discretization is the introduction of a degree of freedom in the ratio of time step size to spatial grid size. This can be seen by considering an electromagnetic wave traveling in the z-direction with x-polarization,

$$\Delta_z \Delta_z E_x[i+\tfrac{1}{2},j,k] = \frac{\Delta_t \Delta_t}{c^2} E_x[i+\tfrac{1}{2},j,k] \tag{2.3}$$

Substituting $E_x = \exp(i(\kappa z - \omega t))$, the difference terms take the form,

$$\begin{aligned}
\Delta_z \Delta_z E_x[k,\tau] &= \frac{1}{\Delta z^2}\exp(i(\kappa(k\Delta z) - \omega(\tau\Delta t)))\left(\exp(i(\kappa\Delta z)) - 2 + \exp(i(\kappa\Delta z))\right) \\
\Delta_t \Delta_t E_x &= \frac{1}{\Delta t^2}\exp(i(\kappa(k\Delta z) - \omega(\tau\Delta t)))\left(\exp(i(\omega\Delta t)) - 2 + \exp(i(\omega\Delta t))\right)
\end{aligned} \tag{2.4}$$

This can be used to solve for the dispersion relation,

$$\cos(\omega\Delta t) - 1 = \frac{c^2\Delta t^2}{\Delta z^2}\left(\cos(\kappa\Delta z) - 1\right) \tag{2.5}$$

As illustrated in figure 2.11, the dispersion relation for finite difference system can be seen to differ from the continuous solution for $\Delta z/\Delta t \neq c$, with some frequencies experiencing unstable growth for $\Delta z/\Delta t > c$. In practice, this means that the step size must be chosen to yield a light speed as close to c as possible without causing unstable growth. This is known as the Courant condition.

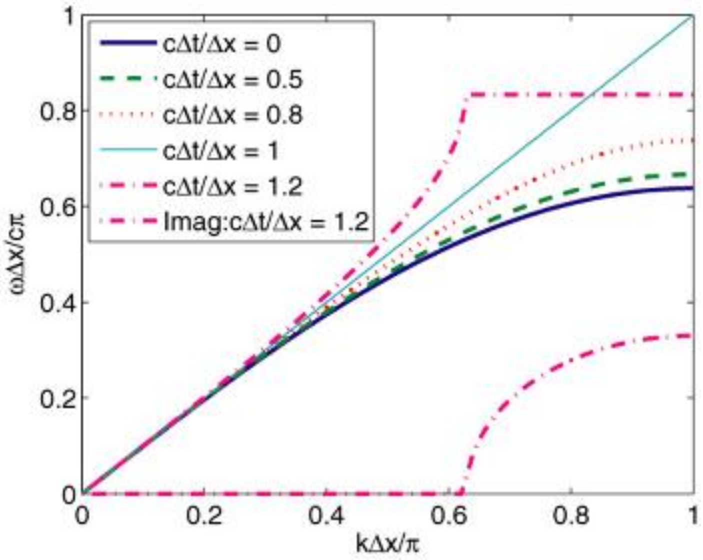

Figure 2.11 Dispersion relation for the finite difference approximation to the wave equation for different ratios of step size to cell size. At ratios above the speed of light, a positive imaginary component emerges at high wave numbers, causing unstable growth. Figure from [54]

Finally, TurboWAVE supports "moving window" solvers. In this case, the region which is being simulated is translating at a constant speed with respect to the simulated system. This allows a simulation to closely follow a laser pulse as it travels through a plasma, reducing window size requirements and providing significant speedup.

2.5 Laser-Target Configurations

2.5.1 Clustered Nitrogen Waveguides

Three different laser-target configurations were implemented. The first configuration employs the elongated cluster target with 140 ps Nd:YAG system. Laser pulses ranging in energy from 150 mJ to 500 mJ is focused with an axicon to a line in the elongated cluster jet. The resulting plasma is probed with a λ=400nm, ~50 fs, frequency-doubled portion of the main Ti:Sapphire laser pulse.

The Ti:Sapphire system is actively synchronized to the Nd:YAG system by a coherent *Synchrolok* phase locked loop system as discussed earlier in section 2.1.3. This allows use of the λ=400nm probe pulse for high time resolution interferometry of plasma waveguide formation by the 140ps duration Nd:YAG laser pulse.

For a portion of the experiment, the 35 fs λ=800nm main pulse from the Ti:Sapphire with 200 mJ of energy was used to generate waveguides by focusing it with an f/25 spherical mirror.

2.5.2 Dense Jet with f/9 Focusing

In the second configuration the Ti:Sapphire laser pulse is focused with 10-50 mJ of energy into a thin, dense gas target. The resulting spot size is 8.5 μm FWHM. The same frequency doubled probe used in 1.5.1 is used to probe the plasma. At very high plasma densities, diffraction from the plasma causes strong intensity variations on the probe and the phase shift cannot be directly extracted from interferograms. Instead, plasma densities can be inferred through a measurement of the neutral gas density before ionization. To measure spectra of side-scattered laser light and light transversely emitted from the plasma, a flip mirror can redirect the image of the interaction region to a fiber spectrometer with a range of 200nm-1100nm.

Finally, the electron spectrometer described in section 2.3.2 was used to characterize forward-directed electrons. With the electrons dispersed downward, a horizontal slit aperture can give information about the angular dependence of the

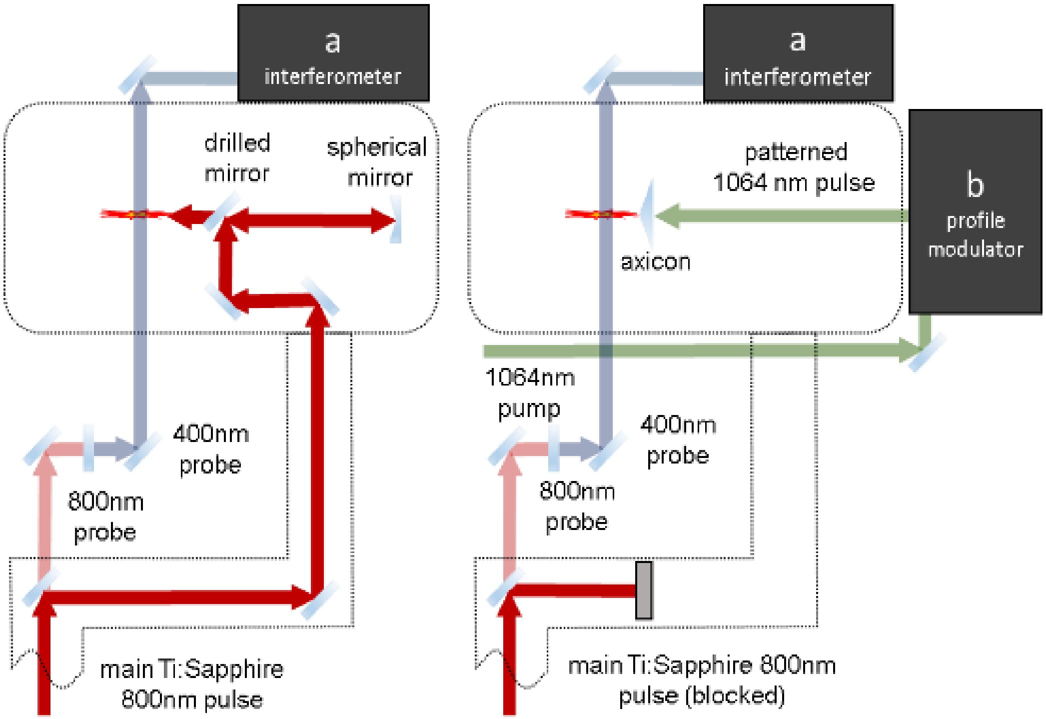

Figure 2.12 Nitrogen waveguide target configuration. (Left) A high power 800 nm pump pulse is focused with an f/25 spherical mirror over an elongated nitrogen cluster jet. (Right) A high power, 1064 nm pump pulse (green) is focused with an axicon to produce a plasma waveguide after being patterned in a profile modulator (b) to produce modulated plasma waveguides discussed in Chapter 3. A synchronous 800 nm probe pulse (red) is frequency doubled (blue) and probes the resulting waveguide. This is directed in to a folded wavefront interferometer (a).

electron spectrum. The magnet and aperture can be removed to expose the Lanex to the full electron beam to characterize the transverse profile, measure beam divergence, and estimate total accelerated charge.

2.5.3 Dense Jet with f/3 Focusing

A setup similar to that in Section 2.5.2 was devised to study ion acceleration. In this configuration, the Ti:Sapphire is focused with 500mJ-1J of energy by an f/3 off-axis paraboloid to a 3μm FWHM spot size in a 100μm hydrogen gas jet with molecule densities capable of producing near-critical density plasmas. A replica of the charged particle spectrometer described in section 2.3.2 was fabricated. The target uses a more advanced cooling system with a set of actuated obstructions to augment the target density. The ion-acceleration simulations of Chapter 5 use a similar geometry.

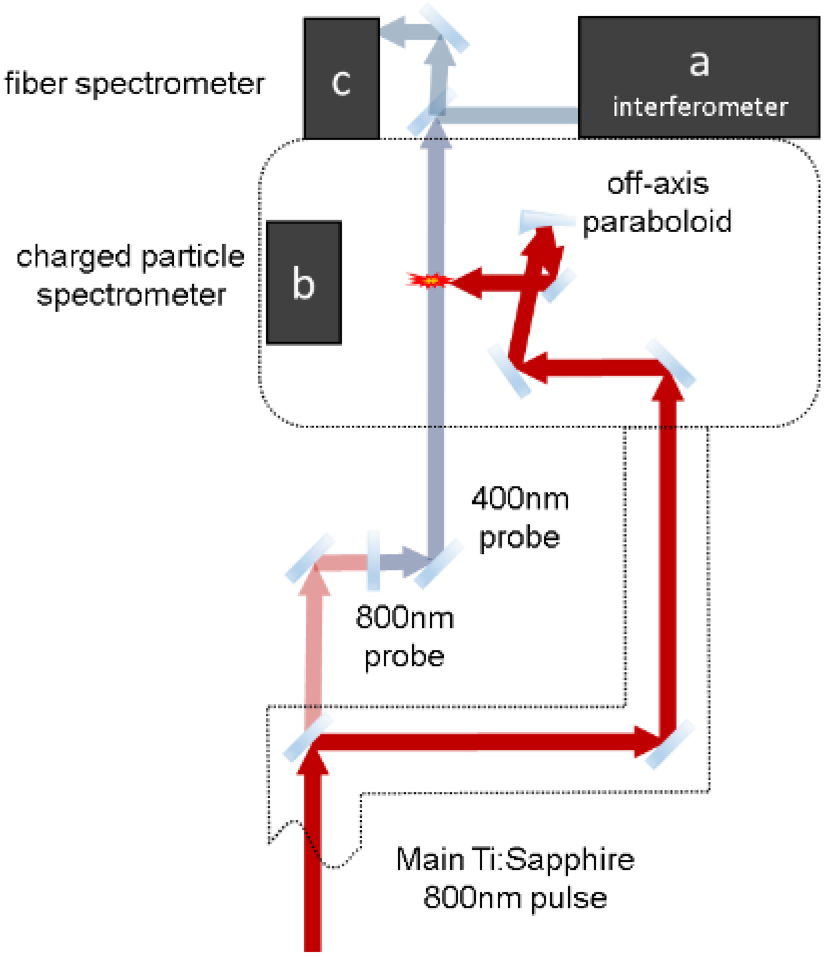

Figure 2.13 Dense gas jet configuration. An intense 800 nm pump pulse (red) is focused into a thin dense hydrogen jet by an off-axis paraboloid. A small portion of the pulse is frequency doubled (blue) before probing the interaction region and entering a folded wavefront interferometer (a). Electrons generated from the interaction are analyzed in a permanent magnet charged particle spectrometer (b). With the probe beam blocked, a flip mirror allows light generated in the interaction region to be imaged into a fiber spectrometer (c).

Chapter 3: Generation of Modulated Plasma Waveguides

3.1 Modulated Plasma Waveguides for Electron Acceleration

A plasma waveguide can extend the interaction of a laser pulse with an electron bunch over many Rayleigh ranges, while still withstanding the high optical fields necessary for acceleration [11]. Such a guiding structure in plasma requires a transverse local plasma density minimum. This structure can be created a number of ways. A gas in a dielectric capillary can be pulsed with an electrical current which ionizes and heats it. To maintain transverse plasma pressure equilibrium, during the discharge, given the cold walls of the capillary, a plasma density profile forms with the on-axis minimum necessary for guiding [55]. In an all optical scheme, a hot column of plasma is generated with an intense laser. This column expands at the ion acoustic speed of the plasma into the un-ionized medium, producing a transient shock wall and density minimum on-axis [11]. In this chapter, we will discuss the formation and manipulation of plasma waveguides using this optical technique. Figure 3.1 illustrates this scheme for the case of a clustered gas jet target irradiated by the line focus of an axicon (Bessel beam heating).

The plasma waveguides used in the experiments of this dissertation are formed by either focusing a 140 ps 1064 nm laser pulse to a line with an axicon or by focusing a 50 fs 810 nm pulse with an f/25 spherical mirror into a clustered gas medium [26,56]. Clusters are formed by throttling cold, high pressure, gas into a

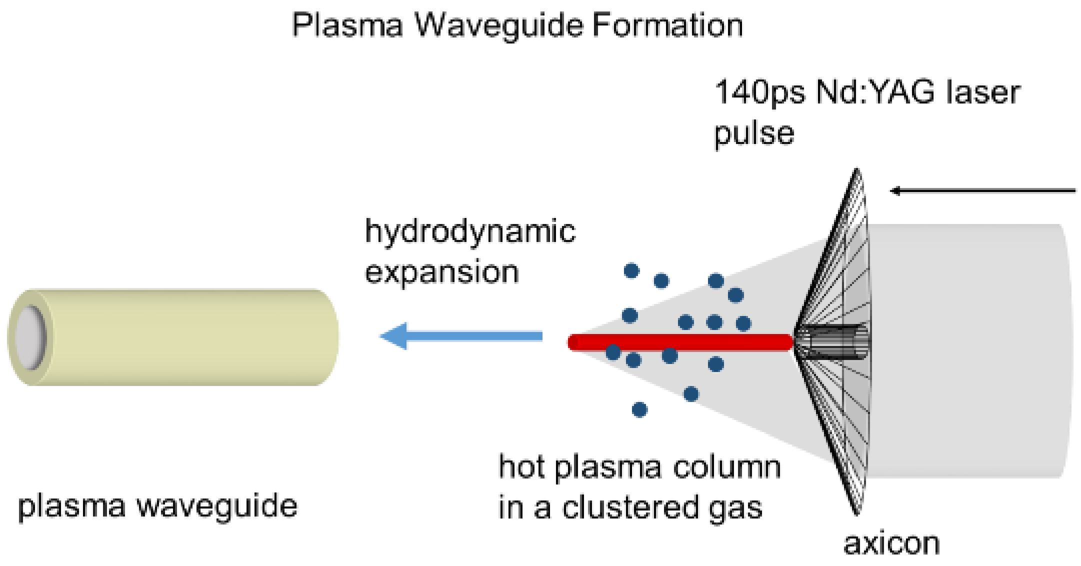

Figure 3.1 An intense Nd:YAG laser pulse is focused to a line in a clustered gas medium. This strikes a hot column of plasma which expands, dynamically forming a guiding structure.

vacuum. The expansion cools the gas further and it precipitates into nanometer-scale solid density aggregates [40]. In practice, this is achieved by pulsing cryogenically cooled gas through a solenoid valve into vacuum.

Clustered gas is an efficient absorber of intense laser light. It is capable of producing the initial electron population and then subsequent heating and deeper ionization over the duration of a single 100 ps or ultrashort pulse [57]. This efficient absorption occurs because the average density of the clustered target is low enough to allow penetration of an intense laser, but the ionized clusters exhibit a local heating akin to a laser-solid interaction. Because of this, nitrogen clusters have been shown to produce uniformly ionized N^{5+} plasma waveguides with 140 ps laser pulses [16].

This chapter describes the formation and structuring of modulated plasma waveguides for electron acceleration schemes such as quasi-phase matched direct laser acceleration (QPM-DLA) and quasi-phase matched laser wakefield acceleration (QPM-LWFA) both developed in our group. Axially modulated plasma waveguides are created either by corrugating the cluster jet flow and applying uniform axial laser heating, or by applying axially modulated heating to a uniform cluster flow. First, the creation of the clustered nitrogen target is described along with a technique for creating corrugations in the cluster density. Then, an optical technique is presented for modulating an intense pulse, which is then used to produce programmable waveguide modulations in a uniform cluster jet.

3.2 Wire Modulated Plasma Waveguides

One way to achieve modulations is to corrugate the flow of the clustered gas target [26]. This can be done using thin wires. When a wire obstructs viscous gas flow, it launches a disturbance in the form of a shock. In contrast, when a wire obstructs ballistic cluster flow, no shocks form and a “shadow” is cast in the flow. Operating within the well-clustered regime is therefore necessary to create high contrast modulations in a plasma waveguide.

To test this, a 25μm tungsten wire was strung over a gas jet. The resulting ‘sliced’ target was irradiated with a 200mJ 35fs 810nm pulse, focused with an f/25 spherical mirror to ionize it. The resulting plasma structure was probed transversely with a λ=400nm probe pulse. The phase shift on the probe was measured using a folded wavefront interferometer and extracted using a Fourier transform technique [58].

Keeping the molecular output of the jet fixed, and varying the reservoir temperature and pressure, the transition from a gas dominated fluid medium to a cluster dominated ballistic medium is observed in the generated disturbance. This was

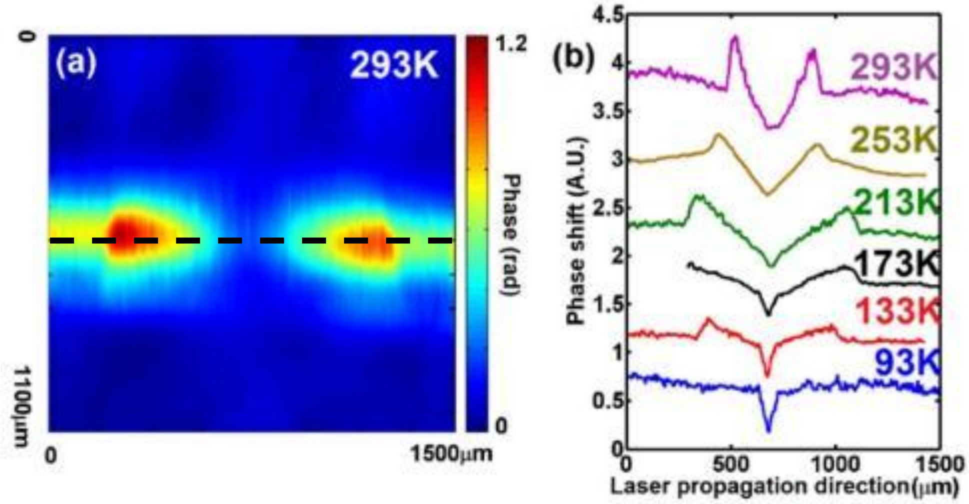

Figure 3.2 Phase shift measurements 1.1 mm above a 25μm wire obstruction. (a) shows plasma generated by irradiating the target above the wire with an intense 810 nm pulse. (b) shows lineouts indicated at the dashed line in (a) for several temperatures, keeping the total molecular output of the jet constant.

accomplished by maintaining the valve backing pressure at 300 psi for temperatures in the range 293 K to 173 K, and 350 psi for 133 K to 93 K. Figure 3.2 shows this transition. The cluster flow regime is indicated by the sharp notch in the density directly above the wire (lower curves), while the gas flow regime is indicated by a wider depression outside of which are sharp density peaks characteristic of an expanding shock wave (upper curves). At 293K, the phase shift is almost completely indicative of gaseous flow, whereas by 93K, the flow of clusters is almost completely ballistic.

Fine density features are necessary for QPMDLA and QPMLWFA. To inspect the limits on feature size, two 25 μm tungsten wires were strung above the elongated cluster target. One wire was fixed while the other was attached to an actuator, which adjusted the spacing between the wires. In the ballistic flow (clustered) regime, the wires were brought together from 170 μm to 65 μm in order to determine a minimum

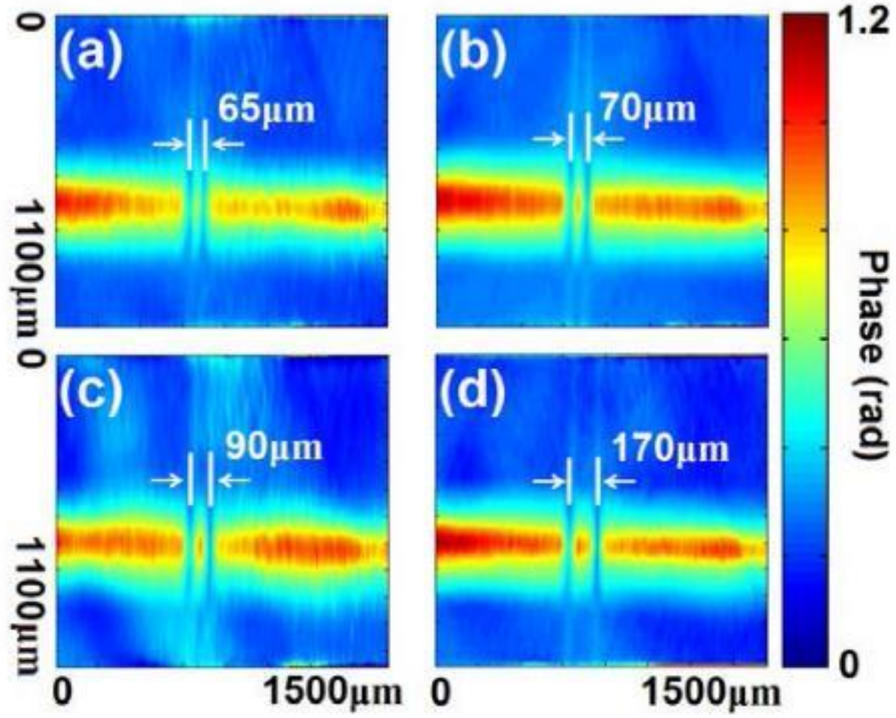

Figure 3.3 With jet parameters fixed in the ballistic regime, a pair of 25 μm wires are brought together. The peak density in the region between appears unaffected by the wires in panels (b), (c), and (d). At about 65 μm separation in panel (a), the penumbras of the wires begin to overlap, reducing the density.

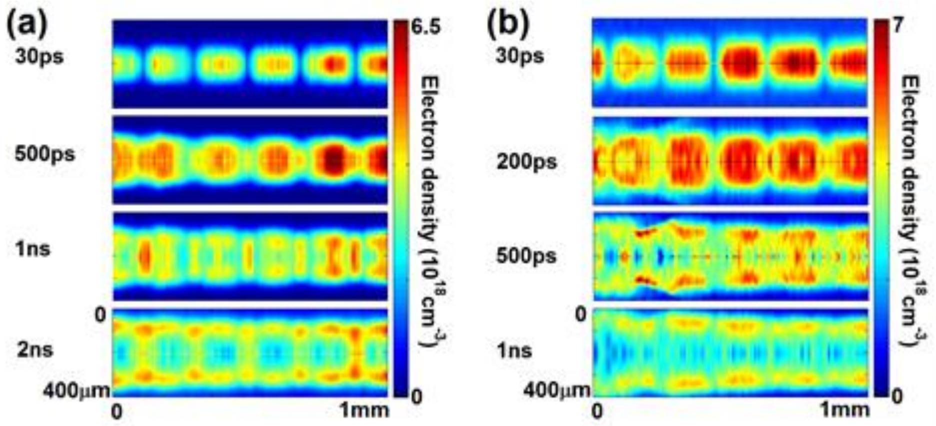

Figure 3.4 25 μm wires were strung in an array with a 200 μm period. The waveguide evolution was probed as above and the plasma densities were extracted via Abel inversion. (a) shows the evolution of a modulated waveguide formed with 93K nitrogen backed at 250 psi. (b) shows the same evolution for a mixture of 90% hydrogen and 10% argon at 300 psi.

possible density feature size of ~70 μm - at which point the flow "shadows" of the wires begin to overlap, reducing the density between them.

To demonstrate the effectiveness of this method, an array of wires was strung over the jet at 93K, producing a series of modulations. The resulting target was irradiated with a 200mJ 35fs 810nm laser pulse, producing several periods of a modulated plasma waveguide. These results are shown in figure 3.4.

The waveguides produced with this method have the benefit of high-contrast and stable modulations. However, the resulting structural modulations cannot be changed without creating a new wire array. Such a design has industrial applications, where the parameters are well known and unchanging, but less desirable in a scientific environment, where more flexibility is desired.

3.3 An interferometric Patterning Method Using a Spatial Light Modulator

3.3.1 Concept

An all-optical method for imposing programmable axial density variations in plasma waveguides is presented. Axially modulated heater pulses have previously been demonstrated using a fixed transmissive ‘ring grating’ [12]. The ring grating method and the method described in section 3.2 produce deep modulations at periods down to 65 μm but are limited to fixed modulation structures. Since both the optimum modulation period and depth for quasi-phasematching depend on many experimental parameters [16,57], it is desirable to have a method to tune them *in situ*.

Here, we achieve heater modulations using a 2D spatial light modulator (SLM), which is an electro-optic liquid crystal array with a pixel-by-pixel-controllable linear birefringence. It is used to impose a transverse *phase modulation* on a low energy laser pulse (<15 mJ) that is interfered with a higher energy pulse (130 – 450 mJ) producing radial intensity modulations. The radially modulated beam is then focused with an axicon to generate a line focus with an axially modulated intensity. The concept is shown schematically in figure 3.5. In prior work by another group [59], a 1D SLM and polarizer directly imposed *intensity modulations* on a high power pulse which was then focused by a cylindrical lens, leading to axially-modulated heating of a plasma channel. However, this method required sending over 100 mJ through the SLM and operating dangerously close to the liquid crystal damage threshold.

3.3.2 Amplitude Modulation through Phase Modulation

The use of interferometric beam combining for patterning the high intensity pulse imposes a trade-off between efficient use of the laser energy and the achievable modulation depth. In order to investigate the relationship between modulation depth and efficiency, we write the field corresponding to the high energy beam as $\mathbf{E}_1$ and that for the low energy beam as $\mathbf{E}_2 = \varepsilon \mathbf{E}_1 e^{i\Delta\varphi(\mathbf{r}_\perp)}$. Here, ε describes the field amplitude splitting at the variable beamsplitter and $\Delta\varphi(\mathbf{r}_\perp)$ describes the transverse phase shift profile imposed on the beam by the SLM. Interference occurs at a non-polarizing beamsplitter of transmissivity *T*.

The total field after combining at the beamsplitter is,

$$\mathbf{E} = \sqrt{T}\mathbf{E}_1 + \sqrt{1-T}e^{i\pi}\mathbf{E}_2 = \left(\sqrt{T} + \varepsilon\sqrt{1-T}e^{i(\Delta\varphi+\pi)}\right)\mathbf{E}_1 \tag{3.1}$$

leading to an intensity profile,

$$I \propto |\mathbf{E}|^2 = \left(T - 2\varepsilon\sqrt{T(1-T)}\cos\left(\Delta\varphi\left(\mathbf{r}_\perp\right)\right) + \varepsilon^2(1-T)\right)|\mathbf{E}_1|^2 \tag{3.2}$$

From equation 2, we can ascertain a maximum possible modulation depth of,

$$\Delta I / I_1 = 4\varepsilon\sqrt{T(1-T)} \tag{3.3}$$

and maximum possible power throughput,

$$P_{max} / P_1 = T + \varepsilon\sqrt{T(1-T)} + \varepsilon^2(1-T) \tag{3.4}$$

where P_1 is the power in the high power arm.

The achievable modulation depth and efficiency both have global maxima with respect to the combining beamsplitter transmissivity, *T*. As seen from eq. 4, the maximum combined power occurs for $T_{P,max} = 1/(\varepsilon^2+1)$, with the associated modulation depth $(\Delta I/I_1)_{P,max} = 4\varepsilon^2/(\varepsilon+1)$ and perfect efficiency $P_{max}/P_1 = 1+\varepsilon^2$. In contrast, eq. 3 shows the maximum modulation depth, $(\Delta I/I_1)_{max} = 2\varepsilon$ occurs for $T = 0.5$ with $P_{max}/P_1 = ½(1+\varepsilon)^2$. The advantage of our interferometric approach is that while the intensity modulation depth scales as ε, the power on the SLM can stay at a safe level, scaling as ε^2. This enables extensive control of modulation depth while maintaining high laser power on target and low power at the SLM.

3.3.3 Experimental Setup

The apparatus, illustrated in figure 3.5, uses a 1064 nm, 140 ps long Nd:YAG laser pulse, which is split into high and low power pulses. The low power pulse reflects off the SLM (Hamamatsu LCOS-SLM, nematic liquid crystal on silicon), picking up a phase shift which is programmed into its refractive index. The low and high energy pulses are then recombined at a non-polarizing beamsplitter (T=0.75) and imaged through an axicon to the line focus, generating an axially modulated plasma waveguide. A synchronous probe pulse passes through the plasma and is imaged into a folded wavefront interferometer to produce interferograms or shadowgrams. The interferograms are processed as described above to extract the phase shift on the probe [60]. Resulting phase shift images are then low pass filtered to reduce noise and Abel inverted to extract the 2D (axial and radial) electron density profile.

Experimental Setup

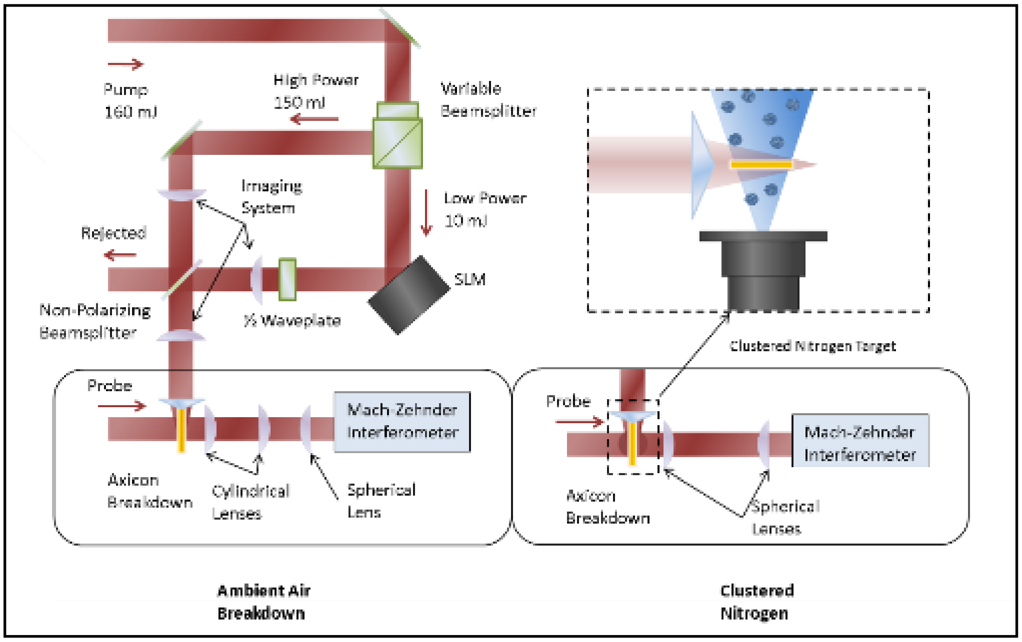

Figure 3.5 Experimental setup. A variable polarizing beamsplitter divides the input pump pulse into high power and low power pulses. The low power pulse is patterned with a phase shift profile by a 2D reflective SLM, and its polarization is then rotated to match the high power beam. The two arms are combined and interfered at a non-polarizing beamsplitter (T=0.75) to produce transverse intensity modulations on the beam. The face of the SLM is imaged to a 28° base angle axicon. The high power arm is imaged likewise. The axicon focuses the modulated beam to a line causing axially modulated breakdown and heating. The plasma is probed by a synchronous pulse which is imaged into a folded wavefront interferometer.

The transversely modulated pulse is then focused by an axicon to form an axially modulated Bessel beam. The modulated Bessel beam ionizes and heats the medium and the intensity modulations result in an axially modulated plasma. The period of the plasma modulations is determined by the SLM pattern, beam magnification between the SLM and axicon, and the axicon base angle. The linear refractive axicons used in these experiments generate a one-to-one mapping of the beam power in an annulus at radius *r* and thickness *dr* to the power in an axial line element at position *z* and thickness *dz* [61]. This effectively yields a magnification factor of the radial modulations dependent on the axicon base angle given by

$$S = \frac{dz}{dr} = \frac{1}{\tan\gamma} - \tan\alpha \tag{3.5}$$

where $\gamma = \sin^{-1}(n\sin\alpha) - \alpha$ is the approach angle of refracted rays toward the axis, *n* is the axicon refractive index, and α is the axicon base angle. The following experiments utilized an SLM with 20 µm pixels magnified by a factor of 2 onto a fused silica axicon with base angle, yielding a minimum modulation period of the line focus. For experiments in air, an axicon with base angle 35° was used, leading to a minimum modulation period of 145 µm. In vacuum, a 28° base angle produced a minimum modulation period of approximately 260 µm.

3.3.4 Experimental Results

Air breakdown and waveguide evolution using a 35° base angle axicon were probed with a sample of the pump pulse at 2 ns delay for interferometric and shadowgraphic characterization of the resultant plasma. First, 130 mJ and 10 mJ were

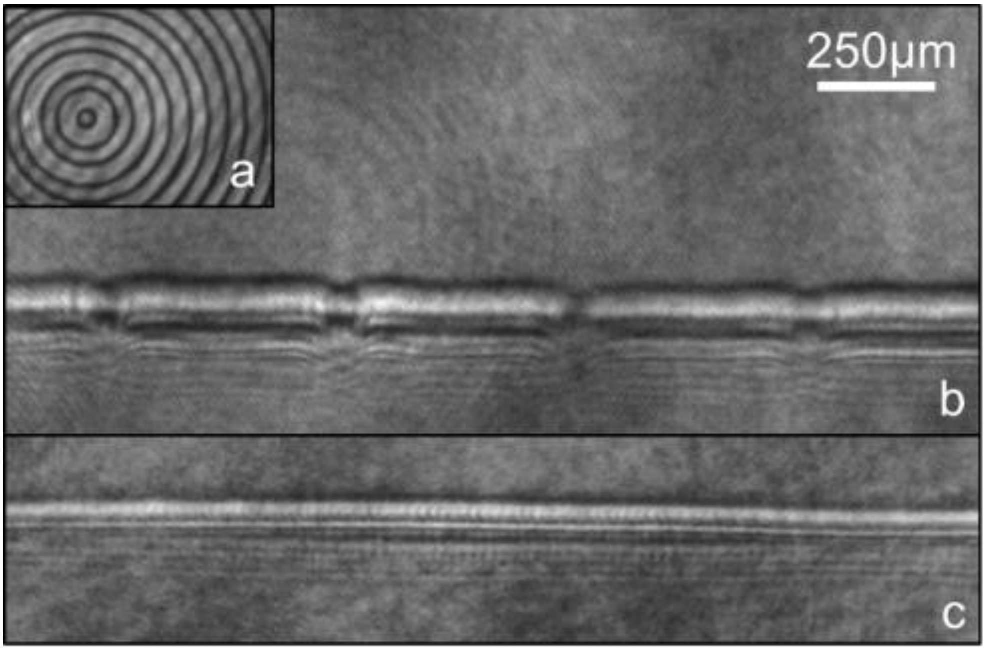

Figure 3.6 (a) Image of a 130 mJ, 140 ps laser pulse with notched minima, and (b) the corresponding plasma with notched un-ionized regions. (c) Without the SLM patterning, the resulting plasma is uniform.

used in the high and low power arms, respectively. In this configuration, the minima of the modulated Bessel beam were below the breakdown threshold of air, allowing modulations to produce un-ionized sections. Figure 3.6 shows shadowgrams for a plasma generated using a phase pattern of equally spaced thin concentric rings imposed on the SLM arm. This leads to a heating profile with concentric thin annular minima, which map to un-ionized regions notched in the plasma with a 400μm modulation period. The nonlinearity of ionization sharpens the notched features below the minimum period supported by the SLM. Such a structure is of interest for guided, quasi-phasematched high harmonic generation [62], with harmonics generated primarily in the notched zones. Without the SLM, the plasma is seen to be uniform.

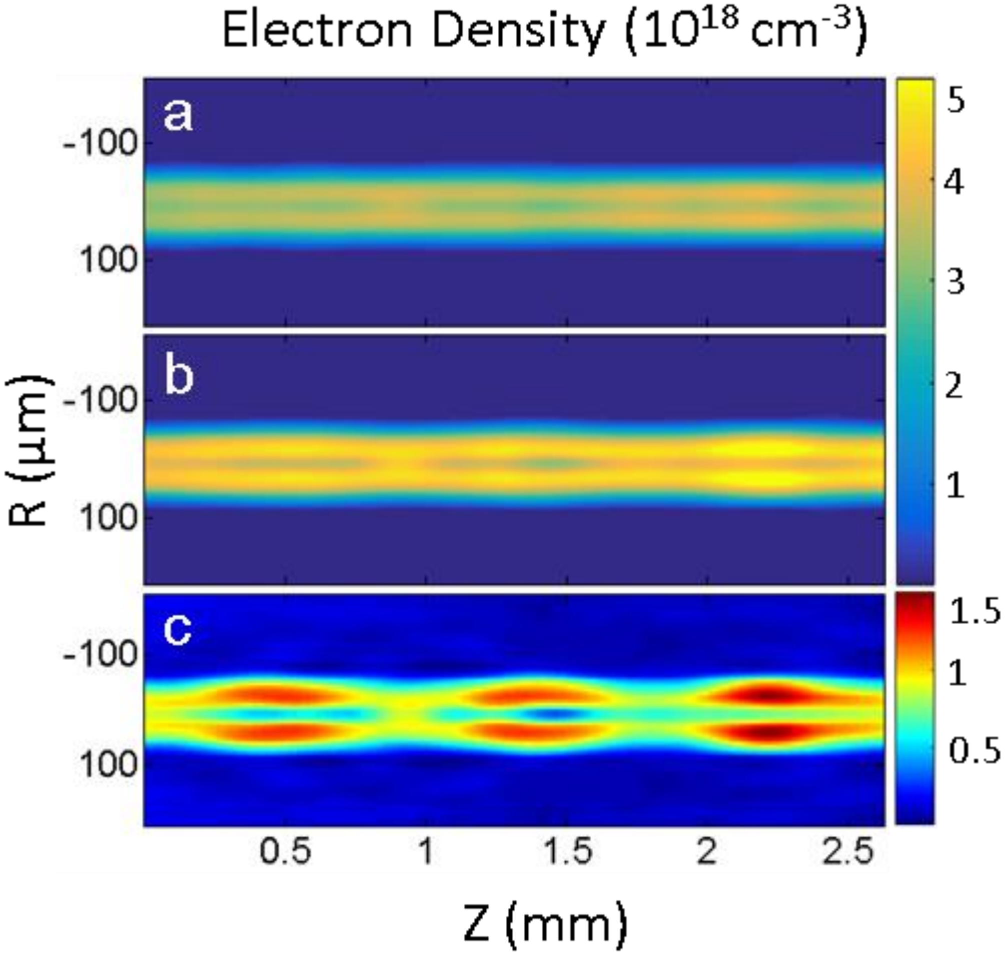

Figure 3.7 Electron density of plasma waveguides in N_2 clusters formed with and without modulations. (a) An unmodulated plasma waveguide formed using only the high power arm. (b) Plasma waveguide with a 860µm period. (c) Difference between modulated and unmodulated densities. Colorbars in 10^{18} cm^{-3}.

Quasi-phasematching of both direct laser acceleration [27] and laser wakefield acceleration [25] would benefit from a modulated plasma waveguide without regions of un-ionized gas. To demonstrate the technique's utility for quasi-phase matched acceleration experiments, the interferometric apparatus was constructed outside of a vacuum chamber, and the radially modulated beam was focused by a 28° axicon over a 7 mm long nitrogen cluster jet. Modulated waveguides were formed in the cluster jet using 450 mJ in the high power arm and 10 mJ in the low power arm. After the combining beamsplitter this gave a maximum modulation depth of approximately 27% on the beam.

Abel inverted images of a 2.5 mm section of the 7 mm long modulated waveguide probed 1ns after breakdown are shown in figure 3.7. Panel (a) shows the channel profile with the SLM arm blocked, yielding a straight channel with no periodic modulations. Panel (b) shows a modulated channel formed by applying a phase mask on the SLM with a 6 pixel radial modulation period. Finally, for clarity the difference between panel (a) and (b) is shown in panel (c) to highlight the periodic modulations imposed by the addition of the modulated beam, showing a clear modulation with an 860 μm period**.** Note that, without interference, after the 75% transmitting beam splitter, the phase modulated arm would only contribute 2.5 mJ of energy while the high power arm would contribute 330 mJ, but the interferometric combination leads to an approximately 10% modulation in the peak density at the waveguide wall.

In summary, the patterning of intense laser pulses using an SLM in an interferometric configuration has been demonstrated. This method reduces the required laser fluence on the SLM, protecting it. These intense patterned pulses can be used to create modulated plasma waveguides in air and nitrogen clusters. Even with ~2% of the total energy on the SLM, the resulting plasma waveguide shows effectively modulated electron density. This technique allows a great deal of freedom for tuning the plasma structures for quasi-phase matching nonlinear optical processes and electron acceleration.

Chapter 4: Self-Guided Laser Wakefield Acceleration and Associated Effects

4.1 Introduction

When relativistic self-focusing overcomes diffraction in a plasma, an intense pulse can collapse to a very intense focus. When Self-focusing collapse stabilizes owing to laser ponderomotive-force induced electron density cavitation, extended self-guiding of the pulse can take place in a relativistic filament. Self-guiding can extend high intensity interactions over many Rayleigh lengths [63]. In this chapter, we examine, with experiments and simulations, the effects of relativistic self-focusing in dense plasmas. First, we identify, for the first time, a new feature universal to relativistic self-focusing in plasma, the spatio-temporal optical vortex (STOV). We study STOVs using 3D PIC simulations [53] of relativistic filamentation. Second, by implementing a thin, dense gas target (see Chapter 2) the interaction of a laser with a near-critical density plasma is investigated. It is seen that these high density targets enable self-focusing, electron injection, and acceleration with very low energy, sub-terawatt pulses.

4.2 Spatio-Temporal Optical Vortices (STOVs) from Relativistic Self-Guiding

In this section, it is shown that energy flow in relativistic filamentation is governed by the formation of spatio-temporal optical vortices (STOVs), just as in air

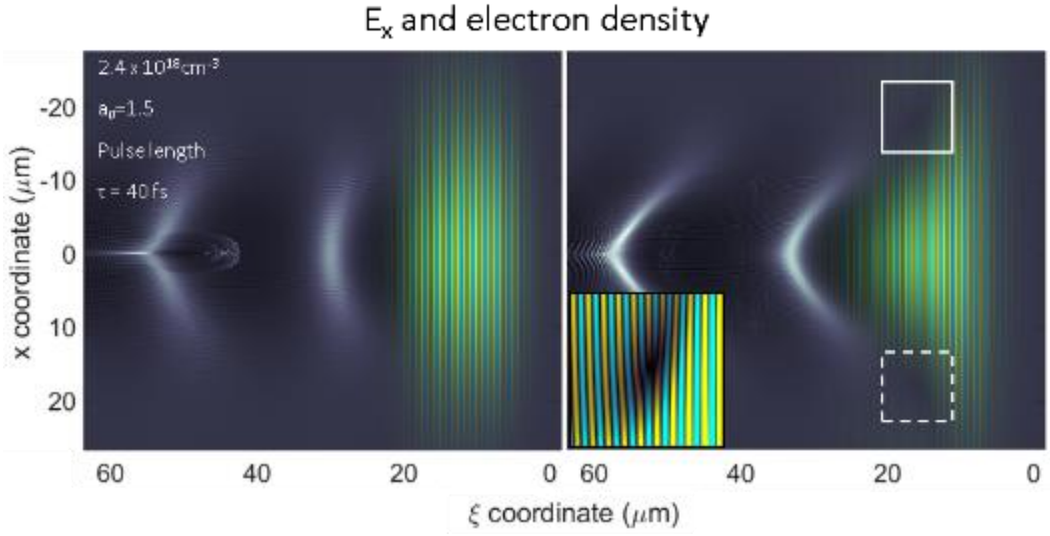

Figure 4.1 2D results of an intense laser field (yellow/cyan) overlaid on electron density (greyscale). The left panel shows the initial pulse profile and plasma wave and the right panel shows the same pulse after 0.5 cm of propagation. The highlighted area is shown in the inset to reveal a phase defect.

filamentation. [64] The complexity of relativistic self-focusing is shown to be simplified by consideration of the nonlinear phase shear of the pulse.

A relativistic filament forms in a plasma when a laser pulse has peak power exceeding the critical power for self-focusing, $P_{cr}[GW] = 17.4(N_{cr} / N_e)$, which is the condition for the self-focusing-induced inward phase front curvature to exceed the outward phase front curvature from diffraction. The self-focusing laser pulse's collapse to a singularity [14] is mitigated by ponderomotive force-induced electron cavitation, which simultaneously generates a large amplitude plasma wake and results in extended propagation of the intense pulse [63].

STOV formation and propagation has been studied previously using a cylindrically symmetric model for femtosecond laser pulse propagation in air [64], where the electromagnetic wave equation is solved using a fluid-like, quasi-neutral (electron charge density=ion charge density at every point) model for the air response. Such a method cannot be applied to the relativistic laser-plasma system because the highly nonlinear and quasi-neutrality-violating plasma response renders the dynamics much too complex. Instead, particle-in-cell (PIC) simulations are implemented, with results showing that STOV formation and propagation is integral to the process of relativistic nonlinear collapse and self-guiding in plasmas.

To show the ubiquity of STOVs in relativistic self-guiding, a 2D PIC simulation of resonant laser wakefield acceleration (LWFA) was performed, simulating the conditions in prior, well-known experiments [22–24]. A λ=800nm, 40 fs FWHM laser pulse with peak normalized vector potential $a_0 = 1.5$ is focused into a semi-infinite plasma of density 2.4×10^{18} cm^{-3}. Examination of Figure 4.1 shows that STOVs can be found on the self-guided pulse. This is seen in boxed region, which is blown-up in the inset, where a dark region indicates an intensity null, and the difference in number of waves above and below the null indicates a phase defect.

The origin of the STOV is the strong gradient in nonlinear phase shift accumulated across the transverse profile of the pulse as it self-focuses. During the pulse collapse, the transverse phase shift gradient can become so strong at a particular location, say $(\xi, \mathbf{r}_\perp) = (\xi_0, \mathbf{r}_{\perp 0})$, that the phase shift variation in the vicinity of this point can reach π. Here, $\xi = \text{v}_g\, t - z$ is the local axial space coordinate in a frame moving with the pulse group velocity v_g along the *z*-axis, and $\mathbf{r}_\perp$ is a transverse coordinate. This gives rise to the birth of a point null in the electromagnetic field envelope at $(\xi_0,\ \mathbf{r}_{\perp 0})$, for which the local phase is undefined (we say the null point has a "phase defect"). In the case of a cylindrically symmetric beam, as modeled in Jhajj *et al* [64], the envelope null would appear as a ring at (ξ_0, r_0), and the phase defect would follow the ring. The null and phase defect at $(\xi_0, \mathbf{r}_{\perp 0})$ subsequently decomposes into two defects—one which slips towards the rear of the pulse and the other which propagates toward the leading edge, shaping the pulse into the characteristic self-guided cone [23]. Although these features have likely been present in many laser plasma systems, their presence in has yet gone unnoticed. A toy model for this process, adapted from Jhajj *et al.*, [64] is presented in Appendix A.2.3.

The phase circulation Γ about these defects satisfies

$$\Gamma / 2\pi = \tfrac{1}{2\pi} \oint_{defect} \nabla\Phi \cdot d\mathbf{l} = \pm 1 \tag{4.1}$$

identifying phase vortices of topological charge +1 and −1, where Φ is the phase of the electromagnetic field component $E = ue^{i\Phi}$, *u* and Φ are real, and the contour integral is taken around the phase defect in the moving frame of the pulse. In the case of a cylindrically symmetric pulse, the field envelope null and phase defect is located at the ring (ξ_0, r_0), and the phase circulation would be poloidal. Because, as seen in figure 4.1 and as explained above, there is phase circulation is in the $(\xi, \mathbf{r}_\perp)$ plane, the associated vortex is *spatio-temporal*, with $\mathbf{r}_\perp$ as the spatial coordinate and ξ as a local time-like coordinate.

In order to study the formation of STOVs and their influence on pulse dynamics, 3D simulations in the resonant regime were run with parameters similar to those of the 2D simulations shown above. The interaction of an 810 nm 40 fs laser pulse with a_0=2 propagating through an underdense plasma was simulated. The transverse laser profile was Gaussian with an 8 micron FWHM at the focus. The focus location was at the interface between vacuum and a semi-infinite uniform plasma with a density 6x10^{18}cm^{-3}. The field solver and particle pusher (discussed in Chapter 2) used a moving window algorithm, with a window speed set at the group velocity of the laser, $\frac{v_g}{c}=\sqrt{1-\frac{\omega^2}{\omega_p^2}}$. Figure 4.2 shows the formation of a STOV in the laser field in the plane of the polarization and propagation directions.

The (ξ, r) 2D air filamentation model of Jhajj *et al.* in [64] assumes cylindrical symmetry, and so STOVs form as ring-shaped phase defects circumscribing a 'core' region of higher laser intensity. Both +1 and -1 charged poloidal vortices are launched in that model, with the +1 vortex eventually settling down to propagate with the self-guided pulse and directing its energy flow (the -1 STOV moves backward and leaves the simulation window). In the 3D simulations of relativistic filamentation, STOVs can grow in a complex manner from a point defect. Eventually, the STOV dynamics settles down so that a +1 ring-like STOV propagates with and circumscribes the core of the self-guided pulse. In fact, the STOV makes possible a rigorous definition of the relativistic filament 'core' as the region transversely interior to the STOV, with the region outside called the 'reservoir' or 'energy bath' [64].

To describe the energy flow in relativistic filamentation, a beam-frame Poynting vector is defined. This can be formed by starting with the stationary frame conservation of energy,

$$\frac{\partial \rho}{\partial t}+\nabla \cdot \mathbf{S}+\mathbf{J} \cdot \mathbf{E}=0 \tag{4.2}$$

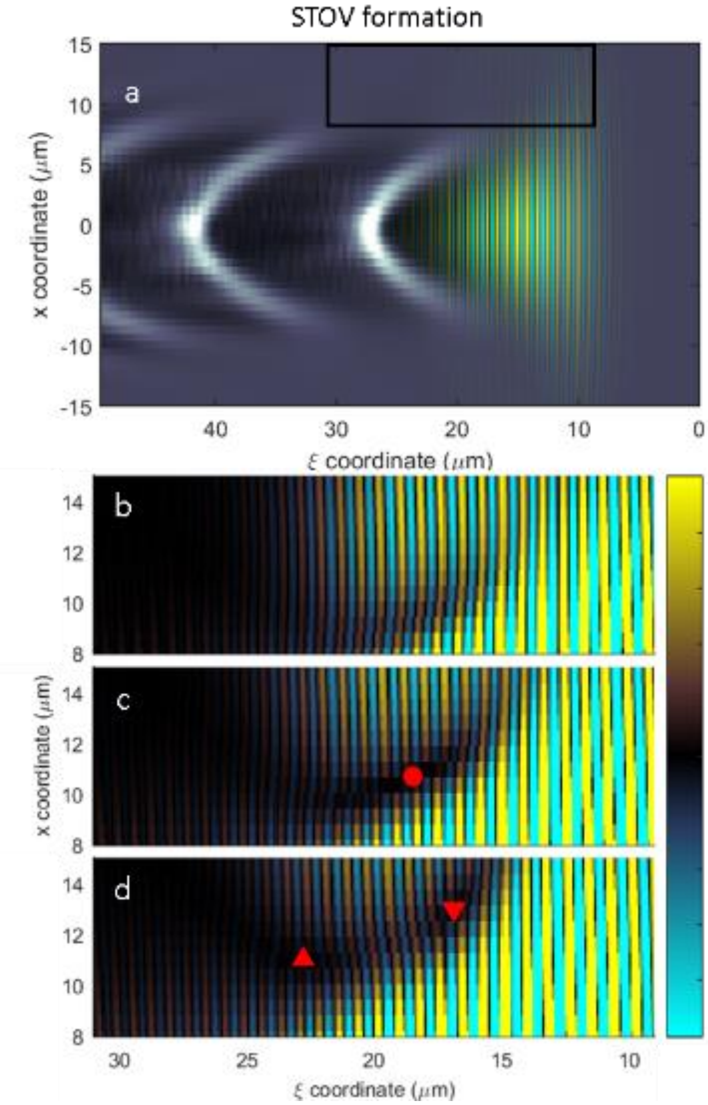

Figure 4.2 3D simulation results showing the formation of a STOV. Panel a shows the pulse profile overlaid on electron density. The boxed region is blown up in panels b-d which are separated by 15 microns of propagation. Panel c shows the formation of a null (red circle) which decomposes into a pair of STOVs, denoted by triangles in panel d. Upward and downward triangles represent STOVs of +1 and -1 topological charge respectively.

where ρ is electromagnetic (EM) energy density, $\mathbf{S} = \frac{c}{4\pi}\mathbf{E}\times\mathbf{B}$ is the Poynting vector (EM intensity), **J** is the current density, and **E** (**B**) are the laser electric (magnetic) fields.

A transformation to the moving frame,

$$\begin{aligned}
&z \rightarrow \xi = v_g t - z \\
&\nabla \rightarrow \nabla' = \frac{\partial}{\partial x}\hat{x} + \frac{\partial}{\partial y}\hat{y} + \frac{\partial}{\partial \xi}\hat{\xi} \\
&S_z \rightarrow S_\xi = v_g \rho - S_z \\
&\mathbf{S} \rightarrow \mathbf{S}' = S_x\hat{x} + S_y\hat{y} + S_\xi\hat{\xi}
\end{aligned} \tag{4.3}$$

yields,

$$\frac{\partial S_z}{\partial z} + \nabla' \cdot \mathbf{S}' + \mathbf{J}\cdot\mathbf{E} = 0 \tag{4.4}$$

which has the form of a conservation law. Thus, in moving frame coordinates, it is the forward-directed Poynting flux S_z that is conserved with respect to the propagation distance z.

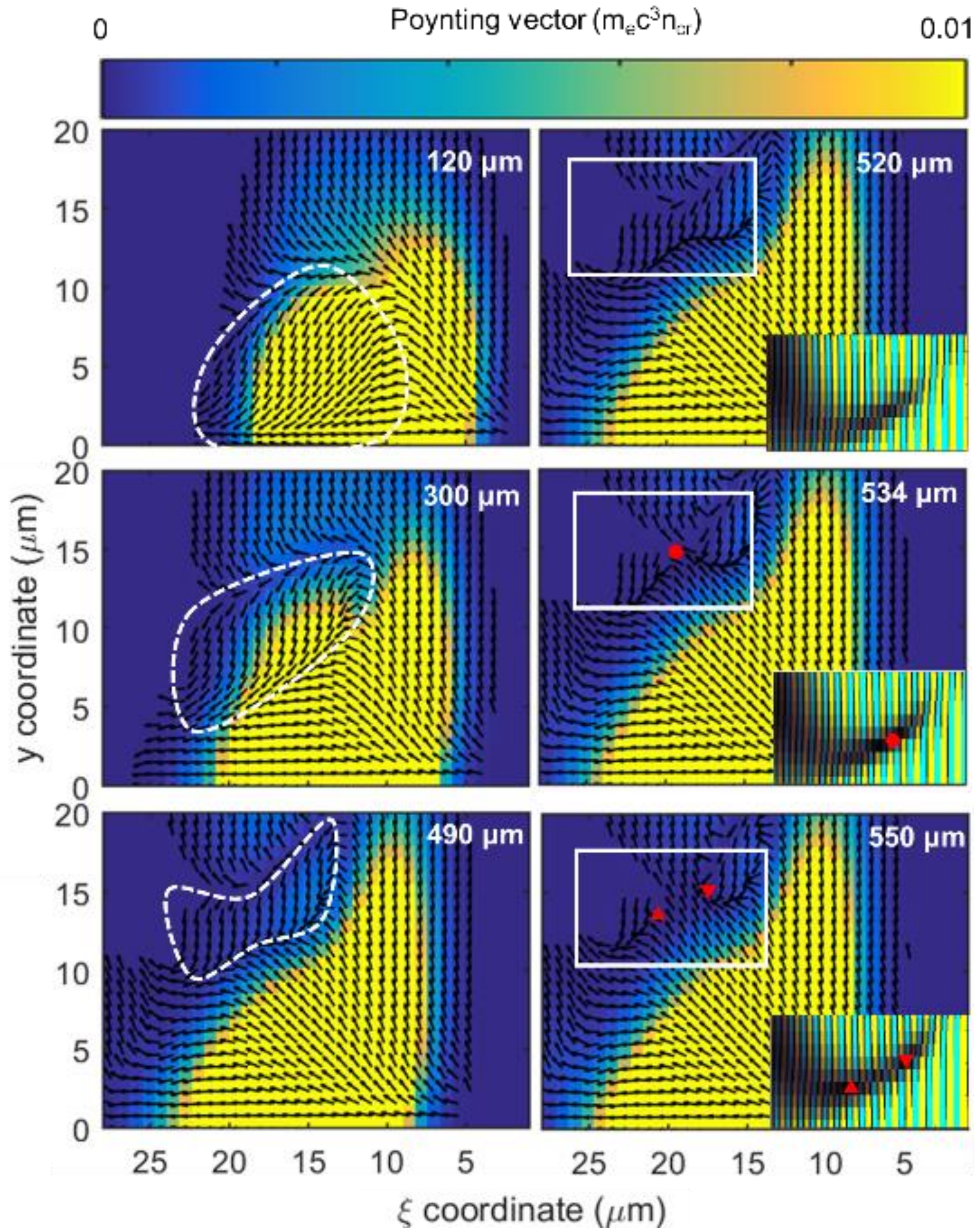

Figure 4.3 $\langle S_z \rangle_t$ *with beam* $\langle \mathbf{S'} \rangle_t$ *direction overlaid in black arrows. A region of axis-directed energy, (indicated with a dashed white line) is seen to form and drift out radially, eventually over the first 520 µm of propagation. This region occludes outward-directed flow which, from z=520-550 µm, pushes through the axis-directed region, creating vortices in* $\langle \mathbf{S'} \rangle_t$*. The formation of these vortices corresponds directly to the formation of STOVs in the laser electric field. At z=534 µm, the penetration of the axis-directed region, along with the formation of a phase defect in the electric field, are indicated by a red circle. At z=550 µm, downward- and upward-facing red triangles indicate both STOVs with topological charge +1 and -1 respectively as well as vortices in the* $\langle \mathbf{S'} \rangle_t$*. Colorbar units are* $m_e c^3 n_{crit}$*.*

Figure 4.3 shows the collapse of a relativistic laser filament looking at the laser envelope in the y-ξ plane with extracted time averaged beam-frame Poynting vector $<\mathbf{S'}>_t$ overlaid (black arrows), where it is seen that STOV formation plays an integral role in the pulse energy flow. Envelope quantities were extracted from the simulated electromagnetic fields using a fast Fourier transform technique (described in Appendix A.1.1), and the time-averaged energy density $<\rho>_t$, Poynting vector $<\mathbf{S}>_t$, and $<\mathbf{S'}>_t$ are calculated from the field envelopes, **E** and **B**, using,

$$\begin{aligned} &< \mathbf{S} >_t = \tfrac{c}{8\pi} \mathrm{Re}(\mathbf{E} \times \mathbf{B}^*) \\ &< \rho >_t = \tfrac{1}{8\pi} (|\mathbf{E}|^2 + |\mathbf{B}|^2) \\ &< \mathbf{S'} >_t = < \mathbf{S} >_t - v_g < \rho >_t \xi \end{aligned} \tag{4.5}$$

It can be seen that STOV formation is closely linked to the dynamics of $<\mathbf{S'}>_t$ during pulse collapse. Initially, with self-focusing dominating, $<\mathbf{S'}>_t$ points towards the center-axis. As the laser energy collects on-axis the electrons cavitate from the increased ponderomotive force, forming a sheath in the periphery of the pulse, and arresting collapse. Without the nonlinear focusing from electrons, the on-axis laser energy diffracts outward, as seen in the outward direction of $<\mathbf{S'}>_t$.

Simultaneously, the laser energy near the sheath is directed inward, occluding the outward diffraction of the on-axis laser energy. As the outward-directed energy escapes *through* the inward directed wall of energy at the sheath, vortices form in $<\mathbf{S'}>_t$. In the insets, the laser E-field shows STOV formation corresponds to the formation of these vortices. This implies that STOV formation not only arises from a local nonlinear phase shear, but is integral to the global pulse collapse dynamics.

Figure 4.4 shows the formation of STOVs in three dimensions. The formation of the long lived ring-like STOV which circumscribes the core region of the laser

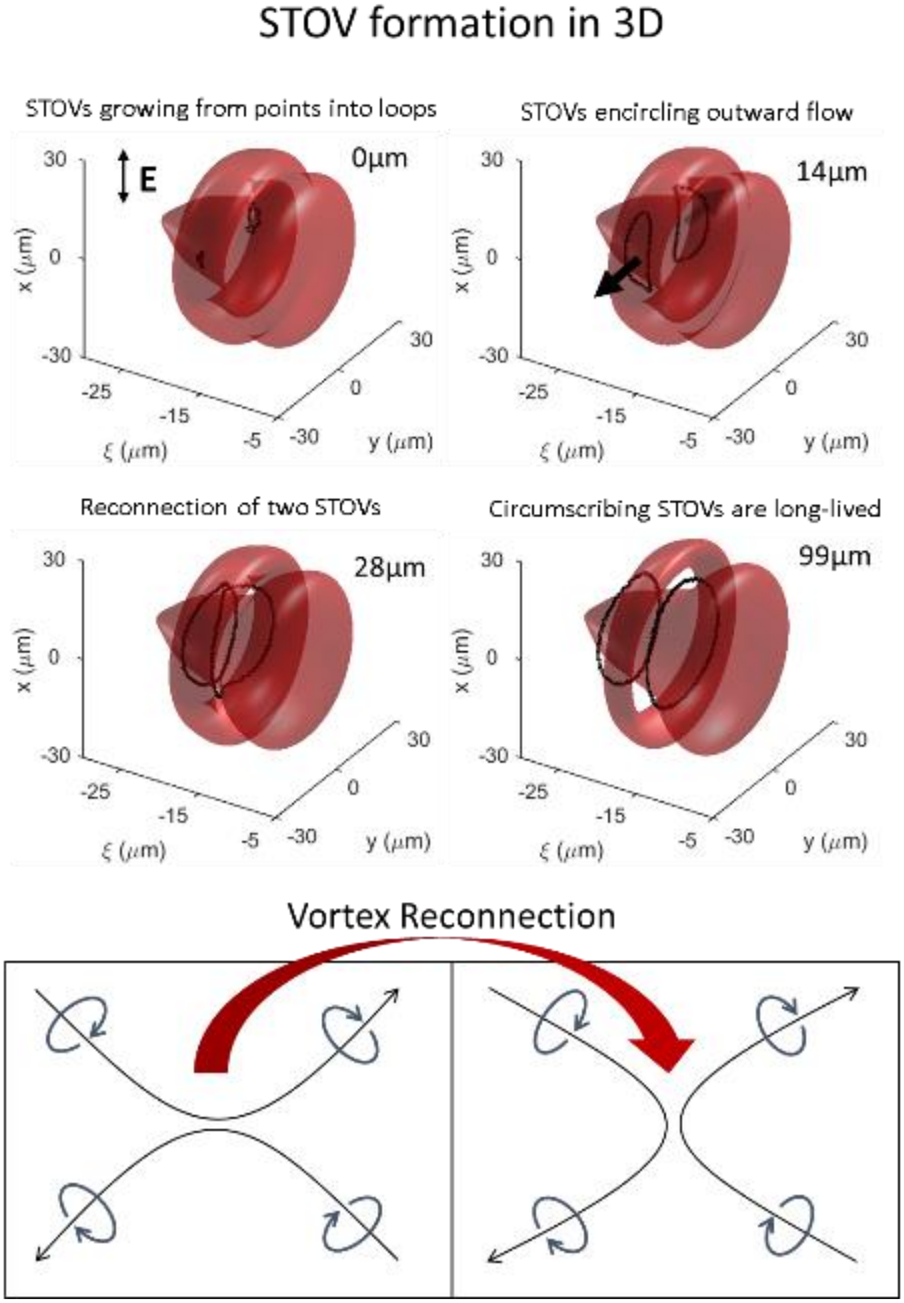

Figure 4.4 Top: STOV formation in 3D PIC simulations shown at four propagation distances. The red surface is the laser pulse envelope (vertically polarized), with black lines indicating STOVs. First, STOVs form from point nulls on the sides of the pulse (declared z=0 μm). These points stretch into closed loops on the sides of the pulse which encircle regions of outward flow (z=14 μm). When the loops touch, they reconnect (z=28 μm), transforming into a pair of long-lived loops which circumscribe the pulse core. Bottom: A diagram of vortex reconnection. When vortices (curved black arrows) touch, they can change their topology via reconnection. This is the process by which STOVs on the side of the pulse transform into STOVs which circumscribe the pulse ~z=28 μm.

begins with nulls in the laser field, located on the sides of the laser pulse. These nulls open into loops which encircle jets of outward Poynting flux. Borrowing the language of superfluid helium vortices, [65,66] two STOVs can be said to “reconnect” with one another, touching at a point and exchanging tails. It can be seen that long-lived circumscribing STOVs are formed through the reconnection of the STOVs on the sides of the pulse.

4.3 Self-Modulated Laser Wakefield Acceleration (SM-LWFA) in a Dense Hydrogen Gas Jet

The power typically required for self-guiding of an ultrashort pulse (~35 fs) in the resonant regime (~10^{18}cm^{-3}) is on the order of 10 TW or higher. However, because of its density dependence, $P_{crit}[GW]=17.4(n_{crit}/n_e)$ [17,18], the critical power for self-focusing can be reduced to below a terawatt for electron densities upwards of $n_e=3\times10^{19}cm^{-3}$ and relativistically self-guiding laser pulses can be studied with modest laser power.

Figure 4.5 shows an experimental setup to demonstrate electron acceleration with a high density target. An intense, 40 fs laser pulse (λ=810 nm) was focused on a thin, dense hydrogen jet to an 8 μm FWHM spot. The pulse is sampled with a pellicle after the interaction to measure its spectrum. The plasma is probed with a λ=400nm, ~50 fs, frequency-doubled portion of the main Ti:Sapphire laser pulse, and imaged to a folded wavefront interferometer to extract target densities. Accelerated electrons

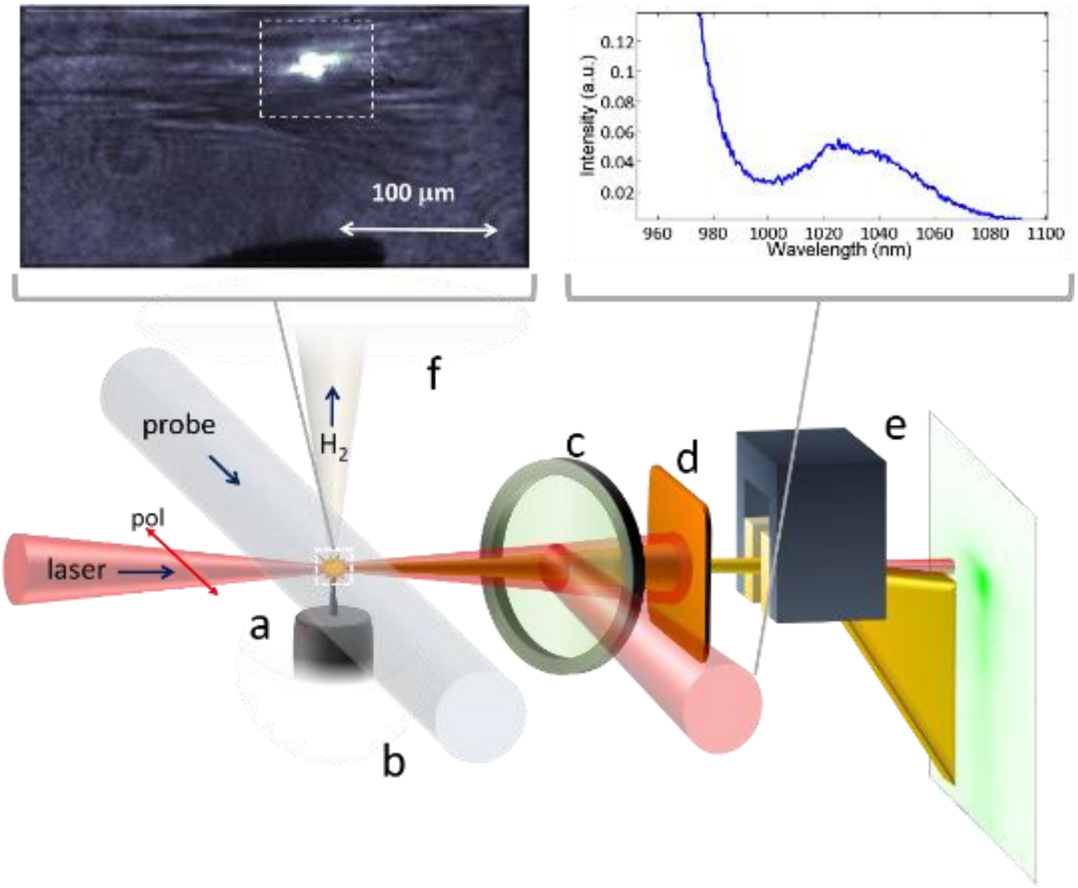

Figure 4.5 Experimental setup. A horizontally polarized Ti:Sapphire laser pulse (10-50 mJ, 50 fs, λ=800 nm) interacts with a cryogenically-cooled, dense thin H2 gas jet (a), whose neutral and plasma density profiles are measured by 400 nm probe by interferometry (b). A portion of the transmitted driver pulse is sampled by a pellicle (c) and measured by a spectrometer. The generated electron beam transmits through the pellicle and enters a permanent magnet charged particle spectrometer. A shadowgram of the laser interaction region above the needle orifice is shown (needle seen as a shadow at bottom), as well as a section of the drive pulse spectrum after the interaction showing a stokes-shifted peak.

transmit through the pellicle and enter a permanent magnet electron spectrometer, described in Chapter 2.

Due to the high density of the target, electrons could be injected and accelerated with sub-terawatt laser pulses. This acceleration was accompanied by a bright flash of light which will be discussed in section 4.3. The electron spectra produced for a variety of pulse energies and target densities are shown in figure 4.6, along with simulations.

At these high densities, ($>10^{19}$cm^{-3}) a 40 fs laser pulse is in the self-modulated regime, meaning the laser pulse length is longer than the plasma period, and breaks into a train of pulselets separated by the plasma period. This was also indicated by the pump spectrum in figure 4.5, showing a strong Stokes peak, indicating modulation. The top panel of figure 4.6 shows this pulselet formation in 3D PIC simulations. The bottom panels show experimental electron spectra in good agreement with the resulting simulated spectra.

It can be seen in figure 4.6 the injected electron bunch (white) overlaps with the driving laser (cyan-yellow). This allows the laser drive betatron oscillations (oscillations within the ion column created by plasma wave), which results in a net forward acceleration when the electrons also interact with the laser magnetic field. The added contribution to the electron energy from the laser can be identified by separating the longitudinal and transverse energy gains.

$$\begin{aligned}
W &= -q\int d\mathbf{r}\cdot\mathbf{E} \approx e\int dxE_x + e\int dzE_z \\
W_{\parallel} &\approx e\int dzE_z = e\int dz(E_{0z}+E_{pz}) \approx e\int dzE_{pz} \\
W_{\perp} &\approx e\int dxE_x = e\int dz(E_{0x}+E_{px}) \approx e\int dxE_{0x}
\end{aligned} \tag{4.6}$$

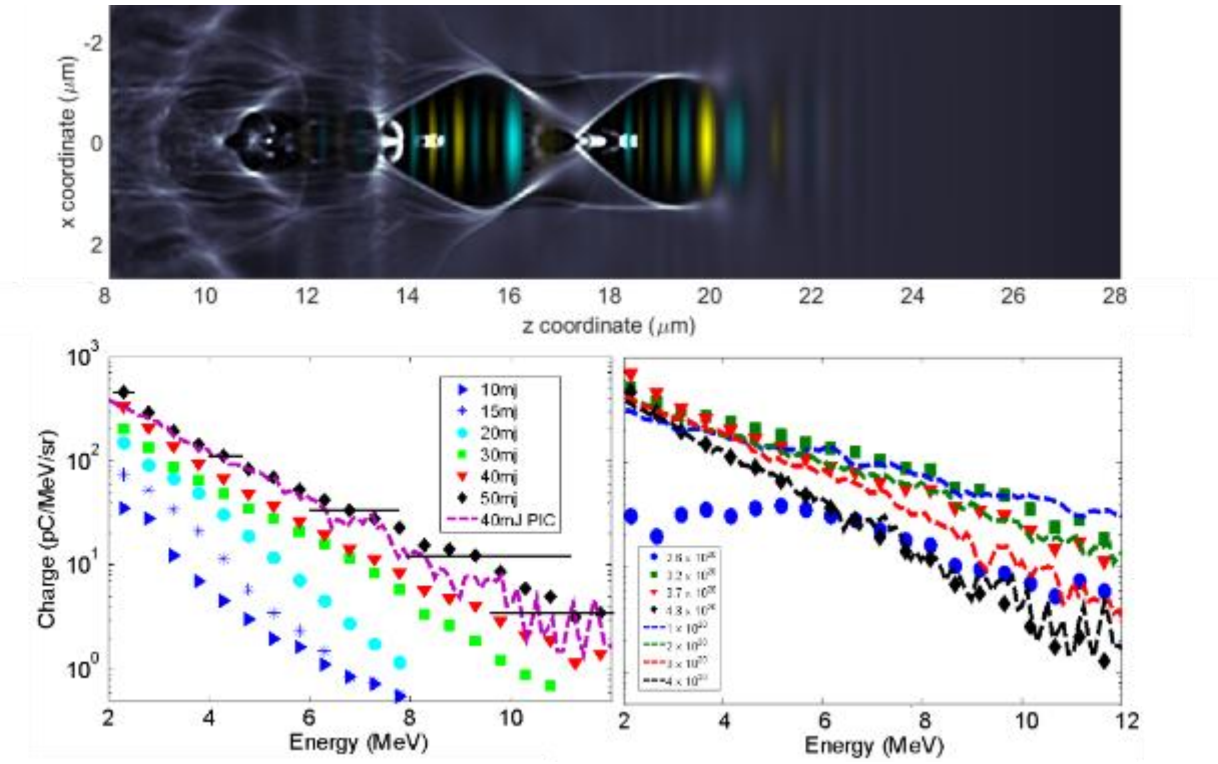

Figure 4.6 (top) laser field overlaid on electron density showing the system in a deeply self-modulated regime. (bottom left) Accelerated electron spectra for peak jet electron density 4.2×10^{20} *cm*$^{-3}$ *for varying laser energy. The horizontal black lines indicate the experimental uncertainty in the energy, determined by geometry-limited spectrometer resolution. The dashed curve is a 3D PIC simulation for 40 mJ pump which has been scaled by a factor 0.14 to line up with the experimental curve for 40 mJ. (bottom right) Accelerated electron spectra at laser energy 40 mJ for varying peak electron density. The dashed curves are from 3D PIC simulations and were scaled by the factor 0.14.*

2D PIC simulations were performed to quantify the relative contributions of direct laser acceleration and laser wakefield acceleration. The TurboWAVE source code was modified to introduce an array quantity Γ_{ij} which represents the total work done on a macroparticle particle *j* over a time *t* by each electric field component *i*, $\Gamma_{ij} = \sum_{\tau=0}^{t} v_{ij}[\tau] E_i[\mathbf{r}_j;\tau]$. This was implemented by updating the quantity during the particle pushing step with the work done on the particle on that step $\Delta\Gamma_{ij}[\tau]$.

$$\begin{aligned} \Gamma_{ij}[\tau+\tfrac{1}{2}] &= \Gamma_{ij}[\tau-\tfrac{1}{2}] + \Delta\Gamma_{ij}[\tau] \\ \Delta\Gamma_{ij}[\tau] &= v_{ij}[\tau] E_i[\mathbf{r}_j;\tau] \end{aligned} \tag{4.7}$$

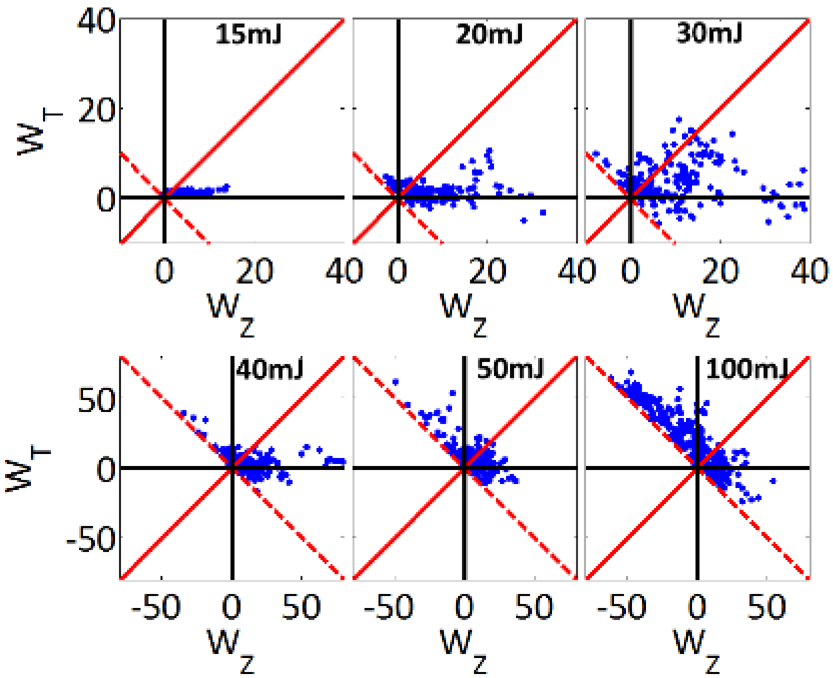

Figure 4.7 2D PIC simulations showing contributions of LWFA and DLA to electron energy gain for a fixed peak plasma density $n_e = 0.07n_{crit}$ for drive laser energies 15-100mJ. Each blue dot is a tracked macroparticle. Regions above and to the left of the solid red line indicate DLA as the dominant form of acceleration, whereas regions below and to the right are dominated by LWFA. The dashed red diagonal marks zero net energy gain. LWFA dominates acceleration at low drive laser energies, transitioning to DLA at high drive laser energies, although the electrons dephase, losing energy to the wake.

The energy contributions can be calculated from Γ_{ij} by multiplying by the time step and particle charge.

$$\begin{aligned} W_{\perp j} &= \Delta t q_j \Gamma_{xj} \\ W_{\| j} &= \Delta t q_j \Gamma_{zj} \end{aligned} \tag{4.8}$$

Figure 4.7 summarizes the relative contributions of direct laser acceleration (DLA) and LWFA. It can be seen that at higher intensities, the DLA contributes more to the electron acceleration and causes early dephasing of the accelerated electrons with the wakefield. Since the electrons are starting from rest, their energy gain must be positive, restricting their position on the W_T –W_Z graph to the upper right-half plain. A dotted line is included to indicate zero net energy gain.

4.4 Broadband Optical Radiation from Electron Injection (Wavebreaking Radiation)

It was seen during the experiment that a bright flash of light on transverse images of the interaction region was correlated with the appearance of electrons on the LANEX screen. Figure 4.8 shows a series of bright flashes over a range of laser energies and target densities. This flash of light was measured to have a ~400 nm full-width spectrum centered at λ~600nm, consistent with a few-femtosecond pulse. Such broadband radiation has previously been seen and identified as wavebreaking radiation [67], though with much lower flux.

The production of this wavebreaking radiation can be modeled by the sudden acceleration of plasma electrons during wavebreaking. As a particle accelerates from rest to the speed of light, it produces a changing magnetic field which in turn produces a unipolar electromagnetic pulse, which is illustrated in figure 4.8. The duration of the resulting pulse is then indicative of the timescale of electron injection into the wakefield. The octave-spanning band is indicates a ~1 fs scale pulse, and therefore acceleration on the order of a femtosecond. This is consistent with acceleration of an electron in a fully cavitated plasma wave, $E = \pi \frac{mc}{e} \omega_{p0} \left(1 + \frac{1}{2} a_0^2\right)^{1/4}$. The acceleration time is estimated by integrating the electron's equation of motion between zero kinetic energy and kinetic energy equal to its rest mass.

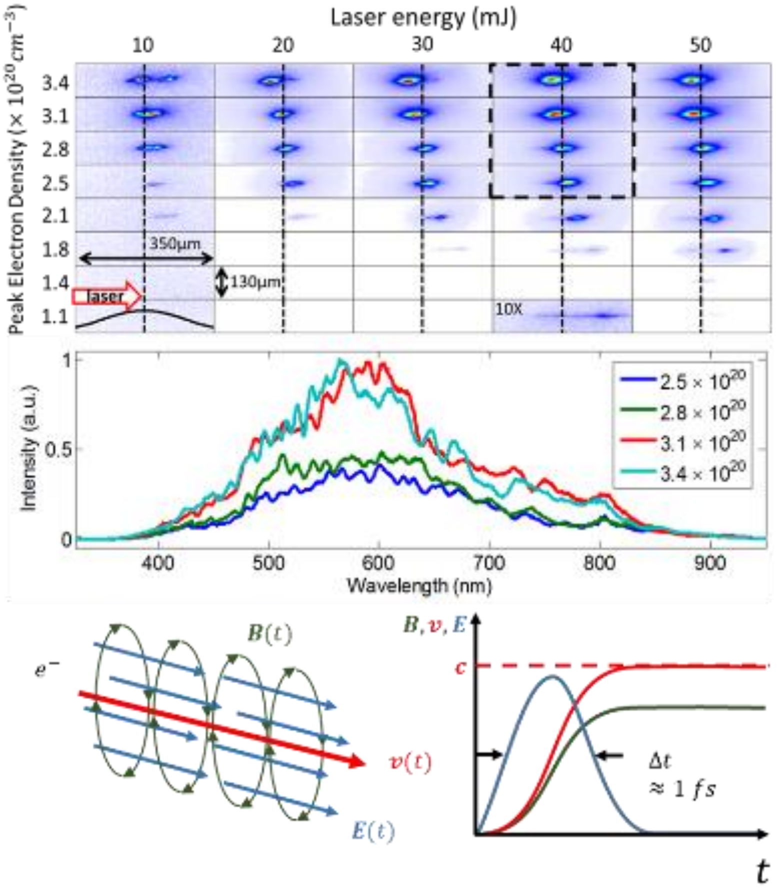

Figure 4.8 (Top panel) Side images of intense radiation flashes from wavebreaking (10 shot averages). The pump laser pulse propagates left to right. Image intensities are normalized to the maximum intensity within each column. The vertical dashed line is the center of the gas jet, whose profile is shown in the lower left. The 40 mJ, 1.1×1020cm–3 image for vertical pump polarization (enhanced 10×), is dominated by 800 nm Thomson scattering on the left and the flash on the right. Center panel: Spectra (10 shot averages) of the flash for conditions enclosed by the dashed black box in the top panel. (Bottom) A simple model showing how a particle accelerated to the speed of light produces a unipolar pulse.

$$\frac{d\mathbf{p}}{dt} = -e\mathbf{E}$$

$$\Delta\mathbf{p}\Big|_{\gamma=1}^{\gamma=2} = -e\mathbf{E}\Delta t\Big|_{t=0}^{t=\tau} \tag{4.5}$$

$$\tau = \frac{\sqrt{3}}{\pi\omega_{p0}}\left(1 + \tfrac{1}{2}a_0^2\right)^{-1/4} \approx 0.5\,fs$$

To explain the anomalous brightness of the broadband flash, one can consider a collection of accelerated electrons emitting. The radiation from these emitters can either add incoherently, in which case the emitted power is proportional to the number, or coherently, in which case the emitted power is proportional to the square of the number of emitters. Since the electrons are all accelerating from a crest in the plasma wave, the criterion for coherent emission can be taken to be the crest thickness Δx_{crest} being smaller than the emitted wavelength λ_{rad}.

This crest thickness can be estimated using a 1D nonlinear model, $\Delta x_{crest} / \lambda_p \sim \frac{1}{\pi}(\omega / \omega_p)^{3/4}(\Delta p_0 / 2mc)^{3/4}$ [68], where Δp_0 is the electron initial momentum spread and λ_p is the quiescent plasma wavelength. For $n_e=3\times10^{20}$ cm^{-3} and $\Delta p_0 / mc \sim 0.06$ (from an initial spread $\sim(\Delta p_0)^2 / 2m$ < 1 keV from residual electron heating after ionization [69]) the crest thickness is $\Delta x_{crest} / \lambda_p \sim 0.04$, or $\Delta x_{crest} \sim 0.12\ \lambda_{rad}$, which is sufficiently small for coherent emission across the visible spectrum. The estimation for the crest thickness also implies that a transition occurs from incoherent to coherent emission as plasma density is increased. This may explain why previous observations [67] of wavebreaking radiation at >10x lower plasma density reported a much dimmer flash.

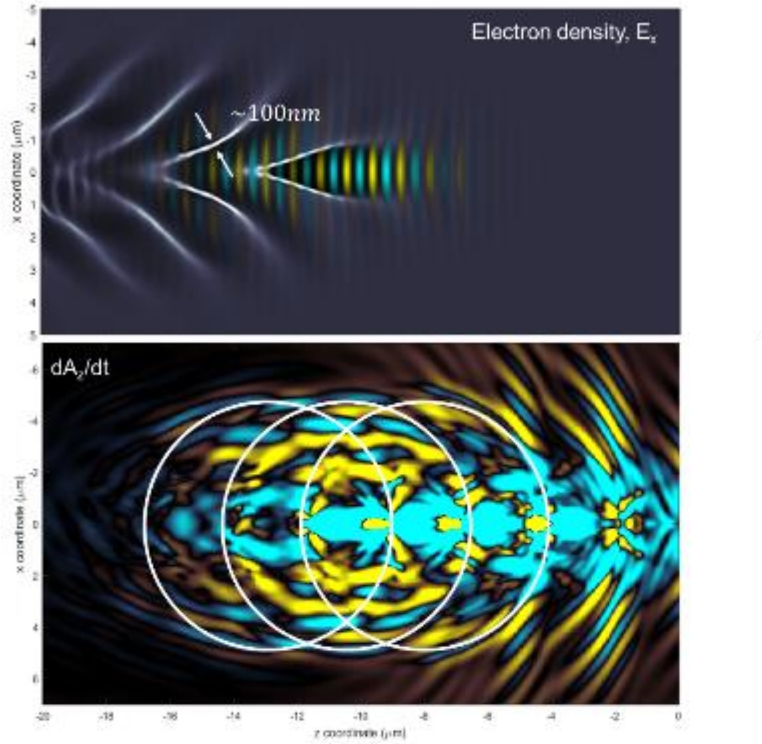

Figure 4.9 PIC simulation results of a 100 mJ laser pulse in a 0.1 n_{crit} plasma. Top panel shows transverse electric field overlaid on greyscale electron density 5 fs before wave breaking. The nonlinear crest thickness is seen to be on the order of 100 nm, consistent with the predictions of the 1D model. The bottom panel shows the generated electromagnetic field 16 fs after wavebreaking. White circles highlight three spherical waves emitted from individual plasma wave crests.

Our 3D PIC simulations confirm this prediction. The top panel of figure 4.9 shows a highly nonlinear plasma wake generated by a 100 mJ pulse in a 0.1 n_{crit} plasma just before wave breaking. The crest thickness is seen to be ~100 nm thick, in good agreement with the 1D model. The longitudinal vector potential in the lower panel shows the propagation of a spherical wave following wavebreaking. Though the central wavelength of the resulting wave is λ~1μm which is longer than the experimental value of λ=600nm, this may be due to chromatic effects in the collection optics which were centered on the visible spectrum.

4.5 Conclusion

In conclusion, we have examined, with experiments and simulations, the effects of relativistic self-focusing in dense plasmas. Using 3D PIC simulations, we have identified, for the first time, the spatio-temporal optical vortex (STOV) in relativistic self-focusing in plasma, and seen that it is integral to the global pulse dynamics. Second, by implementing a thin, dense gas target (see Chapter 2) the interaction of a laser with a near-critical density plasma has been investigated. These high density targets are found to enable self-focusing, electron injection, and acceleration with very low energy, sub-terawatt pulses, in addition to bright broadband electromagnetic radiation from wavebreaking.

Chapter 5: Laser-Driven Proton Acceleration in an Underdense Plasma

5.1 Introduction

The thin, dense gas jet described in Chapter 2 makes accessible the regime of near-critical density plasmas (10^{20}-10^{21} cm^{-3}) needed for magnetic vortex acceleration (MVA) of protons. [37,70] In this chapter, the acceleration of protons to the MeV scale is investigated using 3D PIC simulations with TurboWAVE. [53] First, the application of a high repetition rate, MeV scale, laser-proton source to medical radioisotope production is considered. Then, a process for tuning target parameters for proton acceleration is demonstrated, followed by possible realizations of high repetition rate laser-driven proton accelerator using MVA.

Positron Emission Tomography (PET) is a medical imaging technique that utilizes positron emitters with half-lives on the order of tens to hundreds of minutes. They are produced by proton bombardment in cyclotron facilities, in a concentrated form to compensate for decay during transport to the medical facility. The production of ^{18}F from proton bombardment of ^{18}O water ($^{18}\mathrm{O} + p \rightarrow {}^{18}\mathrm{F} + n$) is favorable due to the relatively long half-life of ^{18}F at 110 minutes, because of reduced decay during transport. A compact proton accelerator would enable the on-site and on-demand production of PET isotopes, and enable more widespread use of alternative isotopes

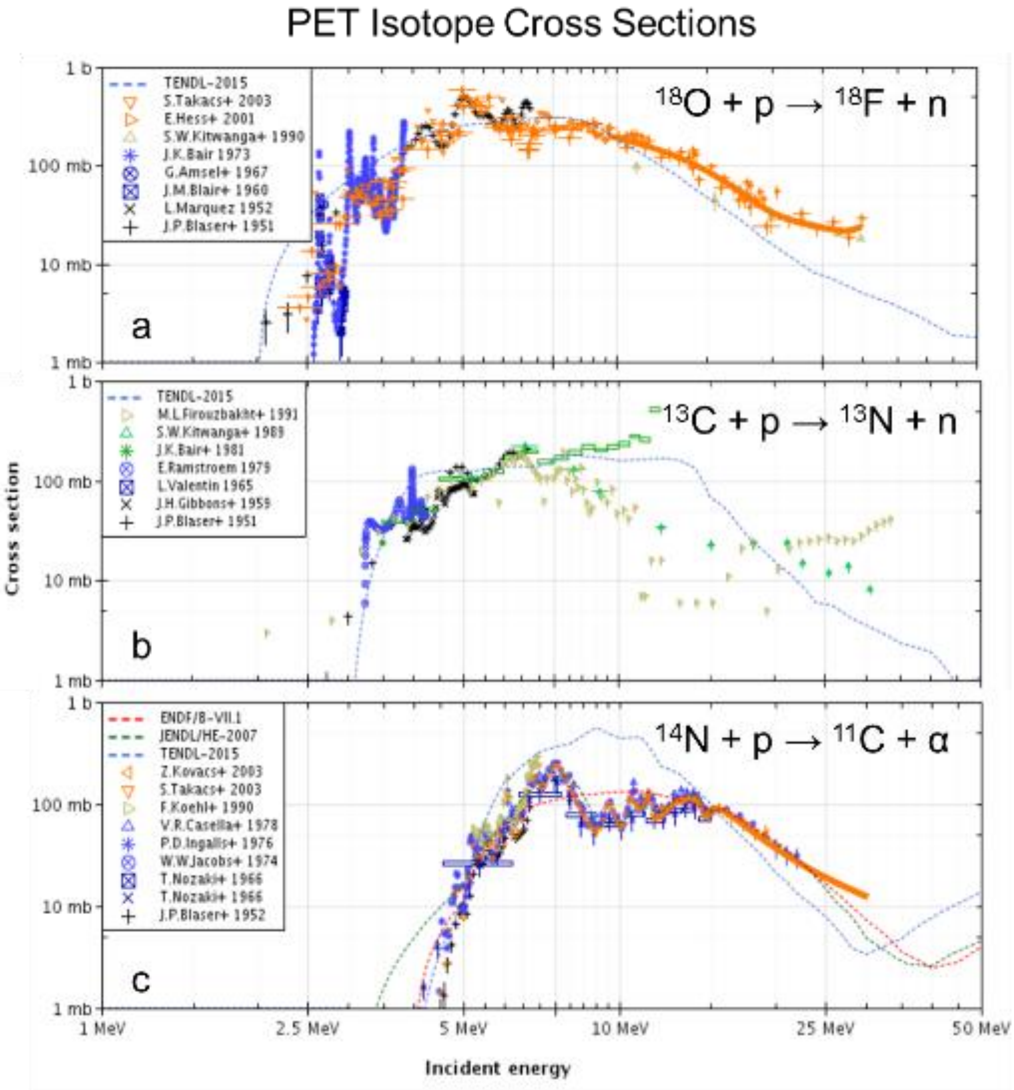

Figure 5.1 Cross sections for the production of a variety of PET isotopes. (a) can be produced with the lowest incident particle energies, and is most commonly used in conventional PET isotope production due to the relatively long half-life of ^{18}F. (b) and (c) would be more useful if produced on-demand, and require lower concentrations due to shorter half-life. (c) also has the added benefit that ^{14}N makes up more than 99% of naturally occurring nitrogen and is therefore quite inexpensive. Taken from NEA databases [71].

with shorter half-lives at lower concentrations. PET using shorter half-life radioisotopes, requires a smaller initial concentration because the higher rate of decay, and thus imposes a smaller total dose on the patient. Production of ^{13}N (^{13}C + p → ^{13}N + n) and ^{11}C (^{14}N + p → ^{11}C + α) is also feasible via proton bombardment. Furthermore, production of ^{11}C from ^{14}N has the added benefit that ^{14}N is extremely abundant, making up over 99% of naturally occurring nitrogen.

Activation cross sections for the production of ^{18}F, ^{13}N, and ^{11}C are shown in figure 5.1. Each reaction has a cross section in the many millibarn range for few to tens of MeV proton energies, and sharp onsets at lower energies of 2.5 MeV, 3 MeV, and 5 MeV for ^{18}F, ^{13}N, and ^{11}C, respectively [71]. For this reason, the focus of this chapter will be the generation of protons at 2-10 MeV energies.

5.2 Achieving Proton Acceleration in 3D simulations

When an intense laser enters a dense plasma, the ponderomotive force causes electron cavitation and generates a beam of electrons which then generates a strong (~10kT) toroidal magnetic field. This changing magnetic field produces an electric field which bores a hole in the electron density which produces an electrostatic field, opening the channel in the protons as well. As the laser deposits its energy into this magnetic field, it depletes, but the magnetic field persists. Without the laser to drive it, the magnetic field undergoes its own dynamics. As described in [70], the magnetic toroid dynamics on a density gradient are dictated by Ertel's theorem, which states that the quantity $\mathbf{\Omega}/n$ is conserved with n the local electron density, $\mathbf{\Omega} = \nabla \times \mathbf{P}$ the generalized vorticity, and electron canonical momentum $\mathbf{P} = \mathbf{p} - e\mathbf{A}$.

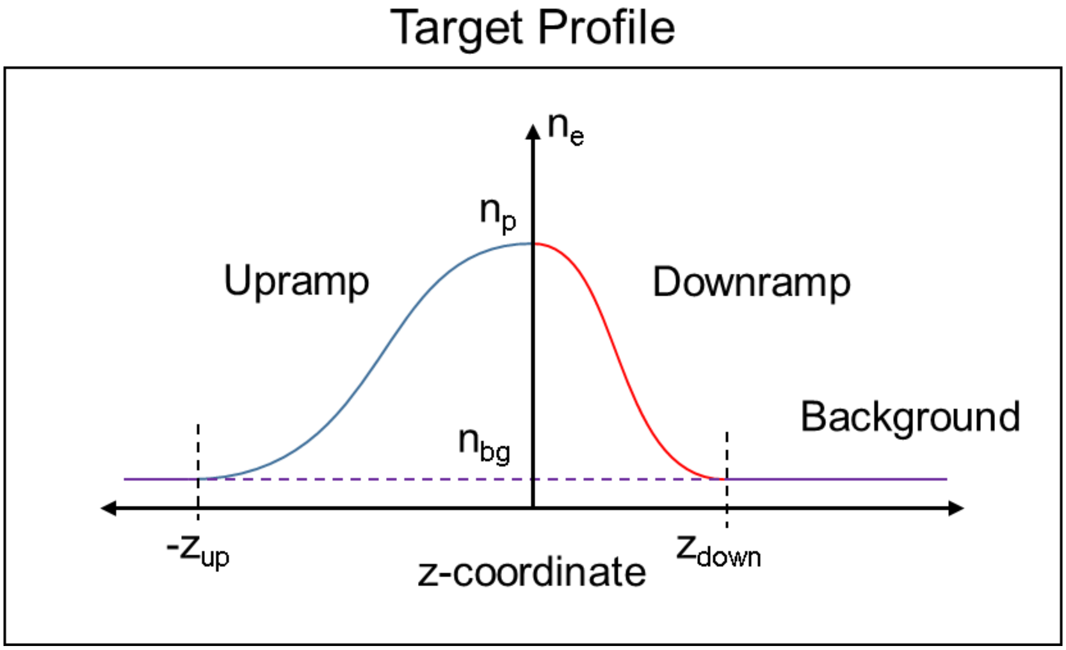

Figure 5.2 The longitudinal target profile is described by four values, Peak density np, background density n_{bg}*, upramp length zup, and downramp length* z_{down}*. These are tuned in three steps to a given laser pulse.*

It has been shown with 2D PIC simulations that the electric fields generated from the expansion of this magnetic field on a plasma density gradient can accelerate protons to 10-150 MeV energies. [37,70] However, experimentally, and in 3D simulations, this mechanism has been seen to be significantly less effective, producing few energetic protons (<1 pC above 1 MeV) from TW laser interactions [72,73]. Recently, 3D simulations of a 34J, 17fs laser pulse interacting with a liquid hydrogen target have been shown to produce GeV-scale protons [74], although no 3D simulations have thus far shown acceleration on the many pC scale above 1MeV from 20 TW laser systems.

To achieve ion acceleration via MVA in a 3D PIC simulation, a near-critical density plasma target was designed in three steps. Figure 5.3 illustrates the

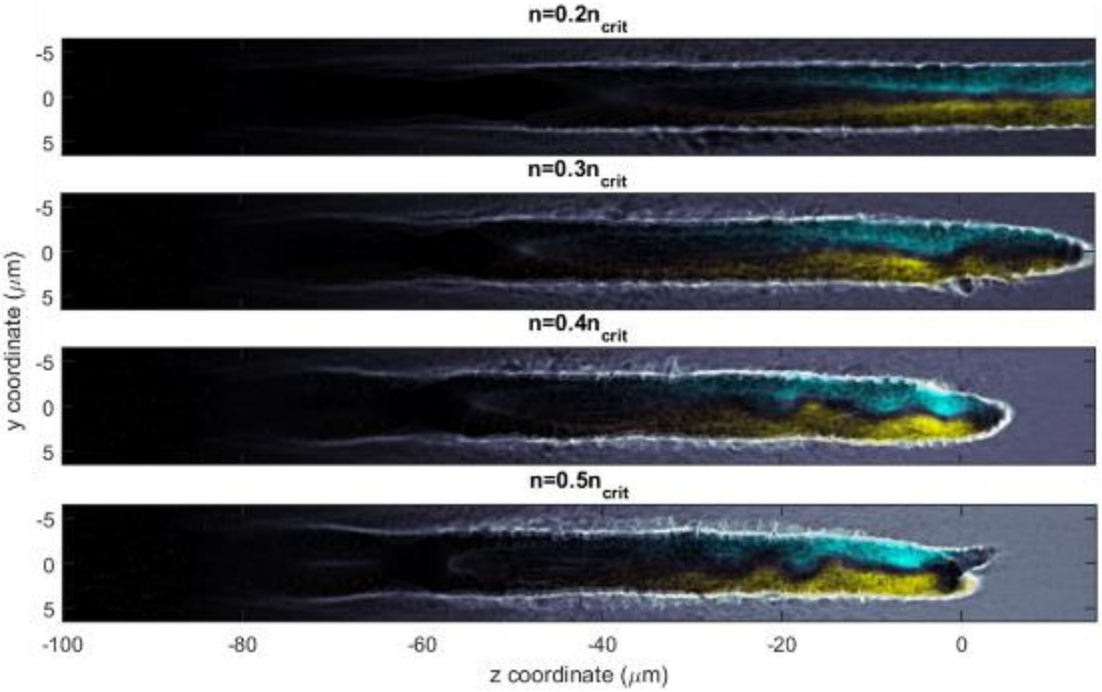

Figure 5.3 For a given pulse energy, the penetration depth into a target can be tuned by the target density. Optimum acceleration conditions should occur at the maximum density which permits transmission of the laser pulse.

longitudinal target profile and the relevant parameters to be tuned. Electromagnetic instabilities can cause deflection and breakup of the laser, limiting its penetration. [75,76] It was seen in [75] that circularly polarized light partially mitigates these instabilities by reducing temperature anisotropy in the plasma. We have also seen that longer pulses exhibit less transverse instability than shorter pulses for a given pulse energy. A 110 fs circularly polarized laser pulse with wavelength 810 nm and 3.25 TW of power was used to design this target because it was seen to show stable propagation in the 0.2-0.5xn_{crit} density plasmas. The vacuum focus position is set half-way up the target up-ramp, with a spot size of 5.4 μm FWHM.

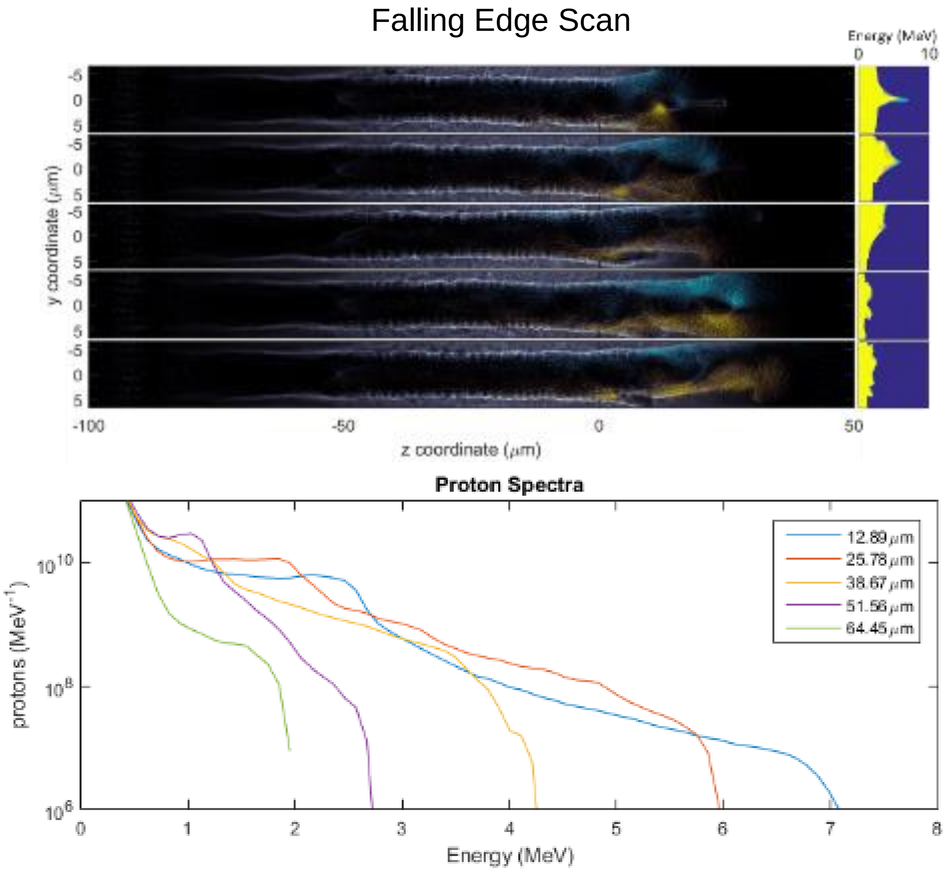

Figure 5.4 The exit density ramp is steepened, revealing that an exceptionally steep (25 um) drop in density is required for acceleration of protons >5MeV. At shorter lengths, the total proton yield begins to drop.

The peak profile density n_p was varied. For this step the length scale z_{up} was chosen to be 100 μm, similar to those experimentally demonstrated in [8]. As seen in figure 5.3 the peak density of this stage was varied from 0.2 - 0.5n_{crit} and for densities above 0.3n_{crit}, the laser was seen to deplete before boring to the peak density at z=0.

Next, the peak density was fixed at 0.3n_{crit} from the previous step, and the length of the downramp was varied. Figure 5.4 shows that, although a downramp of 12μm produces a higher maximum energy, a downramp of 25 μm produces about 50% more protons in the energy range suitable for PET isotope production (>4 MeV).

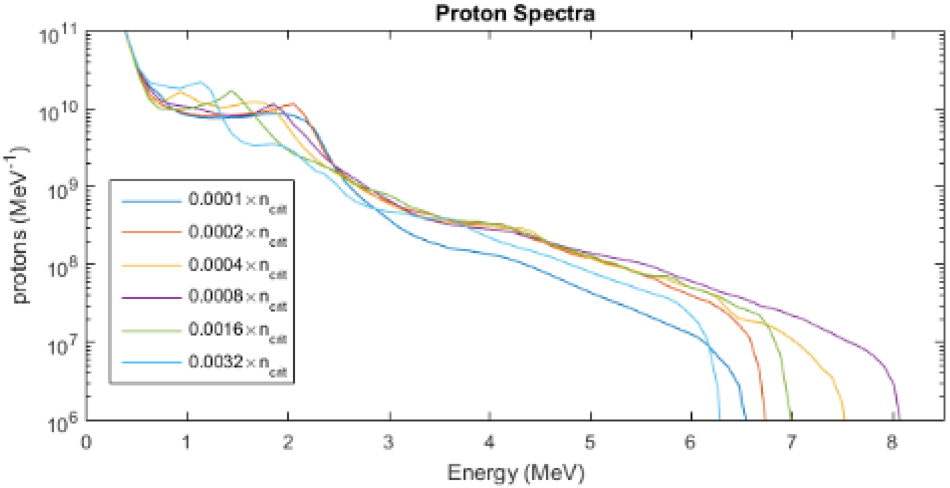

Figure 5.5 Spectra produced by varying background plasma density. There is a clear optimum with a maximum energy and maximum proton yield with respect to background density. At very low densities, densities, the spectrum approaches the best spectrum in figure 3.4, whereas at high densities, the background suppresses magnetic vortex expansion, impeding acceleration.

Finally, a background plasma was introduced to supply more protons for acceleration. Using the profile from the previous step with a 25 μm downramp, the background density was varied. Figure 5.5 shows the resulting proton spectra. At high background densities, the magnetic field expansion is impeded by the background plasma at the downramp, and at low densities, the results approach those obtained in the downramp-varying step. At the optimum background density, 0.0008 n_{crit}, $1.2x10^9$ protons with energy above 4MeV are produced.

5.3 MVA with a 20 TW Ti:Sapphire Laser

In this section, the target parameters resulting from Section 5.2 are adjusted to meet experimental constraints of the thin dense target and Ti:Sapphire laser system described in Chapter 2. In Section 5.2, it was seen that production of 4MeV protons required a downramp as small as 25 μm, which is smaller than those measured in the existing targets. Instead, a symmetric 50 μm FWHM density profile is used, and the

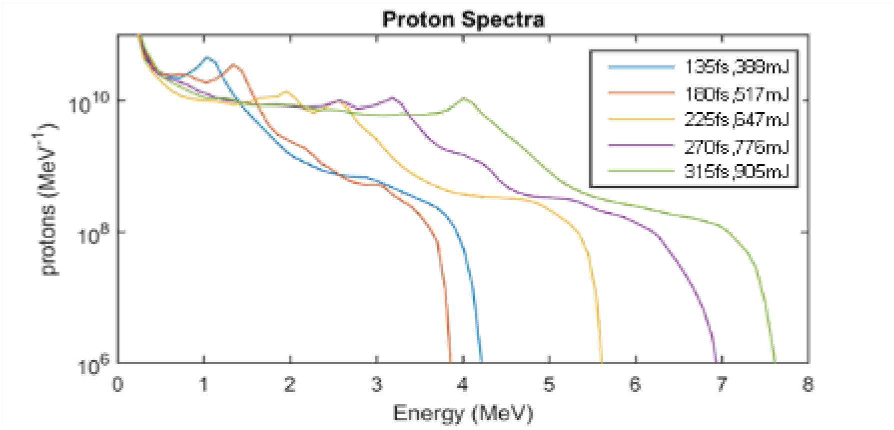

Figure 5.6 Simulations of an 810 nm pulse interacting in a 50micron FWHM plasma profile with a peak density of 0.3xn_{crit}. The resulting spectra show protons in our region of interest (>2.5 MeV) with less than 400 mJ of laser energy.

laser energy is limited to under 1 J. As above, the laser was circularly polarized to reduce the effects of transverse instabilities in the pulse propagation. The vacuum focus intensity was fixed at a_0=3.5, and the laser focused half way up the up ramp.

The target profile is a 5th order polynomial resembling a Gaussian with 50 micron FWHM and a peak density of 0.3 critical. With the peak laser field fixed at a_0=3.5, the energy of the pulse was increased by increasing the pulse length. Because the intensity is the same across these simulations, much of the dynamics are the same, but the longer pulses have more energy to contribute to the generated magnetic field (and therefore, the protons) before depleting.

Figure 5.6 shows the simulation results and spectra. 5.5 x10^{10} protons above 1MeV with a cutoff energy of 7.5 MeV are produced in the interaction using <1 J of laser energy. It can be seen that about 650 mJ of laser energy in 225 fs is necessary to produce an appreciable proton population above 4MeV.

5.4 High Repetition Rate Disk Laser Systems

Since proton movement is long timescales compared to electron movement, the need for a short pulse may be relaxed, and allowing for picosecond-scale pulses enables the use of high-average power disk lasers to drive the acceleration. Such lasers are commercially available with 200 mJ 1-picosecond pulses at a kilohertz repetition rate [77]. Advances have been made pushing few-ps pulses to the Joule level, maintaining 100 Hz repetition rates [78,79]. Additionally, advances have been made reducing pulse lengths to 185 fs with 0.5mJ of pulse energy at 20kHz [80]. It will be shown here that existing disk-laser technology is on the verge of application to proton acceleration and that, with modest enhancement of pulse energy or reduction of pulse length, they would be ideal drivers for high repetition rate laser-driven proton sources.

Currently, commercial disk lasers are available at kHz repetition rates with 1 ps pulses up to 200 mJ of energy [77]. We will first consider the scenario in which kHz, 1ps disk lasers can produce energies in the range of 1J and find the necessary target parameters which will enable the acceleration of protons. Then, we will consider the possibility that a kHz 200 mJ laser can be compressed to ~100 fs pulse lengths, and again find the target parameters necessary for proton acceleration.

First, considering the case of a joule-class 1ps laser system, we take the pulse length to be fixed, and vary the pulse energy from 0.7 – 6.7 J. In these simulations a 63 micron FWHM longitudinal plasma profile was used. As in Section 5.3, we want to keep the self-guided field strength fixed at a_0=3.5 and vary the pulse energy, but since the pulse length is fixed at 1ps, the vacuum spot size was varied instead. The

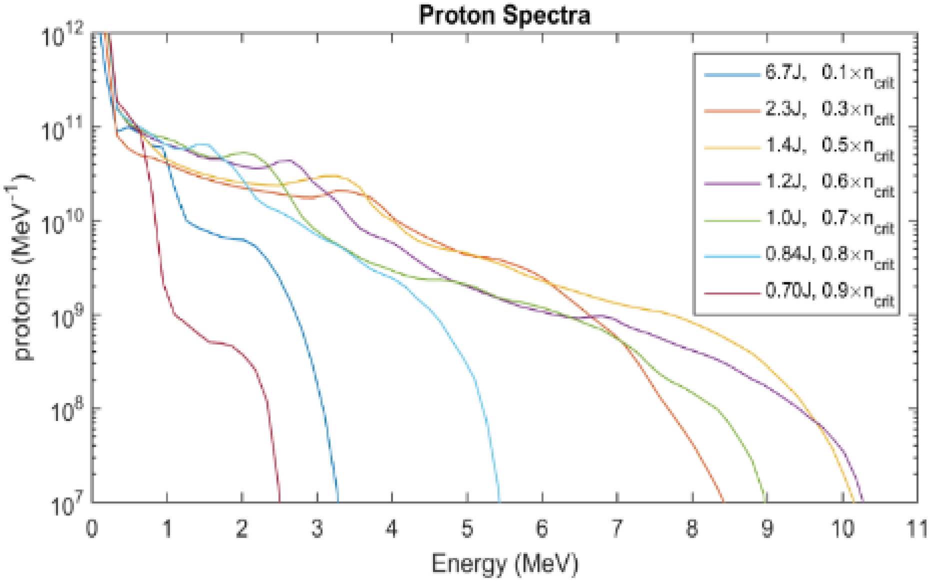

Figure 5.7 Proton spectra for a variety of plasma densities and pulse energies, holding the pulse length fixed at 1 picosecond, and the peak intensity fixed with a_0*=3.5. Cutoff energies are seen above 10 MeV with little over one joule of laser energy.*

target density was adjusted for each energy such that the spot size scaled with the plasma wavelength and thus the self-guided spot size. [81] For example, if the spot size was doubled, the density was reduced by a factor of 4.

Figure 5.7 summarizes the results. At high energies (and therefore, low densities), the generated magnetic field (which scales linearly with plasma density) is reduce, yielding a smaller cutoff energy, while at low laser energies (higher densities), the laser depletes before it drives the magnetic field on the downramp of the plasma. These competing effects lead to an optimum energy and density of ~1.4J and $0.5xn_{crit}$ respectively.

Finally, considering efforts to create sub-picosecond pulses using disk lasers. [80] Regenerative amplifiers have been developed showing that Yb:KYW disk laser pulses can be compressed to less than 200 fs [80]. We will consider in simulations the compression of an existing 200mJ commercial disk laser. Here, laser

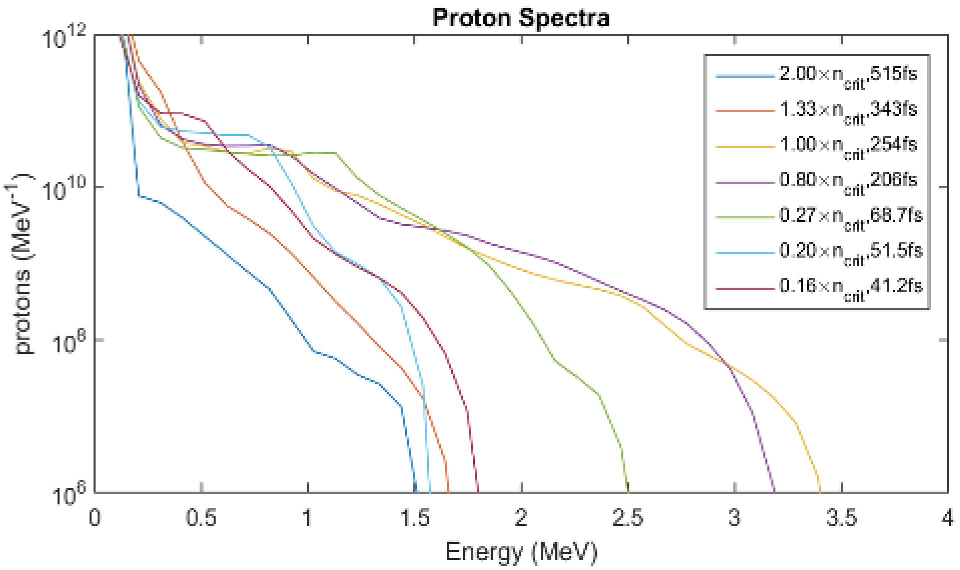

Figure 5.8 Proton spectra resulting from 200 mJ pulses of various pulse lengths irradiating a variety of plasma densities. The highest cutoff energy is seen at critical density with a 200 fs pulse. At high densities, the laser does not fully penetrate the plasma and at low densities and at short pulse lengths, the magnetic fields are too transient to efficiently couple energy to the protons.

energy is fixed at 200 mJ, and the plasma density is adjusted. Since we would again like to hold a_0=3.5, and because the self-guided spot size scales linearly with the plasma wavelength, the pulse length is adjusted in proportion to the square of the plasma wavelength.

Because the energy in the pulse was about 25% of the optimum in the energy scan in figure 5.7, the target thickness was reduced to 13 microns FWHM. Figure 5.8 outlines the resulting proton spectra, showing an optimum near critical density with a 200 fs pulse. The best results show cutoff energies of over 3 MeV with 3 x 10^8 protons above 2.5 MeV, the lower limit for effective generation of ^{18}F from ^{18}O.

5.5 Conclusion

In conclusion, 3D simulations of proton acceleration of 5.5 x 10^{10} protons above 1MeV demonstrated, with less than 1J of laser energy, accessible to the Ti:Sapphire system described in Chapter 2, with a thin-dense target about half the thickness of the thin-dense hydrogen target, also described in Chapter 2. Hypothetical laser systems representing likely advances in disk laser technology are seen to generate 1.4 x 10^{10} protons above 4 MeV with cutoff energies above 10MeV using 1.2J of energy in a 1ps pulse. 10^{10} protons above 1MeV with cutoff energies above 3MeV were demonstrated with 200mJ of energy in a 200ps pulse. Such developments in disk lasers will enable high repetition rate compact proton sources for PET isotope production for a variety of medical applications.

Chapter 6: Conclusion and Future Work

6.1 Particle Acceleration in Three Regimes

Three regimes of laser-plasma-based charged particle acceleration have been discussed. In the first regime, laser propagation is linear or weakly nonlinear, and if there is no preformed guiding structure, the interaction will be limited to a Rayleigh length of propagation. A guiding structure can be produced using the transient expansion of a plasma formed at the line focus of an axicon.

The second regime is dominated by relativistic self-guiding and wakefield generation. With laser power above P_{cr}, of the surrounding plasma, self-focusing effects overcome diffraction and the laser collapses and propagates as an intense filament. In this regime, large amplitude, nonlinear plasma waves are driven which can inject electrons into the accelerating phase of the wakefield.

Finally, in the third regime, cavitation and electron injection generate a quasi-static magnetic field which co-propagates with the laser through the plasma. In this regime, ions can be moved by prolonged charge separation, forming channels or being accelerated as a beam.

6.2 Electron Acceleration Assisted by a Guiding Structure

Acceleration in the first regime requires a relativistic electron bunch to be injected along with the drive laser in a preformed plasma waveguide. Two acceleration methods were introduced involving the use of axial density modulations in the plasma waveguide to overcome dephasing. In the quasi phase-matched direct laser acceleration (QPM-DLA) method, a longitudinal component of the laser is quasi phase-matched to the electron bunch, producing a net forward acceleration. In the quasi phase-matched laser wakefield acceleration method, a linear plasma wave is quasi-phasematched to an electron bunch.

The fabrication of modulated waveguides for these schemes was presented. Two techniques for generating modulated plasma waveguides were demonstrated. One uses thin wires to obstruct clustered gas flow, producing a corrugated neutral target which can then be formed into a modulated waveguide by ionization with a channel forming pulse. The effects of gas reservoir temperature and pressure on the modulation formation were measured and a highly clustered regime with sharp features identified.

The second technique used a spatial light modulator (SLM) to pattern the channel forming pulse. The average and peak pulse power were well above damage threshold of the SLM so an interferometric technique was developed to allow the beam to be patterned. This instead required only putting a small fraction of the total beam power on the SLM. The patterned beam produced axial modulations in the resulting plasma waveguide which were adjustable *in situ* by adjusting the modulations on the SLM.

6.3 Electron Acceleration and Pulse Propagation Dominated by Relativistic Self-Focusing

When the power of a laser is above the critical power of the plasma in which it propagates, a relativistic Kerr nonlinearty causes it to self-focus until higher order nonlinearites balance out the self-focusing. The resulting filament drives a large amplitude plasma wave which self-injects electrons.

It was shown through simulation that in the self-guiding regime, defects form in the phase of the laser pulse. These spatiotemporal optical vortices (STOVs) are seen to be ubiquitous in relativistic self-guiding systems. Simulations of the well-studied resonant regime suggest STOVs have already been present in many experiments and simulations. Their dynamics were seen to be central to the flow of energy during pulse collapse.

Simulations in the self-modulated regime were also performed wherein the laser pulse length is greater than the plasma period. It was shown that with a sufficiently thin and dense hydrogen target, wakefield acceleration in the self-guiding regime can be achieved with less than a terawatt peak-power. This was confirmed experimentally, and was in good agreement with simulations.

The TurboWAVE source code was modified to track work done by transverse and longitudinal components which differentiates between wakefield energy gains and those from ion-channel DLA. It was found that at higher pulse powers, DLA contributes significantly, causing early dephasing of the electrons from the wakefield.

The generation of a bright flash of broadband optical radiation in this regime was also seen. This was identified as wavebreaking radiation and characterized to be octave spanning, coherent visible light. The mechanism was identified as coherent wavebreaking radiation. The sudden acceleration of electrons to near light speeds produces a unipolar electromagnetic pulse. If the plasma crest is sufficiently sub-wavelength, this emission is expected to be coherent. Simulations confirm both the emission of broadband radiation and the crest thickness to be a fraction of the emitted wavelength.

6.4 Ion Acceleration in a Near-Critical Density Hydrogen Gas Jet

At even higher densities and powers, the plasma response is so nonlinear that a quasistatic toroidal magnetic field is generated. This field causes prolonged charge separation, evacuating strongly magnetized electrons and leaving behind unmagnetized protons. This charge separation then induces proton motion, forming a proton channel in the wake of the pulse. The expansion of this magnetic toroid on a density gradient has been proposed [37,70] to produce protons with MeV energies.

Three-dimensional simulations were performed which demonstrated proton acceleration up to 10 MeV. The necessary laser and target parameters were deduced for three plausible scenarios. In the first, a proof-of-principle experiment was simulated, using a joule-class Ti:Sapphire laser producing $5.5\text{x}10^{10}$ protons for <1J of laser energy. Then, a laser pulse consistent with commercial disk lasers was simulated and the optimum pulse energy for proton acceleration found. Finally, keeping pulse energy fixed and compressing it, acceleration to 3MeV was also achieved. These scenarios confirm the efficacy of the acceleration mechanism and provide a future direction for laser based ion acceleration devices.

6.5 Future Work

6.5.1 High-Density Electron Acceleration

Currently, work is being done to characterize the broadband optical radiation emitted during wavebreaking. An experiment is underway to use self-diffraction frequency resolved optical gating (SD-FROG) [82] to measure the spectral phase of the flash. Preliminary measurements of spectral coherence of the flash were made by interfering it with a narrower bandwidth supercontinuum (SC) reference pulse generated in a xenon gas cell. In the top panel of figure 6.1 this flash can be seen to be spectrally coherent over the full reference SC bandwidth. However, because the flash bandwidth exceeds the SC bandwidth, the flash coherence remains to be fully characterized.

The generation of electrons with sub-terawatt pulses has opened up the opportunity to perform electron acceleration with more compact and high repetition rate laser systems. The bottom panels of figure 6.1 show electron spectra and profiles using a kilohertz repetition rate 10 mJ laser system. Efforts are currently being made to further reduce pulse energy using few-cycle optical pulses.

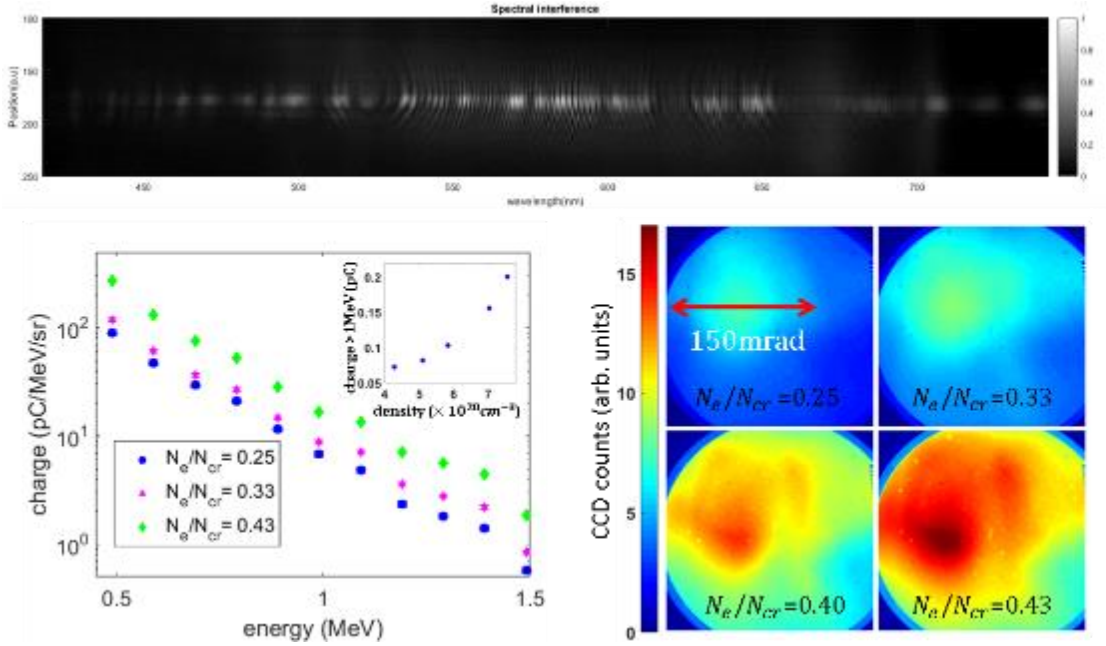

Figure 6.1 (Top) Spectral interferometry of supercontinuum from a xenon gas cell with broadband flash emitted during wavebreaking. Fringes appear over the entire supercontinuum range, but even the supercontinuum does not cover the entire bandwidth of the flash. (Bottom) Electron spectra (left) and electron beam profiles (right) generated using a 10 mJ 1 kHz repetition rate laser system.

6.5.2 Proton Acceleration

An experiment is underway to demonstrate proton acceleration using the Ti:Sapphire system described Chapter 2 in an f/3 focusing geometry. In Chapter 5, the acceleration of protons from a 50μm thick near-critical density plasma with 500mJ – 1J, 230 fs laser pulses was demonstrated in simulations. Using the same thin-dense hydrogen target described in Chapter 2, with razorblades as obstructions, an even thinner, denser structure is achievable which should be sufficient for acceleration. Figure 6.2 shows an interferogram of a razor blade creating a shock over a 150 μm nozzle. The shock appears to have thickness on the order of 50 μm, so the parameters in the simulation described in Section 5.3, which showed protons accelerated above 7 MeV, should be achievable experimentally.

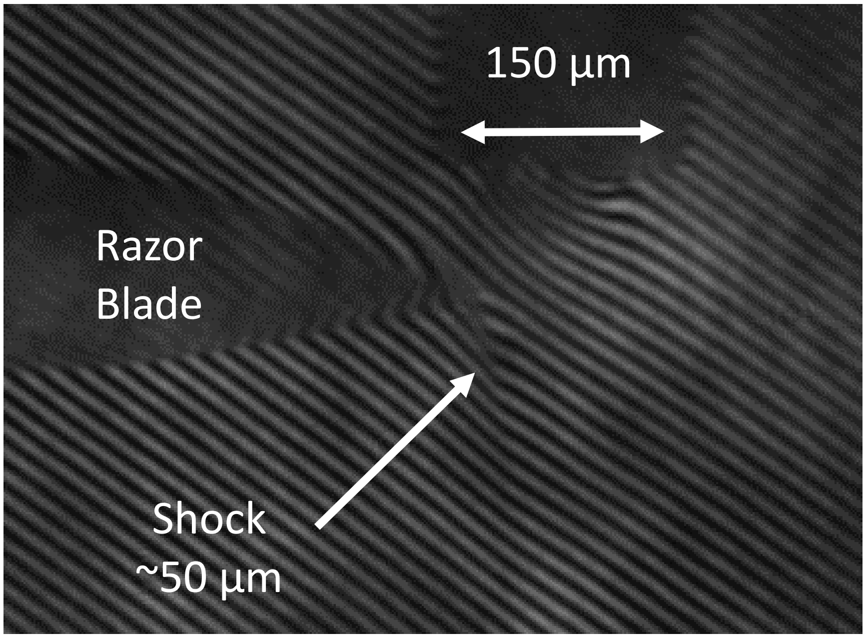

Figure 6.2 A shock formed from a razor blade over the thin-dense hydrogen gas jet. This method offers a way of both generating sharper target gradients, as well as higher target densities.

6.6 Conclusion

At their conception, laser based particle accelerators could boast enormous accelerating gradients compared to conventional accelerators. To push the limits on particle energy, larger lasers have been and are being built. However, there are other important particle beam qualities. System compactness, high bunch charge, average current, and beam quality are all desirable for many particle accelerator applications. The work described here contributed to developing truly compact laser based particle accelerators, which would have broad impact in scientific, industrial and medical applications.

Appendices

Appendix I: Computational Methods

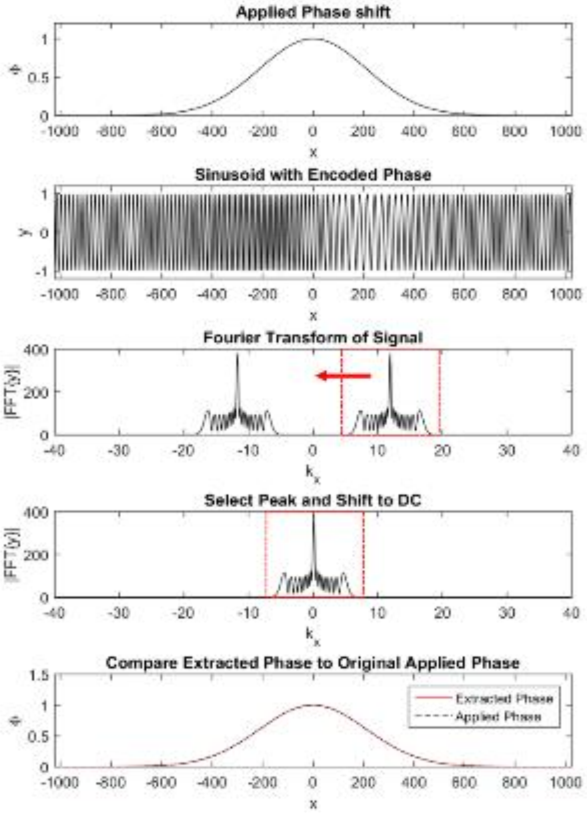

Figure A.1 A benchmark of the phase extraction algorithm. A phase shift Φ(x) is applied to a sinusoid to make a signal y(x). The phase is extracted by selecting a peak in the Fourier domain k_x, and shifting it to zero before inverting. The phase of the resulting complex envelope is the extracted phase from the waveform which is in good agreement with the original applied phase.

A.1.1 Phase Extraction

Phase extraction from interferograms is achieved by identifying a peak in the two-dimensional FFT of the interferograms, and shifting it to center on zero frequency. Taking the argument of the inverse FFT of the resulting image produces a phase shift image which can be further processed to attain neutral gas or plasma density. This technique can also be used to map the envelope of a laser pulse from a simulation.

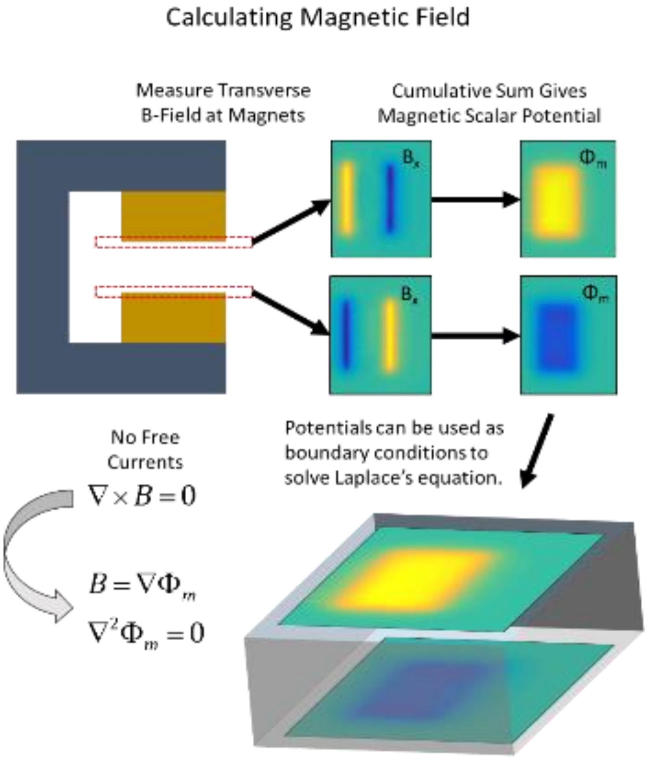

Figure A.2 A volumetric magnetic field is calculated using the magnetic field along its surface to define the boundaries of a magnetic scalar potential. This scalar potential, which obeys Laplace's equation, is solved numerically

A.1.2 Spectrometer Magnetic Field Calculation

The calibration of the electron spectrometer described in Chapter 2 relied on the calculation of a 3D magnetic field from a measured magnetic field. This was achieved by using the absence of free currents to define a magnetic scalar potential which obeys Laplace's equation.

Using measurements of the transverse magnetic field at the magnet surfaces, the magnetic scalar potential Φ_m was found by integrating them at their respective planes. These were then be used as boundary conditions for a field solver. The scalar potential was solved by the method of relaxation [42] converging to a tolerance of one part in one thousand.

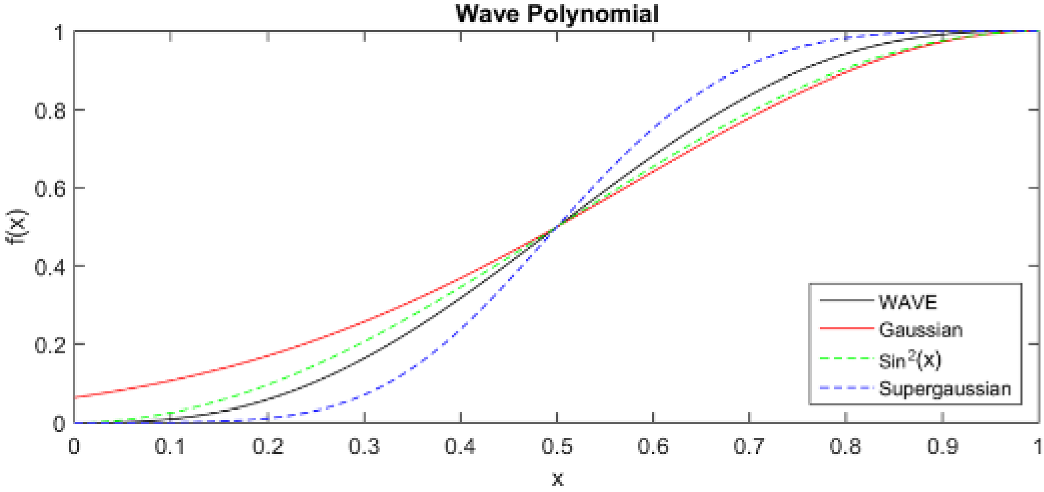

Figure A.3 A comparison of a quintic polynomial used in TurboWAVE to various functions which it may approximate. Parameters are chosen to match peak value and FWHM.

A.1.2 WAVE 5th Order Polynomial

In TurboWAVE, it is necessary to initiate electromagnetic waves in vacuum. To do this, the longitudinal profiles of the laser pulse and plasma must have well-defined termination points. In this work, a fifth-order polynomial, referred to as WAVE, was frequently used to approximate a Gaussian. This polynomial is plotted in figure A.3 and is given by,

$$WAVE(x) = 10x^3 - 15x^4 - 6x^5 \tag{A.1}$$

It can be seen in figure A.3 that WAVE is a good approximation to $\sin^2(x)$ but can have almost 10% deviation from a Gaussian.

This polynomial was used to generate the longitudinal envelope of all laser pulses as well as all longitudinal plasma density profiles. Whenever this polynomial was used to represent a Gaussian, parameters were chosen such that the polynomial shared a FWHM with the desired Gaussian.

Appendix II: Derivations

A.2.1 Relativistic Factor as a Function of Vector Potential

The energy of a charged particle in a relativistically strong electromagnetic plane wave is derived. The Lagrangian for a charged particle in an electromagnetic field is,

$$L = -mc^2\sqrt{1-\frac{v^2}{c^2}} + \frac{e}{c}\mathbf{v}\cdot\mathbf{A} - e\Phi \tag{A.2}$$

which can be normalized,

$$\begin{aligned} l &= -\sqrt{1-\beta^2} - \boldsymbol{\beta}\cdot\mathbf{a} + \phi \\ l &= \frac{L}{mc^2} \\ \boldsymbol{\beta} &= \frac{\mathbf{v}}{c} \\ \mathbf{a} &= \frac{e\mathbf{A}}{mc^2} \\ \phi &= \frac{e\Phi}{mc^2} \end{aligned} \tag{A.3}$$

Assuming **a** takes the form of a plane wave polarized in the x-direction, traveling in the z-direction and no scalar potential,

$$\begin{aligned} \mathbf{a} &= a_x(z,t)\hat{x} \\ \phi &= 0 \end{aligned} \tag{A.4}$$

The Lagrangian has no explicit x-dependence, so the corresponding canonical momentum is conserved,

$$\begin{aligned} &\frac{dP_x}{dt}=0 \\ &\frac{P_x}{mc}=\frac{\partial l}{\partial \beta_x}=\frac{\beta_x}{\sqrt{1-\beta^2}}-a_x \end{aligned} \tag{A.5}$$

It can be taken that before the wave encounters the particle, the particle is at rest. This implies that the canonical momentum at that time is zero,

$$\begin{aligned} &\beta_x(t=0)=0 \\ &a_x(t=0)=0 \\ &=> P_x(t=0)=0 \end{aligned} \tag{A.6}$$

Thus, the velocity is related to the vector potential by,

$$a_x=\frac{\beta_x}{\sqrt{1-\beta^2}}=\gamma\beta_x \tag{A.7}$$

Assuming the x-component of β dominates the particle motion, this can be solved for gamma in terms of a_x to give,

$$\gamma=\sqrt{1+a_x^2} \tag{A.8}$$

A.2.2 Time Averaging for the Ponderomotive Energy

The derivation of the ponderomotive force in Chapter 1 hinges on the identification of a "ponderomotive energy." This energy is the average kinetic energy of a quivering electron in an electromagnetic field, and can be derived by considering the results from Appendix A.2.1 and identifying time dependence,

$$\gamma(t)=\sqrt{1+a_x^2(t)} \tag{A.9}$$

The time-averaged relativistic factor can be defined,

$$<\gamma>\equiv\frac{1}{\tau}\int_0^{\tau}dt\sqrt{1+a_x^2(t)} \tag{A.10}$$

where τ is the time over which the factor is being averaged. This can be taken to be one period of the oscillation of a_x which can be taken to be a sinusoid,

$$a_x(t)=a_0\cos(\omega t) \tag{A.11}$$

The average relativistic factor is therefore,

$$<\gamma>=\frac{\omega}{2\pi}\int_0^{2\pi/\omega}dt\sqrt{1+a_0^2\cos^2(\omega t)} \tag{A.12}$$

With some algebra, this takes the form,

$$\begin{aligned}<\gamma>&=\frac{2}{\pi}\sqrt{1+a_0^2}\int_0^{\pi/2}d\omega t\sqrt{1-\frac{a_0^2}{1+a_0^2}\sin^2(\omega t)}\\<\gamma>&=\frac{2}{\pi}\sqrt{1+a_0^2}\cdot E\left(\sqrt{\frac{a_0^2}{1+a_0^2}}\right)\end{aligned} \tag{A.13}$$

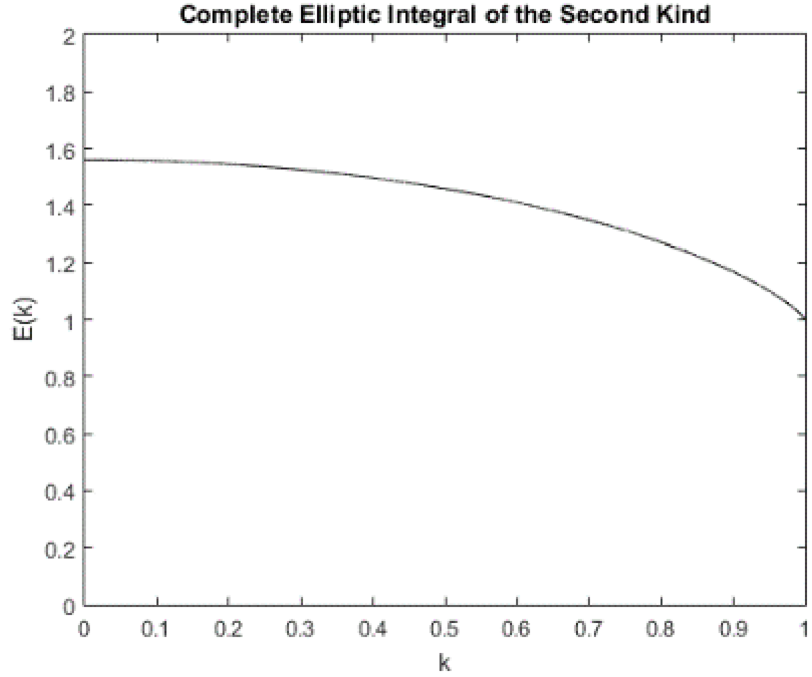

Figure A.4 The complete elliptic integral of the second kind.

Where the complete elliptic integral of the second kind is identified,

$$E\left(k\right)=\int_0^{\pi/2} d\theta\sqrt{1-k^2\sin^2(\theta)} \tag{A.14}$$

It can also be seen that for small a_0, the relativistic factor approaches,

$$<\gamma>\approx\sqrt{1+a_0^2}\approx 1+\tfrac{1}{2}a_0^2 \tag{A.15}$$

Which was used in Chapter 1 to derive the relativistic plasma frequency and the ponderomotive force. For large values of a_0, the relativist factor approaches

$$<\gamma>=\frac{2}{\pi}a_0 \tag{A.16}$$

A.2.3 A Toy Model for STOV Formation

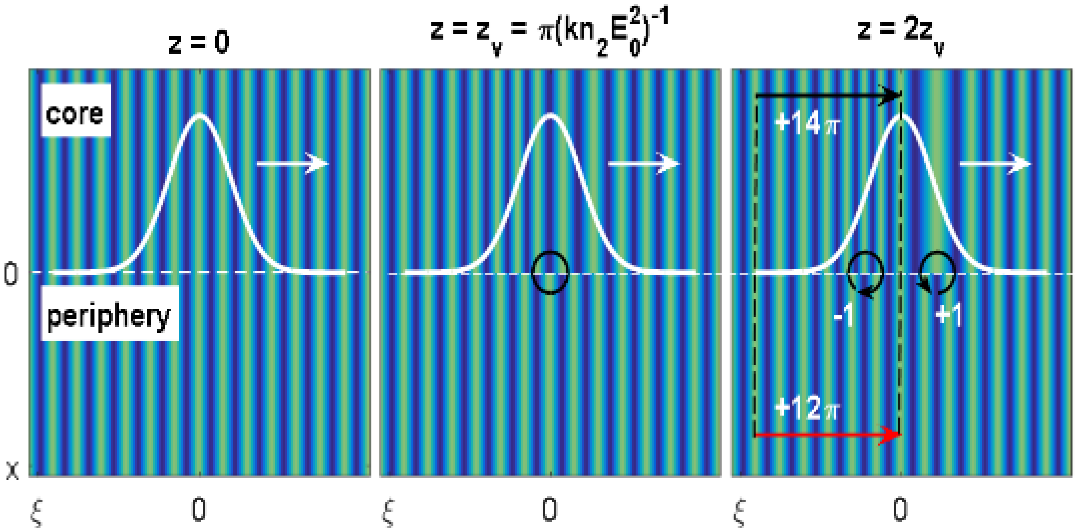

Figure A.8 A toy model for STOV formation. (left) An electromagnetic wave with a temporal intensity profile (superimposed in white). The medium in which it travels is divided into a 'core' with nonlinearities, and a 'periphery' without. (center) This causes a phase slippage between the core and periphery, eventually reaching a difference of π after propagating a distance z_v, forming a phase defect and intensity null indicated by the black circle. (right) As the phase continues to slip, the defect decomposes into a pair of defects about which opposite topological charge can be identified. Counting oscillations above and below a defect and taking the difference gives the topological charge of the defect.

(Adapted from Jhajj *et al.* [64])

Appendix III: Experimental Considerations

A.3.1 The Self-Filtering Unstable Resonator

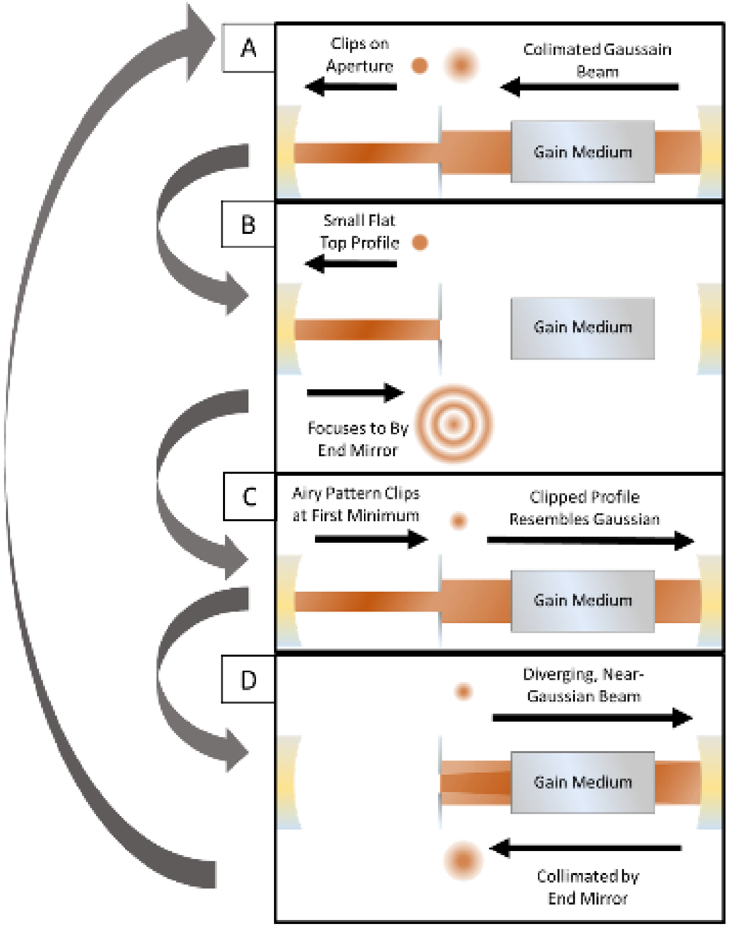

Figure A.9 The mechanism behind the self-filtering unstable resonator cavity. (A)On each pass, a collimated beam is clipped by an aperture. (B) The resulting small flat-top profile is focused by an end mirror back onto the aperture such that (C) the resulting Airy profile is clipped at the first minimum, producing a small near-Gaussian profile which diverges from the aperture. (D) The diverging beam is amplified by the gain medium, and collimated by another end mirror. The reflected collimated beam is amplified through the rod again, after which it heads towards the aperture repeating the cycle.

Figure A.10 The aperture in the Nd:YAG regenerative amplifier SFUR(left), and a damaged pinhole used in the Nd:YAG vacuum spatial filter.(right) The SFUR aperture is still a clean, 1mm circle after decades of use. The laser profile is burned around the aperture, showing the extent to which the aperture is overfilled. In contrast, the VSF pinhole is easily damaged by misaligning the high power beam which is focused through it.

The Nd:YAG laser regenerative amplifier has a self-filtering unstable resonator(SFUR) design, described in detail in [38]. The goal of including this section in the appendix is to dispel misconceptions about the self-filtering unstable resonator. Neither end mirror truly focuses the beam onto the aperture. The end mirror on the right collimates the beam, while the end mirror on the left, although placed with the aperture at its focus, serves only to transform the small flat-top beam into its far-field Airy pattern.

The aperture is fashioned from a sturdy metal with a 1mm hole, making it robust to standard operation. This is in contrast to the pinhole in the vacuum spatial filter (VSF) which is easily damaged. Because the SFUR produces a clean Gaussian profile, the load on the vacuum spatial filter is reduced. However, even with standard operation, the VSF pinhole needs to be changed out regularly.

A.3.2 Energy Curves for Permanent Magnet Spectrometer

Using the 3D magnetic field which resulted from section A.1.2, an electron spectrometer was simulated in CyberRay ray tracing software. The magnetic field was originally measured using the 1/8" thick magnets. To simulate other magnets, this field was scaled linearly with the magnet thickness, in good agreement with the magnet specifications.

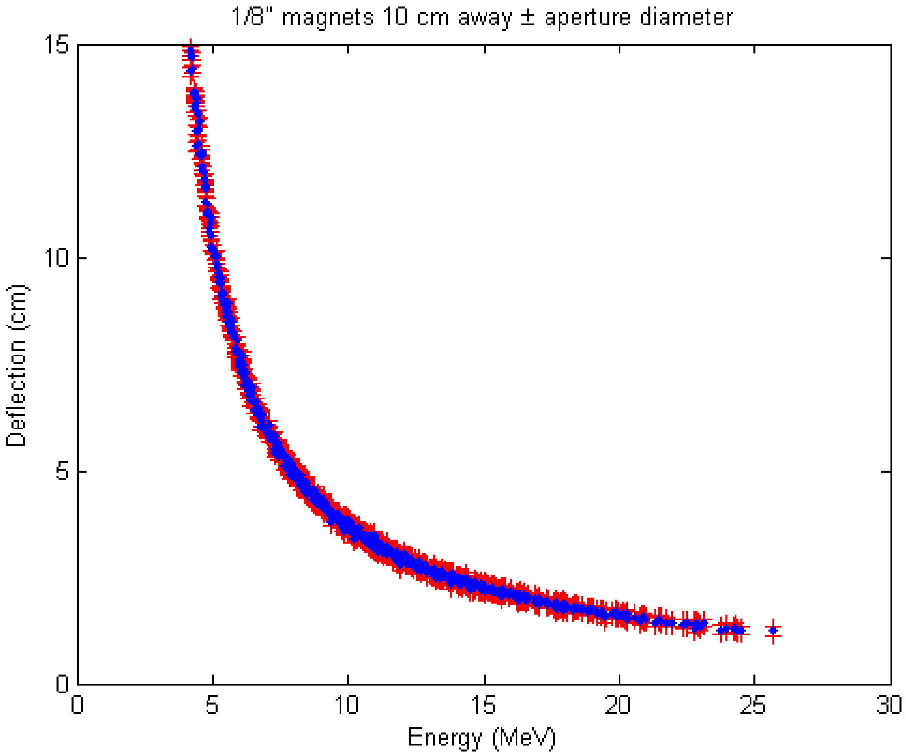

Figure A.11 Electron deflection as a function of energy for the simulated spectrometer using 1/8" magnets.

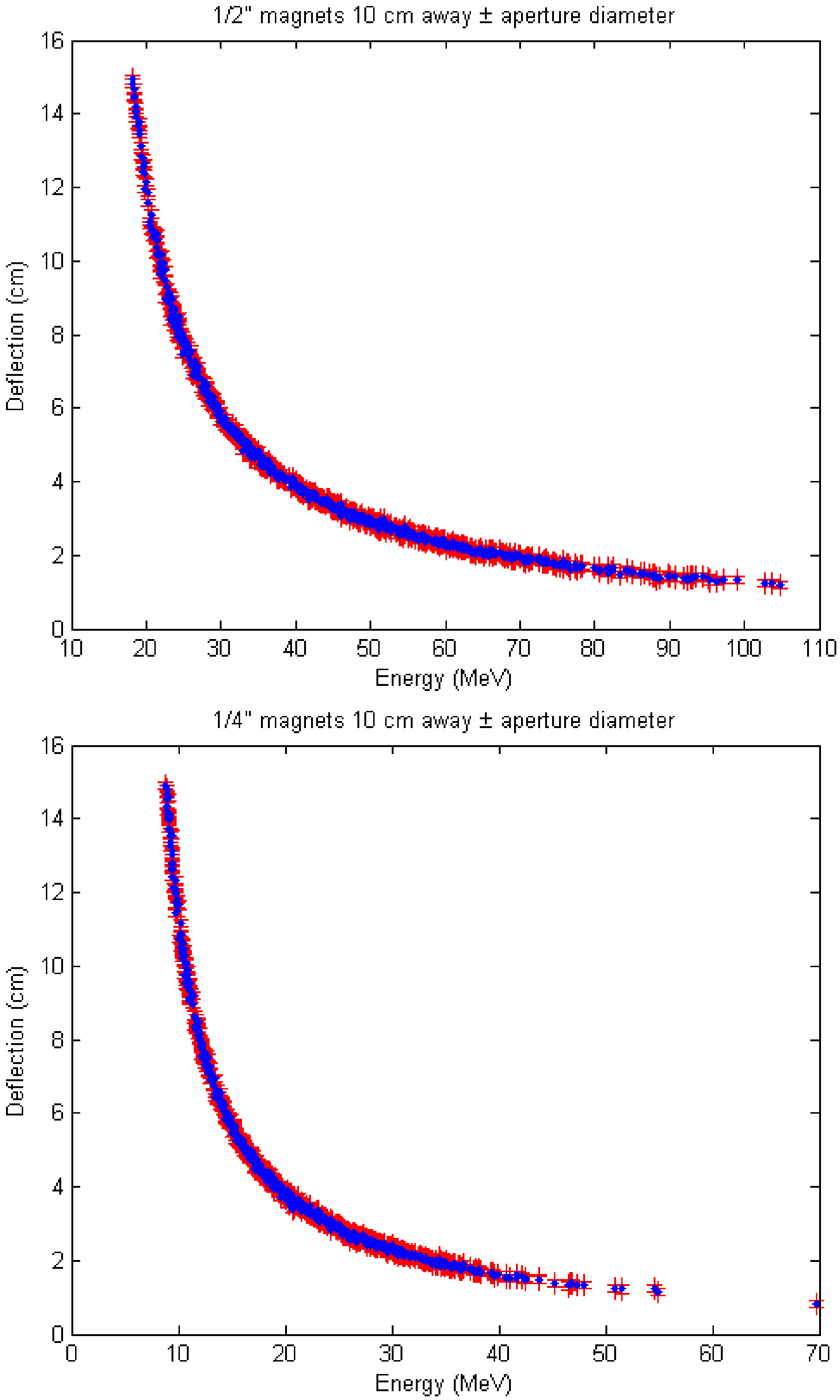

Figure A.12 Electron deflection as a function of energy for the simulated spectrometer using 1/2" and 1/4" magnets.

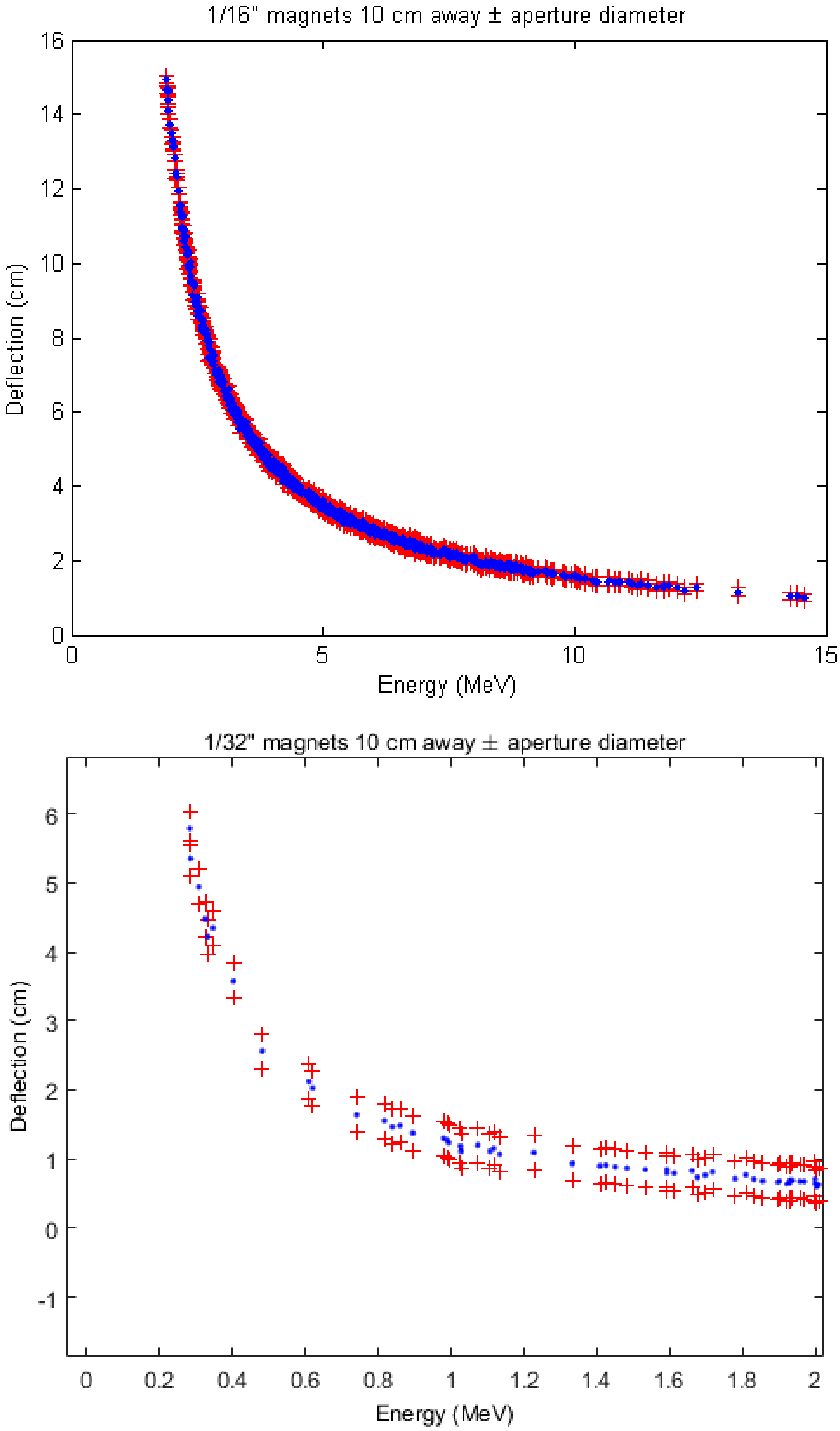

1/16" magnets 10 cm away ± aperture diameter

1/32" magnets 10 cm away ± aperture diameter

Figure A.13 Electron deflection as a function of energy for the simulated spectrometer using 1/16” and 1/32” magnets.

Bibliography

[1] R. W. Hamm and M. E. Hamm, *Industrial Accelerators and Their Applications* (2012).

[2] W. R. Hendee, Rev. Mod. Phys. **71**, 444 (1999).

[3] M. Demarteau, R. Lipton, H. Nicholson, and I. Shipsey, Rev. Mod. Phys. **88**, 45007 (2016).

[4] G. A. Loew, in *Handb. Accel. Phys. Eng.*, edited by A. W. Chao and M. Tigner, 1st ed. (1998), pp. 27–28.

[5] R. Bingham, J. T. Mendonça, and P. K. Shukla, Plasma Phys. Control. Fusion **46**, R1 (2004).

[6] H. Daido, M. Nishiuchi, and A. S. Pirozhkov, Rep. Prog. Phys. **75**, 56401 (2012).

[7] W. P. Leemans, A. J. Gonsalves, H. S. Mao, K. Nakamura, C. Benedetti, C. B. Schroeder, C. Toth, J. Daniels, D. E. Mittelberger, S. S. Bulanov, J. L. Vay, C. G. R. Geddes, and E. Esarey, Phys. Rev. Lett. **113**, 1 (2014).

[8] A. J. Goers, G. A. Hine, L. Feder, B. Miao, F. Salehi, J. K. Wahlstrand, and H. M. Milchberg, Phys. Rev. Lett. **115**, (2015).

[9] M. N. Zervas and C. a. Codemard, IEEE J. Sel. Top. Quantum Electron. **20**, 1 (2014).

[10] H. Fattahi, H. G. Barros, M. Gorjan, T. Nubbemeyer, B. Alsaif, C. Y. Teisset, M. Schultze, S. Prinz, M. Haefner, M. Ueffing, A. Alismail, L. Vámos, A. Schwarz, O. Pronin, J. Brons, X. T. Geng, G. Arisholm, M. Ciappina, V. S. Yakovlev, D.-E. Kim, A. M. Azzeer, N. Karpowicz, D. Sutter, Z. Major, T.

Metzger, and F. Krausz, Optica **1**, 45 (2014).

[11] C. Durfee III and H. Milchberg, Phys. Rev. Lett. **71**, 2409 (1993).

[12] B. Layer, A. York, T. Antonsen, S. Varma, Y.-H. Chen, Y. Leng, and H. Milchberg, Phys. Rev. Lett. **99**, 35001 (2007).

[13] T. Clark and H. Milchberg, Phys. Rev. E. Stat. Phys. Plasmas. Fluids. Relat. Interdiscip. Topics **61**, 1954 (2000).

[14] G. Fibich, *The Nonlinear Schrödinger Equation: Singular Solutions and Optical Collapse* (2015).

[15] C. G. Durfee and H. M. Milchberg, Phys. Rev. Lett. **71**, 2409 (1993).

[16] A. J. Goers, S. J. Yoon, J. A. Elle, G. A. Hine, and H. M. Milchberg, Appl. Phys. Lett. **104**, 214105 (2014).

[17] P. Sprangle, E. Esarey, and A. Ting, Phys. Rev. Lett. **64**, 2011 (1990).

[18] P. Sprangle, C. M. Tang, and E. Esarey, IEEE Trans. Plasma Sci. **15**, 145 (1987).

[19] T. Tajima and J. Dawson, Phys. Rev. Lett. **43**, 267 (1979).

[20] A. Pukhov, S. Gordienko, S. Kiselev, and I. Kostyukov, Plasma Phys. Control. Fusion **46**, B179 (2004).

[21] S. Bulanov, N. Naumova, F. Pegoraro, and J. Sakai, Phys. Rev. E **58**, R5257 (1998).

[22] C. G. R. Geddes, C. Toth, J. van Tilborg, E. Esarey, C. B. Schroeder, D. Bruhwiler, C. Nieter, J. Cary, and W. P. Leemans, Nature **431**, 538 (2004).

[23] S. P. D. Mangles, C. D. Murphy, Z. Najmudin, A. G. R. Thomas, J. L. Collier, A. E. Dangor, E. J. Divall, P. S. Foster, J. G. Gallacher, C. J. Hooker, D. A.

Jaroszynski, A. J. Langley, W. B. Mori, P. A. Norreys, F. S. Tsung, R. Viskup, B. R. Walton, and K. Krushelnick, Nature **431**, 535 (2004).

[24] J. Faure, Y. Glinec, A. Pukhov, S. Kiselev, S. Gordienko, E. Lefebvre, J.-P. Rousseau, F. Burgy, and V. Malka, Nature **431**, 541 (2004).

[25] S. J. Yoon, J. P. Palastro, and H. M. Milchberg, Phys. Rev. Lett. **112**, 134803 (2014).

[26] B. D. Layer, A. York, T. M. Antonsen, S. Varma, Y. H. Chen, Y. Leng, and H. M. Milchberg, Phys. Rev. Lett. **99**, 35001 (2007).

[27] A. York, H. Milchberg, J. Palastro, and T. Antonsen, Phys. Rev. Lett. **100**, 195001 (2008).

[28] S. Yoon, J. Palastro, D. Gordon, T. Antonsen, and H. Milchberg, Phys. Rev. Spec. Top. - Accel. Beams **15**, 81305 (2012).

[29] A. J. Goers, Electron Acceleration by Femtosecond Laser Interaction with Micro-Structured Plasmas, University of Maryland, 2015.

[30] A. Macchi, M. Borghesi, and M. Passoni, arXiv Prepr. arXiv1302.1775 (2013).

[31] M. Passoni, L. Bertagna, and A. Zani, New J. Phys. **12**, (2010).

[32] L. O. Silva, M. Marti, J. R. Davies, R. a Fonseca, C. Ren, F. S. Tsung, and W. B. Mori, Phys. Rev. Lett. **92**, 15002 (2004).

[33] A. Henig, S. Steinke, M. Schnurer, T. Sokollik, R. Horlein, D. Kiefer, D. Jung, J. Schreiber, B. M. Hegelich, X. Q. Yan, J. Meyer-Ter-Vehn, T. Tajima, P. V. Nickles, W. Sandner, and D. Habs, Phys. Rev. Lett. **103**, 3 (2009).

[34] L. Yin, B. J. Albright, B. M. Hegelich, K. J. Bowers, K. A. Flippo, T. J. T. Kwan, and J. C. Fernández, Phys. Plasmas **14**, (2007).

[35] F. Salehi, A. J. Goers, G. A. Hine, L. Feder, D. Kuk, B. Miao, D. Woodbury, K. Kim, and H. Milchberg, Opt. Lett. **42**, 2 (2016).

[36] J. Isaacs and P. Sprangle, Appl. Phys. Lett. **110**, 24101 (2017).

[37] S. V. Bulanov, Plasma Phys. Reports **31**, 369 (2005).

[38] C. G. Durfee III and H. M. Milchberg, Opt. Lett. **17**, 37 (1992).

[39] Www.fastlite.com (2015).

[40] O. F. Hagena, Surf. Sci. **106**, 101 (1981).

[41] S. J. Yoon, A. J. Goers, G. A. Hine, J. D. Magill, J. A. Elle, Y.-H. Chen, and H. M. Milchberg, Opt. Express **21**, 15878 (2013).

[42] W. H. (Harvard-S. C. for A. Press, C. U. Saul A. Teaukolsky (Department of Physics, W. T. V. (Polaroid Corporation), and B. P. F. (EXXON R. and E. Company), *Numerical Recipes in C: The Art of Scientific Computing* (1988).

[43] B. Hafizi, D. F. Gordon, A. Zigler, and A. Ting, Phys. Plasmas **10**, 2545 (2003).

[44] A. Buck, K. Zeil, A. Popp, K. Schmid, A. Jochmann, S. D. Kraft, B. Hidding, T. Kudyakov, C. M. S. Sears, L. Veisz, S. Karsch, J. Pawelke, R. Sauerbrey, T. Cowan, F. Krausz, and U. Schramm, Rev. Sci. Instrum. **81**, (2010).

[45] Y. Glinec, J. Faure, A. Guemnie-Tafo, V. Malka, H. Monard, J. P. Larbre, V. De Waele, J. L. Marignier, and M. Mostafavi, Rev. Sci. Instrum. **77**, 1 (2006).

[46] C. K. Birdsall and A. B. Langdon, *Plasma Physics via Computer Simulation* (2004).

[47] J. M. Dawson, Rev. Mod. Phys. **55**, 403 (1983).

[48] B. B. Godfrey, J. L. Vay, and I. Haber, J. Comput. Phys. **258**, 689 (2014).

[49] R. Lehe, M. Kirchen, I. A. Andriyash, B. B. Godfrey, and J. L. Vay, Comput. Phys. Commun. **203**, 66 (2015).

[50] I. A. Andriyash, R. Lehe, and A. Lifschitz, **33110**, (2015).

[51] A. Gonoskov, S. Bastrakov, E. Efimenko, A. Ilderton, M. Marklund, I. Meyerov, A. Muraviev, A. Sergeev, I. Surmin, and E. Wallin, Phys. Rev. E - Stat. Nonlinear, Soft Matter Phys. **92**, 1 (2015).

[52] D. F. Gordon, B. Hafizi, and M. H. Helle, J. Comput. Phys. **267**, 50 (2014).

[53] D. F. Gordon, IEEE Trans. Plasma Sci. **35**, 1486 (2007).

[54] J. Verboncoeur, Plasma Phys. Control. Fusion **47**, (2005).

[55] D. Spence and S. Hooker, Phys. Rev. E **63**, 15401 (2000).

[56] V. Kumarappan, K. Y. Kim, and H. M. Milchberg, Phys. Rev. Lett. **94**, 18 (2005).

[57] H. Sheng, K. Kim, V. Kumarappan, B. Layer, and H. Milchberg, Phys. Rev. E **72**, 36411 (2005).

[58] M. Takeda, H. Ina, and S. Kobayashi, J. Opt. Soc. Am. **72**, 156 (1982).

[59] M.-W. Lin, Y.-M. Chen, C.-H. Pai, C.-C. Kuo, K.-H. Lee, J. Wang, S.-Y. Chen, and J.-Y. Lin, Phys. Plasmas **13**, 110701 (2006).

[60] M. Takeda, H. Ina, and S. Kobayashi, J. Opt. Soc. Am. **72**, 156 (1982).

[61] J. Sochacki, A. Kołodziejczyk, Z. Jaroszewicz, and S. Bará, Appl. Opt. **31**, 5326 (1992).

[62] H. M. Milchberg, T. R. Clark, C. G. Durfee, T. M. Antonsen, and P. Mora, Phys. Plasmas **3**, 2149 (1996).

[63] G.-Z. Sun, E. Ott, Y. C. Lee, and P. Guzdar, Phys. Fluids **30**, 526 (1987).

[64] N. Jhajj, I. Larkin, E. W. Rosenthal, S. Zahedpour, J. K. Wahlstrand, and H. M. Milchberg, Phys. Rev. X **6**, 1 (2016).

[65] M. S. Paoletti, M. E. Fisher, and D. P. Lathrop, Phys. D Nonlinear Phenom. **239**, 1367 (2010).

[66] J. Koplik and H. Levine, Phys. Rev. Lett. **71**, 1375 (1993).

[67] A. G. R. Thomas, S. P. D. Mangles, Z. Najmudin, M. C. Kaluza, C. D. Murphy, and K. Krushelnick, Phys. Rev. Lett. **98**, 2 (2007).

[68] S. V. Bulanov, T. Z. Esirkepov, M. Kando, J. K. Koga, A. S. Pirozhkov, T. Nakamura, S. S. Bulanov, C. B. Schroeder, E. Esarey, F. Califano, and F. Pegoraro, Phys. Plasmas **19**, (2012).

[69] B. M. Penetrante and J. N. Bardsley, Phys. Rev. A **43**, 3100 (1991).

[70] T. Nakamura, S. V. Bulanov, T. Z. Esirkepov, and M. Kando, Phys. Rev. Lett. **105**, 135002 (2010).

[71] Http://www.oecd-Nea.org/janisweb/index.html (2016).

[72] M. H. Helle, D. F. Gordon, D. Kaganovich, Y. Chen, J. P. Palastro, and A. Ting, Phys. Rev. Lett. **117**, 1 (2016).

[73] Y. Fukuda, A. Y. Faenov, M. Tampo, T. A. Pikuz, T. Nakamura, M. Kando, Y. Hayashi, A. Yogo, H. Sakaki, T. Kameshima, A. S. Pirozhkov, K. Ogura, M. Mori, T. Z. Esirkepov, J. Koga, A. S. Boldarev, V. A. Gasilov, A. I. Magunov, T. Yamauchi, R. Kodama, P. R. Bolton, Y. Kato, T. Tajima, H. Daido, and S. V. Bulanov, Phys. Rev. Lett. **103**, 1 (2009).

[74] A. Sharma and A. Andreev, Laser Part. Beams 1 (2016).

[75] Y. K. Kim, T. Kang, M. Y. Jung, and M. S. Hur, Phys. Rev. E - Stat.

Nonlinear, Soft Matter Phys. **94**, 1 (2016).

[76] A. V. Kuznetsov, T. Z. Esirkepov, F. F. Kamenets, and S. V. Bulanov, Plasma Phys. Reports **27**, 211 (2001).

[77] Http://www.us.trumpf.com/en/products/laser-Technology.html (2016).

[78] J. Tümmler, R. Jung, T. Nubbemeyer, I. Will, and W. Sandner, 2 (2011).

[79] R. Jung, J. Tümmler, T. Nubbemeyer, and I. Will, Opt. Express **24**, 4375 (2016).

[80] U. Buenting, H. Sayinc, D. Wandt, U. Morgner, and D. Kracht, Opt. Express **17**, 8046 (2009).

[81] G. A. Mourou, Z. Chang, a. Maksimchuk, J. Nees, S. V. Bulanov, V. Y. Bychenkov, T. Z. Esirkepov, N. M. Naumova, F. Pegoraro, and H. Ruhl, Plasma Phys. Reports **28**, 12 (2002).

[82] D. J. Kane and R. Trebino, IEEE J. Quantum Electron. **29**, 571 (1993).